Two-Component Bose-Einstein Condensation

by

Michael Robin Matthews

B.S., University of Texas, 1994

A thesis submitted to the
Faculty of the Graduate School of the
University of Colorado in partial fulfillment
of the requirements for the degree of
Doctor of Philosophy
Department of Physics
1999

This thesis entitled:
Two-Component Bose-Einstein Condensation
written by Michael Robin Matthews
has been approved for the Department of Physics

Prof. Eric Cornell

Prof. Deborah Jin

Date

The final copy of this thesis has been examined by the signatories, and we find that both the content and the form meet acceptable presentation standards of scholarly work in the above mentioned discipline.

Matthews, Michael Robin (Ph.D., Physics)

Two-Component Bose-Einstein Condensation

Thesis directed by Prof. Eric Cornell

Bose-Einstein condensates in dilute atomic gases have been around for almost 5 years now. The first experiments dealt with density related properties of the condensate – things like internal energy, collective excitations, and density profiles. All of these aspects are well described by a non-linear Schrodinger equation, in which the non-linearity arises from repulsive potentials between ^{87}Rb atoms that make up the condensate. While interesting in their own right, these experiments had little to do with the “strangeness” of a condensate as a macroscopic quantum object.

In this work the new era of condensate physics is described. These are experiments mainly concerned with the quantum phase and coherence properties. We have constructed a robust system for creating internal-state superpositions, with the ability to image the interference between them. Our first observations show how condensates, initially created with a well-defined phase, remain coherent, unlike a sample of thermal atoms. We have devised schemes to spatially manipulate the relative phase between two condensates in unique ways which brings about very unexpected behavior. By choosing a very specific scheme we were able to create a vortex state and measure the unique 2π phase winding, making this a very simple system for utilizing quantum control.

Dedication

I dedicate this work to my wife Melanie, and my parents Ann and Robin. Melanie has really given up a lot so that I could follow physics. To her it meant living apart for many years, and always having to cut short our time together. She has been incredibly patient and supportive, and understanding when sometimes physics came first. I hope I can make it up to her.

Sometimes people ask my parents where I got my talent at physics. For some reason people assume that it could not have been from a kindergarten teacher and a highschool geography teacher. Well, it was. From as early as I can remember, they motivated in me an interest in everything. They indulged me when ever they could afford to – things from archery to cadaver frogs. One of the first times I remember thinking about the world was when I asked my dad why the Battlestar Gallactica ships seemed to have so many parts that weren't aerodynamic. He answered "That's smart thinking, but remember, there is no air is space". To this I replied, "Then why do all the movies have ships that look so much like airplanes?". Eventually my scientific knowledge outgrew theirs, but their love and support continued. Both my sister and I owe them everything for our talent and confidence to pursue the most difficult paths.

Acknowledgements

Given the stereotype of physicists as introverted and antisocial, it seems amazing that I have not had to work with a single one. The Wieman, Cornell and Jin groups have known some truly dedicated, bright, and fun people.

First, I need to acknowledge Eric Cornell for the opportunity and guidance. He knew when to lend advice, and when to let me go off on my own. His grasp of physics inspired me to understand things from new perspectives. It's been a privilege to work with him. Carl Wieman is another great physicist who led me through my graduate career. His technical intuition always motivated me to seek out new methods and find simple but useful techniques. Even though their status is among the elite, and the Nobel Prize may well come to JILA, they always treated the grad students as respectable, intelligent scientists in their own right. It's part of what made JILA a stimulating environment.

There have been other great scientists who shared equally in this work. Mike Anderson who pushed me into the experiment head first, and was responsible for most of the work leading to the original BEC. Jason Ensher was a co-grad student for most of my time here. He and I worked very well together with complimentary styles. The second post-doc I had the privilege of working with was Deborah Jin. Coming from a condensed matter background, she had little atomic physics training, and yet always seems to stay a step ahead of everything. She, Jason and I made a great team, and did some of the best early condensate studies in the world. After feeling a personal responsibility for the success of our experiment, David Hall came to our group as a post-doc. He was very well trained in the art of precision measurement, which led to numerous arguments between us concerning nearly every detail of the apparatus. Because of this, the experiment was taken to another level. We ferreted out some of the last bugs and made the experiment extremely robust, making the best compromises between making things work and making things right. It was a great experience working with David (except when *he* suggested to Carl that we find some cots for the lab so we could sleep there too). Paul Haljan recently entered the group, and has contributed a lot to this work. He and the newest post-doc Brian Anderson have been instrumental in the recent vortex studies. The experiment is in good hands.

On another front, much of this work was based on and/or motivated by the work of theorists at JILA. Jinx Cooper, Chris Greene, Murray Holland, and John "Weird" Bohn have given a lot of support and ideas. Jim Burke, Brett Esry, and Jamie Williams have devoted much of their efforts to understanding and providing new directions for our experiment.

I would like to acknowledge the older post-docs and grad-students who not only made JILA a great place to work, but taught me a lot of physics: post-docs Eric Abraham, Eric Burt, Marla Dowell, Tim Dinneen, Zheng-Tian Lu, Nate Newbury, and Mike Renn, and grad students Steve Bennett, Kristan Corwin, Elizabeth Donley, Chris Myatt, Brad Paul, Jake Roberts, Kurt Vogel, and Chris Wood. No one could ask for a better group of people to work with over the years.

The Wieman/Cornell and now Jin groups are blessed with a new generation of post-docs and grad student. Post-docs Simon Cornish and Simon Kuppens, along with graduate students Neil Claussen, Brian DeMarco, Heather Lewandowski, Kurt Miller, and Dirk Mueller have been very helpful.

This work relied heavily on the expertise of the instrument and electonics shop people: David Alchenberger, Hans Green, Seth Wieman, and Hans Rohner, from the instruments shop and Paul Beckingham, Terry Brown, James Fung-A-Fat, and Michael Whitmore from the electronics shop .

Fran Haas, Pam Leland, and Karen Melcher helped make JILA a fun place to be, not to mention the daunting task of keeping Eric and Carl organized and on time, which made my work that much easier.

Contents

Chapter

Appendix

Figures

Figure

Tables

Table

Chapter 1

Introduction

1.1 Overview

Bose-Condensation is formed when a macroscopic population of bosons occupy the same quantum state at non-zero temperature. Our experiment can be thought of as a series of steps that make all degrees of freedom for a large number Rubidium atoms exactly the same. Luckily, most of the steps are simply selecting out atoms which are already in the same state. The methods we go through follow a progression from higher to lower energy scales, becoming more difficult as the energy lowers. This of course begins by selecting Rb to put in our vacuum chamber (this part is simple, because our living at room temperature means we find Rb is already non-degenerate with other elements – only chemically combined). Next we select out the isotope of ^{87}Rb from ^{85}Rb by tuning our magneto-optical trapping (MOT) lasers to the proper wavelength so that only ^{87}Rb is captured in our trap. The only remaining degrees of freedom are the internal energy levels of ^{87}Rb (the hyperfine and Zeeman levels) and the external, motional degree of freedom (the harmonic oscillator energy level). With optical pumping techniques we can force most of the atoms into the same internal level. Those that we don't get are effectively removed from the sample by our magnetic trap's selectivity – only specific internal levels are confined. The last step is the most difficult. At this point in the experiment the atoms are confined in a harmonic, magnetic trap, but their energy is much larger than the spacing of the oscillator levels, so the probability of even a single atom existing in a given state is small. Forced evaporation [61] is used to cool the sample until nearly all atoms exist in the same ground state; the zero-point energy of our trap.

In principle BEC can occur in states other than the ground state, but the large state space available to particles makes arbitrary-state BEC creation unlikely. The ground state posses this one advantage; it is the end of the road for a system being cooled. Atoms cooled in a harmonic trap must eventually run into the ground state, piling up as they run out of energy levels to occupy. Of course, BEC is much more than a simple state-space argument. The symmetry of bosons brings about a stimulated process whereby atoms have a preference to scatter into a state already occupied. There are, however, so many states available for an atom to occupy when at higher temperatures, that the enhancement is generally immaterial. The number of accessible states can be limited by colder temperatures (*i.e.* narrowing of the distribution and truncation of the state space by the zero point). Only when the atomic wavefunctions overlap and when there is significant probability to exist in the same state does the Bosonic symmetry become important. This brings about the temperature and density requirements for condensation. The small enhancement factor also grows as the number of atoms in the ground state becomes larger. The wavefunction for N atoms in the ground state is the product wavefunction

$$\psi_{\text{BEC}} = \psi_0(1)\psi_0(2)...\psi_0(N). \tag{1.1}$$

Eq. 1.1 based on a harmonic oscillator potential is not quite a complete description of the multiparticle ground state. Two colliding atoms experience repulsive (in the case of ^{87}Rb) potentials which can be well modeled by a hard sphere interaction. The size of this sphere is given by the s-wave scattering length

a, and leads to a nonlinear term in the wave equation ψ_{BEC} for a condensate, proportional to $aN|\psi_{\mathrm{BEC}}|^2$. For ^{87}Rb the positive scattering length imposes a resistance to compression on the condensate. Condensates with many atoms (like current experiments with $\sim 10^6$) are many times larger in extent, and correspondingly less dense than if $a = 0$. Most of the original BEC experiments over the first two years after 1995 centered on validating the non-linear wave equation, and studying the added richness of the system from the standpoint of the density distribution $|\psi|^2$.

Another interesting trait of BEC is its phase. A phase factor may be written in front of Eq. 1.1, but of course, it takes another condensate in order for the phase to be meaningful. Double condensates were first produced by Myatt *et al.* [108] through poor optical pumping which led to creation of condensates in the two long-lived trappable states of ^{87}Rb (the $|2,2\rangle$ and $|1,-1\rangle$). These two states are not ideal for most double condensate studies since they feel a factor of two difference in trapping potential, and sit in quite distinct positions in the trap due to gravity. ^{87}Rb has another trapped state, the $|2,1\rangle$, which is confined with the same strength as the $|1,-1\rangle$. Thus started our studies on double condensates. It is not trivial to cool these two states simultaneously into condensation since the $|2,1\rangle$ state has a relatively large spin-exchange loss rate. This means it is much easier to create the $|2,1\rangle$ state from an existing $|1,-1\rangle$ condensate, which has the added advantage of starting the system with a well defined relative phase between the two condensates.

This is accomplished through a two photon-transition. The energy splitting between the $|1,-1\rangle$ and $|2,1\rangle$ is second order in magnetic field, centered about the "magic" field value of 3.24 G. We try to operate as close to this field as possible so that the effect of noise from various sources is small. It turns out there is an interesting (and useful) side effect of the TOP trap [114] (our implementation of a harmonic, magnetic trap) on the two-photon transition. The time-dependent rotating field of the TOP trap is equivalent to a fictitious, static magnetic field which acts oppositely on the two states. This translates into linear offsets in the relative position of the states in the trap, and effects the two-photon transition energy. As it turns out, we can use this effect to cancel another offset imposed by the differing magnetic moments (from the higher-order B dependence). This allows for unique control over the separation of the condensates in the TOP trap.

The addition of the new condensate state requires modification of the wavefunction describing each condensate. An extra nonlinear term in each state's wave equation represents the pressure of one condensate on the other. Interestingly, all the scattering lengths involved in the double condensate system are very similar in magnitude. This provides for subtle behavior: each component in a mixture of the two states is able to rearrange its density distribution without much energy cost, as long as it does not affect the overall density distribution.

When the two-photon drive is on, there can be coherent transfer of population between the two states. This can make the dynamics very complicated given the nonlinear interaction between the states. However, when the time scale to make coherent transfer is short compared to the trap oscillation period and the time needed for the interactions kick in, the system can be modeled simply. The atoms can then be treated as discrete, non-interacting two-level systems, and the equations become the two-level Bloch equations applied locally to each part of the condensate. We can then think in terms of familiar concepts to atomic physicists: things like the Bloch sphere, Rabi oscillations, and π-pulses. As the first demonstration of these concepts we placed a condensate in a superposition of the two spin states, and at a later time, read out the relative phase, much like a standard atomic or optical interferometer.

There is of course more to a condensate than just single atom spectroscopy.

In fact, we have an interesting new piece of physics here that is not so accessible in atomic physics. This is a wavefunction which is macroscopic in size, so that we can affect the relative phase and population in a spatially selective manner. It becomes possible to think of multiply connected phase structures such as vortices. Interestingly these experiments can also occur quickly compared to trap oscillations or density-changing behaviour, which means we can apply our two-level model locally to create phase and population structures. Experimentally we can adjust the local detuning and Rabi frequency of the two-photon drive to control the evolution of each discrete point. Of course our ability to implement arbitrary control is finite, and we have only succeeded in creating large scale (order of the condensate) structures.

The first of these was a simple linear phase gradient across the condensate. When the two-photon drive is instantly turned on the condensate oscillates between the two spin states. A continuous spatial variation in the detuning and/or Rabi frequency of the coupling drive means the local phase accumulates at different rates for different positions.

Experimentally what we see corresponds exactly to our local view of discrete two-level systems (at least for short times, before mean-field has much effect). For a vertical gradient in the Rabi frequency, the population oscillations eventually get out of phase between the top and bottom of the condensate. As more time goes by, other parts of the condensate get further out of phase and the condensates appear to be striped, alternating between population of $|1,-1\rangle$ and $|2,1\rangle$ along the vertical axis. Some of these structures actually have quite good overlap with the harmonic oscillator states, which makes this the first quantum-state engineering done with a condensate. For longer times with the two-photon drive on, the phase winds up tighter and tighter.

There turns out to be a subtle condensed matter analogy in this experiment.

If we don't ignore the mean-field and potential terms in the wave equation (or we run the experiment for longer time), then we find a peculiar behavior. The phase which has wound up begins to unwind, even with the two-photon drive still present. In fact it unwinds back to its initial condition of all atoms in the $|1,-1\rangle$ state. An analogy may be drawn to spin-echo [74], except that this recurrence occurs in an inhomogeneous system *without* the application of additional unique pulses to reverse the spin evolution. In this case there is an energy cost associated with the spatial change in phase, and it is the hydrodynamics which drive the atoms to change their superposition of the two spin states. The two-dimensional vector that defines the geometric phase actually has access to a higher dimension – the relative phase between the two states (or equivalently, the relative populations of the dressed states). The fact that it is able to use its extra spin degree of freedom to minimize the energy is a unique feature of our two-component condensate.

One might ask why the phase, instead of unwinding, doesn't just break at some point in order to remove windings. The answer is again the energy cost. Since the condensate is *not* simply the sum of the parts from our local model, there is a large amount of energy required to support a large gradient in phase. If the phase were to become discontinuous at a point, then density must go to zero at that point. This is energetically unfavorable since the pressure from the repulsive interactions opposes that. There is a kind of threshold predicted in this qualitative model. If the winding of the phase is slow enough, then the condensate should have enough energy to continuously remove the phase gradient. We have seen this kind of behavior; for very small gradients in Rabi frequency the condensate never develops stripes, even though it should if a simple scaling applied from the cases with larger gradients. This has only been qualitatively explored.

Given this kind of interpretation of our technique, Williams and Holland [6] proposed another scheme. Their motivation was simple – if a linear phase gradient can be applied in the vertical direction, is it possible to apply the gradient *around* the condensate, in such a way to create a vortex state? The lowest angular momentum state is one with a single quanta of rotation, in which the phase winds by 2π around condensates center. A simple angular dependent phase describes the new wavefunction:

$$\Phi(\vec{r}) = e^{i\phi}\Phi(r). \tag{1.2}$$

One intriguing aspect of superfluid vortices is their metastability. This comes from the same energy argument discussed earlier. Since the phase in a vortex state winds continuously by 2π around the core, it can only unwind by creating a discontinuity – "breaking" the phase. This discontinuity must force the density to zero at that point, creating a large slope in the wavefunction, equivalent to a large kinetic energy. If this energy is not available, the state is metastable.

Numerically solving the nonlinear wave equation, and including an arbitrary mechanism for offsetting the confining potentials for the two spin states (one way to make the phase gradient), Williams and Holland found that such a state could be generated. They proposed applying the two-photon drive to the initial $|1,-1\rangle$ state, while applying a rotating offset. The offset instantaneously produces a gradient in detuning across the cloud, but it is rotated about the cloud's center at a rate comparable to the Rabi frequency. The result is a vortex state in $|2,1\rangle$ with the core region occupied by the $|1,-1\rangle$ state.

This method gets around one of the concepts stated earlier in a unique way. The problem with creating a vortex in an existing, single-state condensate is that the uniform phase of the condensate must be broken, then twisted, then put back together in order to achieve the 2π winding. We found earlier that a condensate resists this breaking (or even tightly twisting) of the phase since it requires a large amount of energy. Using a two-state condensate, we write on the phase *as* the population is transferred into the $|2,1\rangle$ state. Thus we are not bound by the condensates stiffness since there is not yet a condensate in the target state. There is yet another attractive feature of this technique. Since the central region of the condensate is in the $|1,-1\rangle$ state when the vortex is created in the $|2,1\rangle$ state, the states partially overlap. The presence of the $|1,-1\rangle$ enables us to use standard atomic interferometry to read out the relative phase between the two states. What we find is exactly the 2π winding in the phase of the ring shaped $|2,1\rangle$ state.

1.2 Who cares?

These new experiments dealing with and manipulating the condensate's phase, and related work going on in other groups, will be the main focus of BEC physics for many years. So why is this interesting and who cares? ("who" refers to Joe Scientist, not Joe Six-pack). Before BEC was observed in a dilute atomic system, every well-rounded physicist certainly had some interest in the creation of an ideal Bose-Einstein condensate. Not because the theory was thought lacking, but because it was a regime in phase-space which had never been accessible experimentally. Of course physicists in condensed matter and liquid helium have long been able to produce super-conductors and fluids. Unfortunately these are far from an ideal realization of BEC, and required heroic efforts in probing the system on the microscopic level. The thing that draws atomic physicists to the idea of a dilute system is twofold – the ability to have nearly 100% of the particles in the condensate, and the ability to do atomic spectroscopy on them.

The first reason is obvious. Nearly any measurement in atomic physics must take into account broadening from some source, almost always including thermal. With a million or so atoms in the exact same state, the prospects for precision measurements are phenomenal (well, almost... see below), since the broadening is erased, and the signal to noise that much better. Schooled in the atomic clock techniques of magnetic resonance and precision spectroscopy, I find this a strong motivation for creating long lived, unique superpositions and entangled states with the ability to test fundamental physics. Most physicists surely find it extremely appealing to measure quantities with far reaching implications such as parity nonconservation, or the electric dipole moment of the electron, on the top of a small table, in a small room, with only a handful of money and scientists. It is somehow more elegant, or at least, complimentary to high energy experiments.

Unfortunately, some of the experiments in this thesis show precision measurement with condensates still has some hurdles to clear. In the most straightforward form, a precision measurement utilizes the relative phase accumulation between two states which exist in superposition. This phase is easily read using many well developed techniques. It is the amount of relative phase gained by the states while in superposition that is proportional to some energy difference between the states. The real trick then, is to arrange the superposition so that the energy involves the quantity to be measured, and affects the two states differently. Unfortunately, the interactions can produce very unpleasant results. When we create the two-state superposition, the interactions drive some very complex spatial rearrangement of the states. This is unfortunate not only because the state separation makes a relative phase measurement difficult, but also since there is another source of energy which affects the two states differently. There are some possible solutions to this, like optically (or magnetically if the energy of the states can be insensitive to fields) turning off the interactions, or by going to a beam type experiment. The later is one very real application for coherently removing atoms from the condensate (the so-called “atom-laser” [97]). Things like continuous BEC production will be a critical step in this and many other applications.

There is another area I have learned to appreciate and take an interest in, mostly because of Eric's motivation. These are the experiments to make connections with condensed matter physics. Coming into this mostly ignorant of superfluid and superconductor physics, partly because of their theoretical complexity, my real motivation was exploring the quantum nature of BEC, similar to old atomic physics work. And some of our original work with collective modes and other "fluid dynamics" type behavior I found somewhat dry and unenlightening. However there are some great experiments on liquid helium that we have been able to draw strong analogies to, which we can also talk about in atomic physics terms. Plus we have the luxury of superior imaging and probing to get at the important quantities like phase and state distribution. I think atomic physicists will be able to add a new perspective on many helium experiments in the near future.

This thesis focuses mainly on double condensate experiments, including mean-field interactions and relative phase measurements. Chapter 2 begins with finite temperature excitations, the only remnant of the first BEC apparatus not covered by Ensher [61]. Chapters 3 and 4 focus on two-photon and imaging technology respectively, with emphasis on double condensate experiments. The remaining chapters cover mean-field interactions (Chapter 5), the measurement of relative phase (Chapter 6), creation and evolution due to a gradient in phase across the condensate (Chapter 7), and creation of a vortex state (Chapter 8).

Chapter 2

Finite Temperature excitations [1]

Bose-Einstein condensation in a dilute atomic vapor [36, 54, 43] has been the subject of several experimental studies characterizing this weakly-interacting quantum fluid. In particular, measurements of interparticle interactions and the low-lying collective excitations of the condensate [91, 92, 79, 107] show excellent agreement with theoretical predictions based on a mean-field description of the condensate. This ability to make quantitative comparison between experiment and theory is one of the primary advantages of BEC in a dilute atomic gas. Previous excitation measurements were performed in a regime for which there is no detectable non-condensate fraction. This chapter expands the study of low-lying collective excitations of condensates to include higher temperatures, a regime where theoretical predictions do not yet exist. At these temperatures the interplay between condensate and non-condensate components, a potentially dissipative process not included in the usual mean-field theoretical treatment [81, 128, 59, 112, 51, 62, 66, 127, 135, 104, 67, 85, 109], strongly affects the physics. We find large energy shifts and unexpected structure in the condensate excitation spectrum, as well as a damping rate which plummets with decreasing temperature. These dramatic temperature effects have been met with interest from the theoretical community [65, 82, 103, 115, 122, 125, 126].

The apparatus and techniques used for creating a Bose-condensed sample in a dilute atomic gas of ^{87}Rb [36, 114, 113], accurately determining its temperature [60], and probing the spectrum of low-lying collective excitations [91] are described elsewhere. We first optically trap and cool the atoms, then load them into a purely magnetic TOP (Time-averaged Orbiting Potential) trap [114]. This trap provides a cylindrically symmetric, harmonic confinement potential. Cooling the atoms in the TOP trap proceeds by forced evaporation, whereby an applied weak radio-frequency (rf) magnetic field induces Zeeman transitions to untrapped spin states [77]. The final temperature is controlled by the final frequency of the rf field. The atom cloud is observed by absorption imaging, in which the shadow of the atomic cloud is imaged onto a charge-coupled device array. To circumvent limitations of optical imaging resolution we allow the atom cloud to expand freely for 10 ms before imaging [36, 91].

The condensates are produced in a trap with radial frequency ν_r =129 Hz (365 Hz axial), with the same evaporation parameters as used in our recent quantitative study of the BEC phase transition [60]. We thus perform finite-temperature studies of condensate excitations in a well-characterized system, complementing our previous low-temperature study of collective excitations which examined the dependence on relative interaction strength. We report our results as a function of reduced temperature $T' \equiv T/T_o$, where T_o is the predicted BEC transition temperature for a harmonically confined ideal gas [7]. The estimated systematic uncertainty in T' is 5% for $T' > 0.6$, and 10% for $T' < 0.6$. At $T' < 0.6$ the non-condensate component becomes unobservably small and the temperature is inferred from the final frequency of the rf field. The lowest attainable T' is limited by the evaporation parameters and the extended size of the condensate; deeper evaporative cuts quickly reduce the number of atoms in the condensate. While plotting our results as a function of T', we emphasize that the evaporative cooling process changes the total number of atoms as well as the temperature. Fig. 1

shows various quantities relevant for our particular evaporation parameters.

The basic spectroscopic approach for studying collective excitations follows Ref. [91]. First, a small applied sinusoidal, time-dependent perturbation to the transverse trap potential distorts the cloud. We then turn off the perturbation and the cloud freely oscillates in the unperturbed trap. Finally, the cloud is suddenly allowed to expand and the resulting cloud shape imaged. The symmetry of the drive perturbation can be varied in order to match the symmetry of a particular condensate mode. The modes are labeled by their angular momentum projection m on the trap axis. In this work, we examine the previously observed $m = 0$ and $m = 2$ modes [91, 107]. Frequency, amplitude, and damping rate of the excitations are determined as shown in Fig. 2.1 . The main results of this work are shown in Fig. 2.3. For these data, the perturbative drive pulse duration was typically 14 ms, with the center frequency set to match the frequency of the excitation being studied. The response amplitudes (defined in caption for Fig. 2.2) for these data were kept small, between 5 and 15%. The radial trap frequency ν_r is calibrated by driving a $m = 1$, or "sloshing", excitation of a cloud at $T' = 1.3$. Interatomic interactions should not affect this excitation which consists solely of rigid-body center-of-mass translation. We have also checked that anharmonicities in the confining potential are negligible in our measurements.

The normalized response frequencies as a function of T' are shown in Fig. 2.3a. Collective excitations of a non-interacting cloud should occur at twice the trap frequency (dashed line). Indeed, above the BEC phase transition, the $m = 0$ and $m = 2$ excitations are basically degenerate at $\nu/\nu_r \approx 2$. The non-condensate frequencies are consistently about 1% higher than $2\nu_r$, presumably because interactions are not completely negligible even at the relatively low densities of these clouds [8]. The non-condensate excitation frequencies do not vary significantly with temperature, even for $T' < 1$.

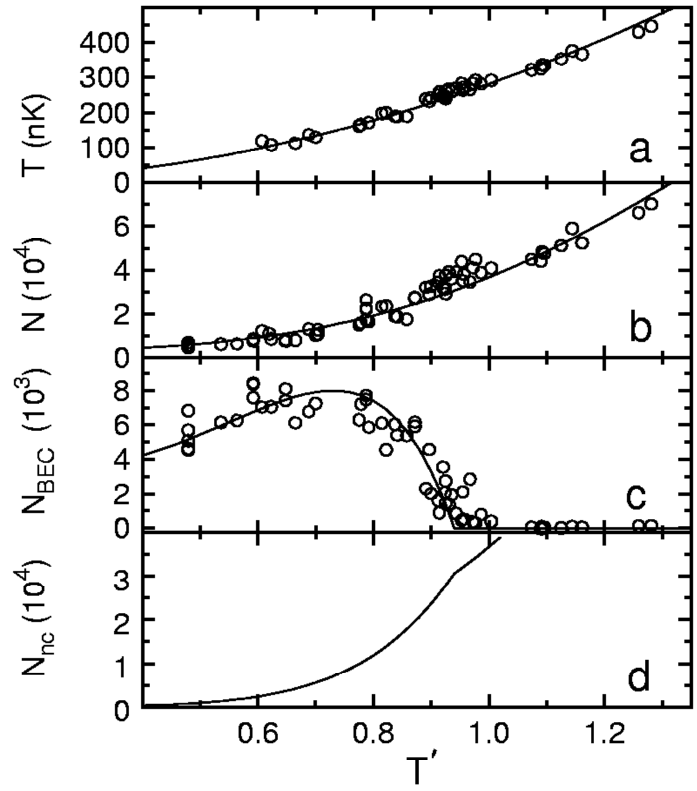

Figure 2.1: We plot temperature T (a) and total number of atoms N (b) as a function of normalized temperature T'. The relationship between N and T is not fundamental but rather a consequence of our evaporative trajectory. In (c) we plot the number of condensate atoms N_{BEC} and in (d) the inferred non-condensate number N_{nc}. Because of their different spatial extents, the peak density of the condensate component is an order of magnitude larger than that of the non-condensate component below $T' \approx 0.9$.

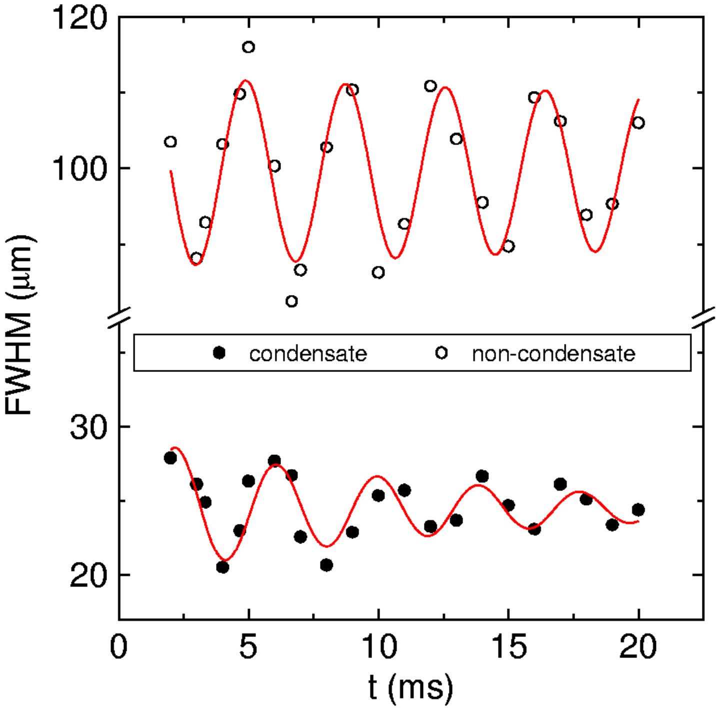

Figure 2.2: In this example, we plot the observed widths, obtained from 2-Gaussian surface fits to absorption images, of a $T' = 0.79$ cloud with an $m = 0$ excitation. The widths of each component, condensate and non-condensate, of the freely oscillating cloud are fit by an exponentially damped sine wave: $Aexp(-\gamma t)sin(2\pi\nu t + \phi) + B$, from which we obtain the response frequency ν, initial fractional amplitude A/B, and decay rate γ. For each pair of points (condensate and non-condensate widths) a fresh cloud of atoms is cooled, excited, and allowed to evolve a time t before a single destructive measurement.

In contrast, the excitation spectrum of the condensate exhibits strong temperature dependence. While some frequency shift might be expected because of the temperature dependence of the number of condensate atoms (see Fig. 2.4), and therefore the relative interaction strength, the magnitude of the observed temperature-dependent frequency shifts is several times larger than that observed due to interaction effects [91]. In addition, the frequencies of these two modes, which are degenerate in the limit of zero interactions, actually shift in opposite directions, with only the $m = 0$ heading to the non-interacting limit. A sharp change is apparent in the slope of the temperature dependence of the $m = 0$ excitation frequency. Repeated measurements confirm that this distinct feature at $T' \approx 0.62$ reproduces. We speculate this might arise from coupling with another mode, perhaps with a strongly temperature-dependent second-sound excitation or with the excitation of the non-condensate component. No corresponding distinct feature is evident in the temperature dependence of the $m = 2$ condensate excitation frequency.

Fig. 2.3b presents the decay rate γ as a function of temperature. While the frequencies of the two condensate modes behave very differently, their decay rates appear to fall on a single curve, with γ quickly decreasing with decreasing T' [9]. Another remarkable feature is that for temperatures where two-component clouds are observed, the condensate excitations damp much faster than their non-condensate counterparts (see also Fig. 2.2). The strong temperature dependence suggests that finite decay times reported in Refs. [91] and [107] were due to the finite temperature of the samples and that condensate excitations may persist for very long times at lower T'.

In the limit of low amplitude response, the measured spectrum corresponds to the elementary excitations of BEC in a dilute gas. At our lowest temperature, $T' \approx 0.48$, we examine the condensate excitations as a function of increasing

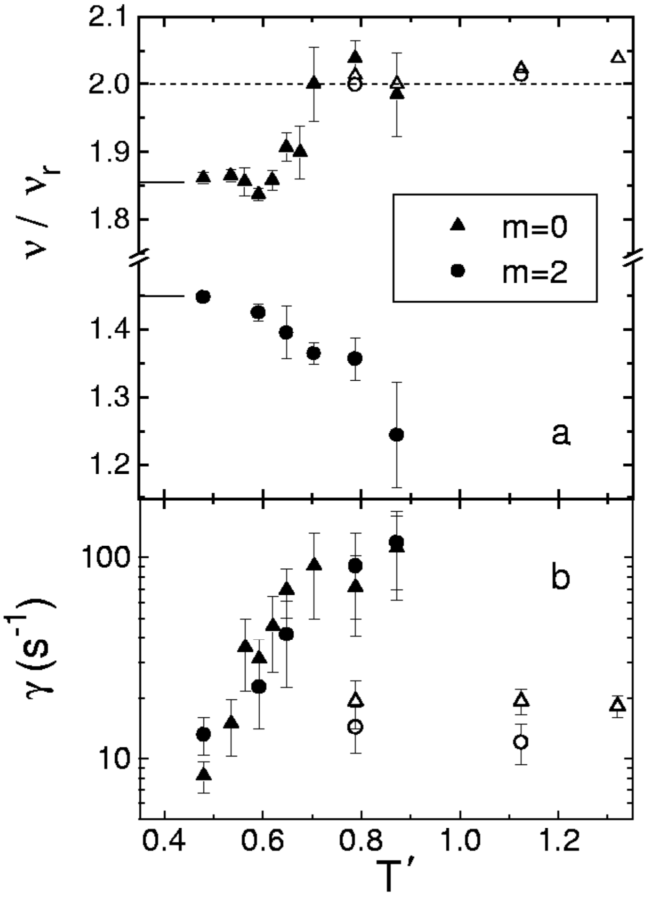

Figure 2.3: Temperature-dependent excitation spectrum: (a) Frequencies (normalized by the radial trap frequency) for $m = 0$ (triangles) and $m = 2$ (circles) collective excitation symmetries are shown as a function of normalized temperature T'. Oscillations of both the condensate (solid symbols) and non-condensate (open symbols) clouds are observed. Short lines extending from the left side of the plot mark the mean-field theoretical predictions in the $T = 0$ limit (for 6000 atoms in our trap) [8]. (b) For both the $m = 0$ and $m = 2$ condensate excitations the damping rate γ quickly decreases with decreasing temperature.

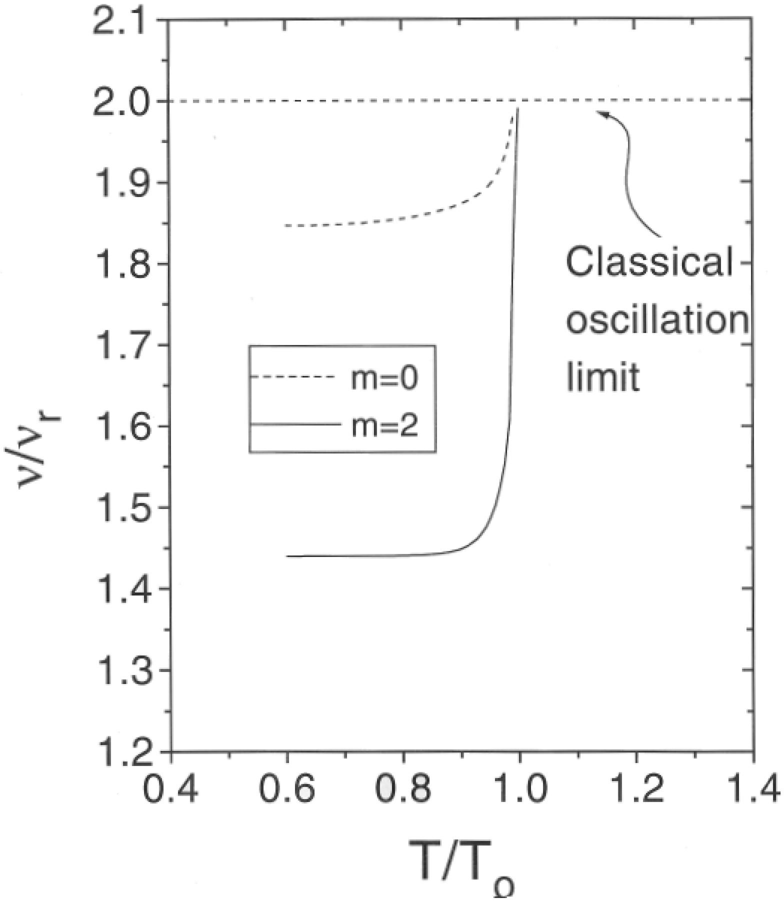

Figure 2.4: A simple model based on the theory by Edwards [59], which only takes into account the change in mean field due to the changing number of atoms in the condensate as a function of temperature.

response amplitude. The $m = 0$ mode exhibits a significantly smaller anharmonic frequency shift than the mode with $m = 2$ symmetry (Fig. 2.5a). The decay rates γ for the $m = 0$ and $m = 2$ condensate excitations show some dependence on response amplitude (Fig. 2.5b), but in neither case does γ approach zero in the limit of small response. These data demonstrate that ν and γ measured for a typical response amplitude of 10% are fairly close to the zero-amplitude perturbation limit.

For comparison with the results of our free-evolution spectroscopy technique, Fig. 2.6 presents a more conventional resonance measurement. While the central frequency is in good agreement with that measured from observing the freely oscillating widths as discussed above, the resonance technique is inefficient in terms of data collection time and moreover vulnerable to systematic errors, particularly when one tries to extract a damping rate from the linewidth.

This experiment extends previous studies of condensate excitations to temperatures for which both condensate and non-condensate atoms are present in significant numbers. This regime is not yet well understood theoretically, as the standard mean-field theoretical treatment of collective excitations of a harmonically confined dilute BEC is done for the $T = 0$ limit and does not include dissipation. Both $m = 0$ and $m = 2$ condensate modes exhibit large temperature-dependent frequency shifts. The decay rate of the condensate collective excitations decreases rapidly with temperature, and shows no signs of leveling off. More recently, there have been further theoretical investigations into finite temperature modes [56, 73, 110].

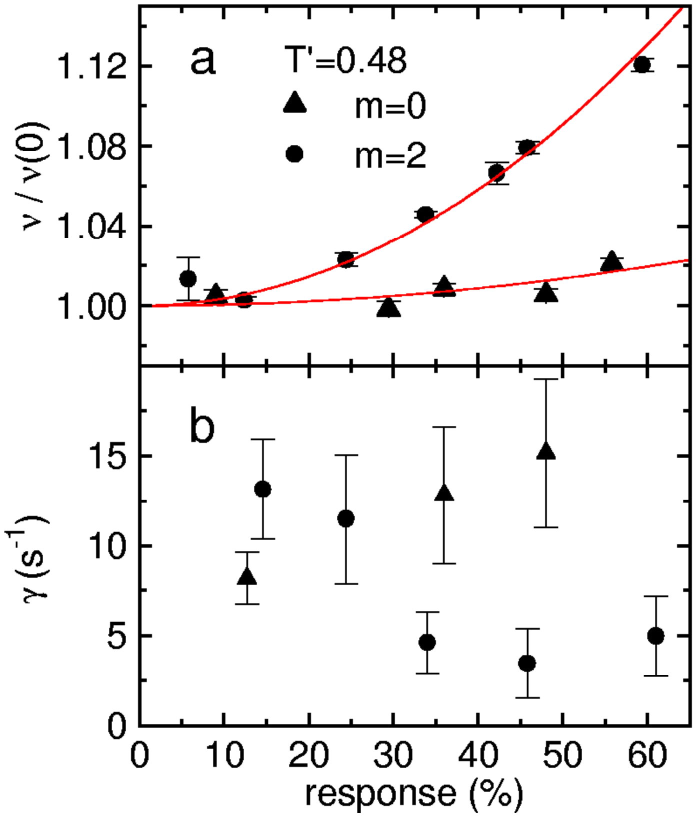

Figure 2.5: For large response amplitudes at our lowest temperature, $T' \approx 0.48$, we measure the shift in the response frequency ν and damping rate γ. In (a) the frequencies, normalized by the small drive limit, show a larger anharmonic shift for the $m = 2$ condensate excitation than for the $m = 0$ case. (Some of the $m = 2$ data is the same as presented in Ref. 4 and is reproduced here to facilitate comparison.) Solid lines are guides to the eye. In (b) the decay rates γ for the $m = 0$ and $m = 2$ condensate modes shift in opposite directions with increasing response amplitude.

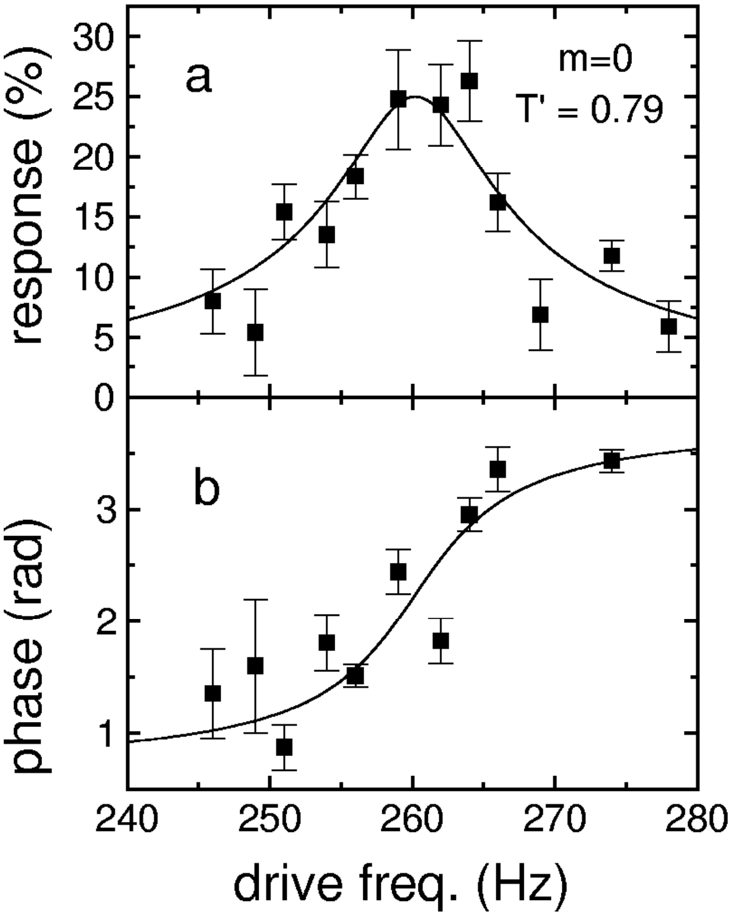

Figure 2.6: The response of the $m = 0$ condensate excitation at $T' = 0.79$ as a function of the center drive frequency. Solid lines show fits to the expected form for the amplitude (a) and phase (b) of a driven harmonic oscillator in the presence of damping. For these measurements a constant amplitude drive is applied with a duration of 150 ms (about 7 Hz FWHM in frequency), after which the resulting excitation is observed for 10 ms to determine amplitude and phase.

Chapter 3

Two-Photon transition

3.1 Introduction

One of the unique qualities of degenerate quantum systems is that all particles share the same phase. Although this phase is random between successively created condensates, the phase remains coherent over time for each production of a condensate [41, 58, 89, 90, 99, 102]. This is only true in the absence of external effects, such as thermal atoms and magnetic field variations. Investigation of phase properties requires the presence of another object which can interfere with the condensate in order to make the phase observable. The internal states of ^{87}Rb prove very useful, in that standard atomic physics magnetic-resonance techniques can be employed for interferometry. For experiments on trapped condensates the internal states used must have the same sign and magnitude of $\partial E/\partial B$ (the magnetic moment) in order that the states overlap spatially. Only the $|1,-1\rangle$ and $|2,1\rangle$ states satisfy this. This chapter describes the two-photon transition first for a free atom in a uniform magnetic field, then for the complicated case of a confined atom in a time dependent magnetic field.

3.2 Transition for a free atom

The levels $|1,-1\rangle$ and $|2,1\rangle$ (hereafter called $|1,-1\rangle$ and $|2,1\rangle$ respectively) have the same magnetic moment to first order, and are separated by the hyperfine splitting ν_{hs} ~6.8 GHz. A two-photon drive is required since there are two units of angular momentum between them. Fig. 3.1 shows the $5S_{1/2}$ $F=1$ and $F=2$ ground states of ^{87}Rb in a small magnetic field which produces splittings of ~ 0.7 MHz/G between adjacent Zeeman levels. Also shown are the radio-frequency (~ 1 MHz) and microwave (~ 6.8 GHz) photons and their relative detunings. When the intermediate detuning is larger than the Rabi frequencies of the two level microwave and rf transitions ($\Omega^2_{-1\rightarrow 0}$ and $\Omega^2_{0\rightarrow 2} \ll \Delta^2$) then the probability for a transition to the intermediate state $|2,0\rangle$ is small. The three-level system can then be treated as a two-level system [68] with a Rabi frequency

$$\Omega_0 \equiv \frac{\Omega_{-1\rightarrow 0}\Omega_{0\rightarrow 2}}{2\Delta_{\mathrm{IM}}}. \tag{3.1}$$

where all Ω are bare Rabi frequencies and Δ_{IM} is the detuning from the intermediate state. For arbitrary two-photon polarizations and Δ multiple paths must be considered to avoid interference or transitions to untrapped states. As an example, another possible arrangement is a microwave detuning below the $|2,0\rangle$ state and increasing the rf energy. This opens up path to the $|2,-2\rangle$ state through the $|2,-1\rangle$ intermediate state if the required polarizations are present. Likewise, increasing the microwave frequency so that the intermediate state is higher in energy than the $|2,1\rangle$, and changing the rf correspondingly, opens another path to the same final state $|2,1\rangle$, but through the $|1,0\rangle$, causing interference. The states $|2,1\rangle$ and $|1,-1\rangle$ are sufficiently long lived that the linewidth is interaction time limited, meaning it is possible to measure the transition frequency to $\sim$ 10Hz. At this level the transitions have magnetic field dependence given by the Breit-Rabi formula

$$\nu(B) = -\frac{\nu_{hs}}{8} - g_I\frac{\mu_n}{h}Bm_F \pm \frac{\nu_{hs}}{2}\sqrt{1+m_F x(B) + x^2(B)} \tag{3.2}$$

$$x(B) = (g_J + \frac{g_I}{M_r})\frac{\mu_b}{\nu_{hs}h}B \tag{3.3}$$

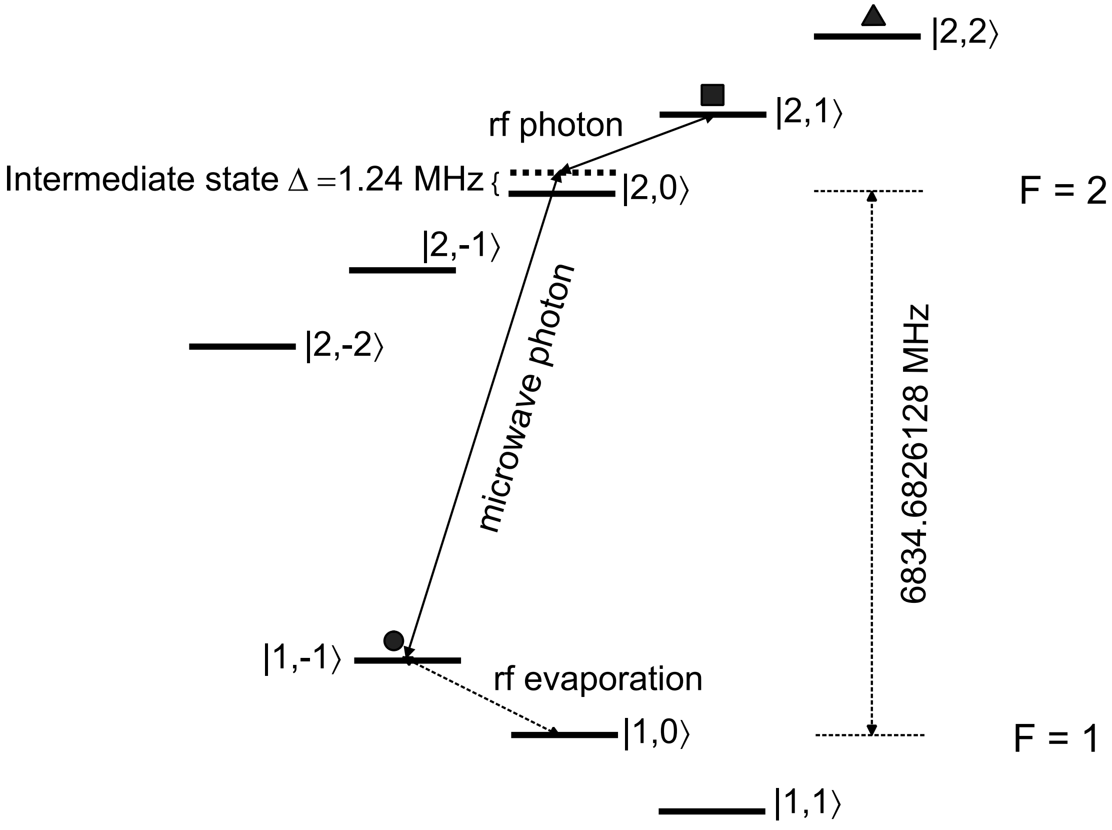

Figure 3.1: The ground states of ^{87}Rb in a small magnetic field. The states marked with squares have nearly the same magnetic moment. The state marked with the triangle is the only other trapped, but with twice the confinement of the other two. Microwave and rf photons couple the two states through an intermediate level.

$\frac{\mu_b}{h}$	1.399624 MHz/G
$\frac{\mu_n}{h}$	762.2591 Hz/G
$M_r = \frac{m_p}{m_e}$	1836.152701
g_I	$2.75124 \times \frac{2}{3}$
g_J	$2.002319 \times 1.0000059$
h	$6.6260755 \times 10^{-27}$ erg·s
ν_{hs}	6834.6826128 MHz [39]

Table 3.1: Useful constants

where the plus (minus) sign is used for $F = 2$ ($F = 1$) and the fundamental values in table 3.1 are useful [35]. This equation is exact for purposes here; the sphericity of the electronic orbit means that the field gradient at the nucleus is zero, giving no interaction with the nuclear charge distribution. All other interaction terms vanish by symmetry arguments, up to the small magnetic octupole moment [121].

Expansion of the function of $x(B)$ in Eq. 3.2 about small $x(B)$ is valid when the Zeeman splitting is small compared to the hyperfine splitting ($\mu_b B \ll h\nu_{hs}$), yielding the useful approximation for the frequency of any state

$$\begin{aligned} \nu(B) &= (-\frac{1}{8} \pm \frac{1}{2})\nu_{hs} + \left(-g_I\frac{\mu_n}{h} \pm \frac{1}{4}(g_J + \frac{g_I}{M_r})\frac{\mu_b}{h}\right) m_F B \\ &\pm \frac{1}{4\nu_{hs}}(1 - \frac{m_F}{4})\left((g_J + \frac{g_I}{M_r})\frac{\mu_b}{h}B\right)^2 . \end{aligned} \tag{3.4}$$

This evaluates to the simple expression for the transition frequency between $|1,-1\rangle$ and $|2,1\rangle$, good to < 1Hz up to $B =$20G

$$\Delta\nu(B) = -2796.21B + 431.361B^2 + \nu_{hs}. \tag{3.5}$$

Eq. 3.5 is plotted in Fig. 3.2. The setup for driving the two-photon transition is shown in Fig. 3.3. Rf is applied through the same path as the evaporation rf; capacitively coupled onto the top quadrupole coil. Microwave is applied through a sawed-off waveguide of cross-section 2.2 cm by 1.0 cm, ~15 cm long, and ~3 cm from the center of the cell to the end of the guide. The cutoff frequency for the

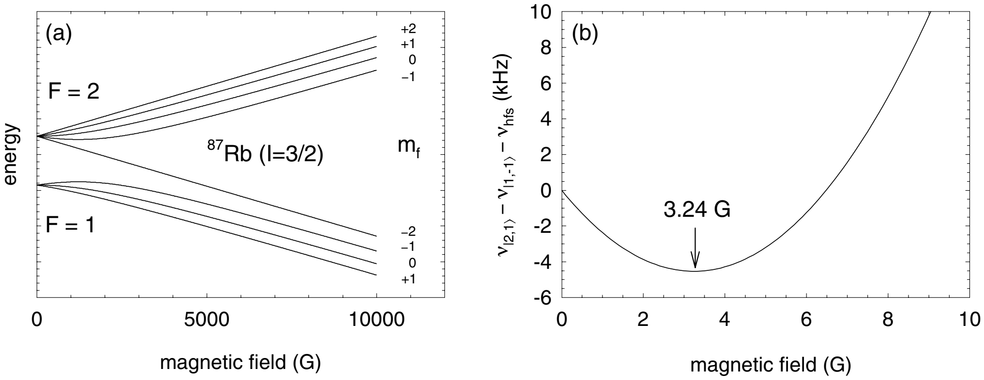

Figure 3.2: (a) The hyperfine and Zeeman levels as a function of bias field. The frequency splitting at B=0 is ν_{hs}. Figure (b) shows the energy difference between $|1,-1\rangle$ and $|2,1\rangle$, where the energy difference at B=0 has been subtracted. At the special field value of $B = 3.24$G the transition has no field dependence.

TE_{10} mode is 6.82 GHz ($\lambda = 4.4$ cm) [86]. Magnetic field polarization is along the long direction of the waveguide, or out of the page in Fig. 3.3, in the same direction as the rf. Since the quantization axis of a trapped atom is parallel to the page (rotating with the TOP field), this configuration provides equal amounts of $\sigma+$ and $\sigma-$ microwave and rf for all angles of the TOP field. Unfortunately, the presence of other conduction objects near the trap (coil supports, copper coils) distort the microwave field in an unknown way. Power is applied to the waveguide through rigid coax from a Hughes traveling-wave tube amplifier (20W), which is driven by an HP 8672A frequency source. Since our expected precision was $\sim$ 1 part in 10^{10}, and we wanted the option of making absolute frequency measurements, the HP source was locked to an HP58503A GPS receiver with root Allen variance of $\sim 1 \times 10^{-12}$ over 1 second (10MHz signal). Before the amplifier input is a microwave switch for fast turn on. The amplifier output passes first through a high power directional coupler to prevent damaging reflections, then through a power splitter in reverse. The splitter takes power from the reflected wave to a square law detector for measuring the power on a scope.

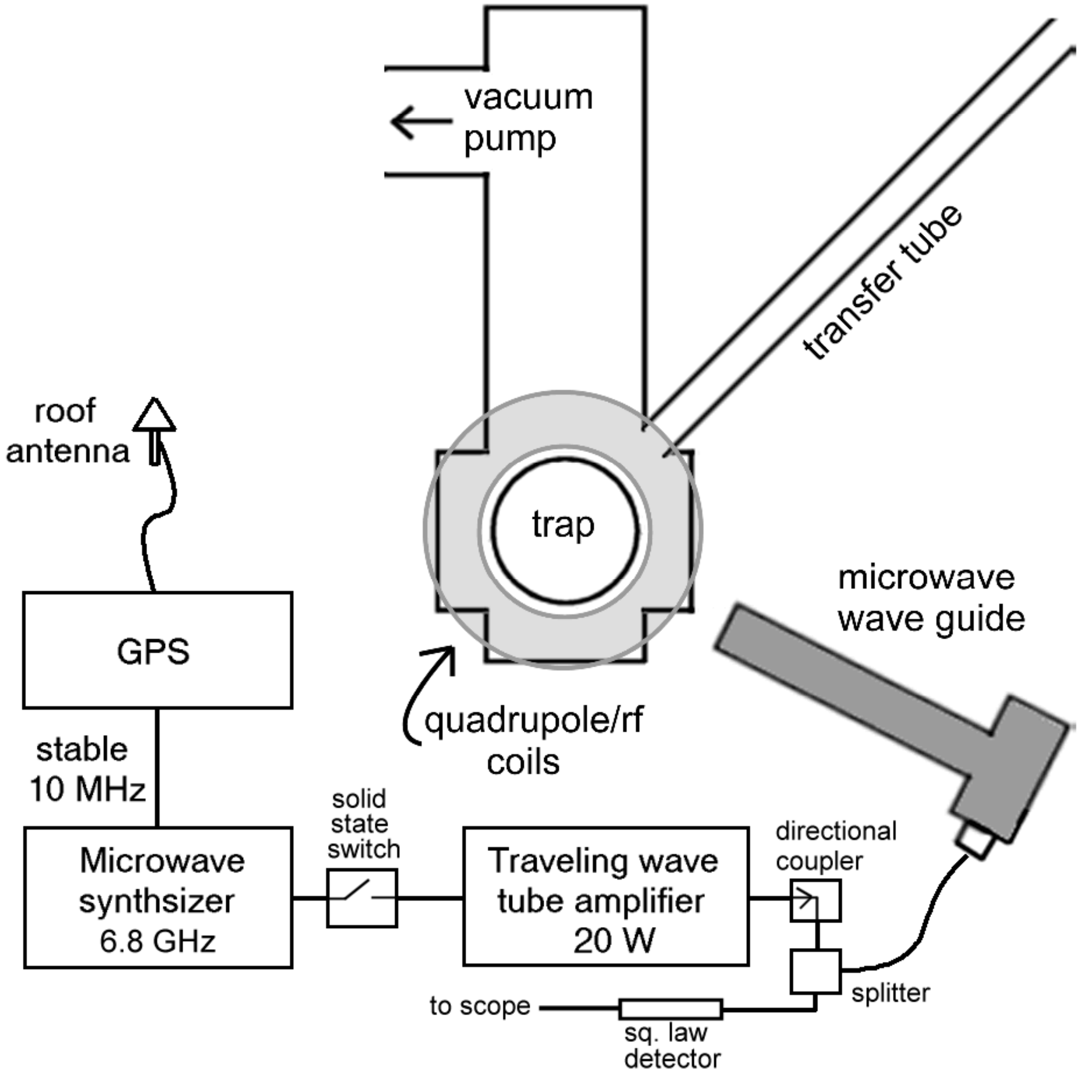

Figure 3.3: The position of the microwave waveguide is shown relative to the trap. Rf is capacitavly coupled to the top quadrupole coil (it is the same as the evaporation rf)

.

The rf is generated either by the rf synthesizer used for evaporation, or a separate synthesizer if the frequency switching time is not fast enough to go between evaporation and the two-photon drive. An rf switch is used to toggle between the two synthesizers. The remainder of the rf path is the same as for evaporation. Stability requirements for the rf are easily met by the devices without externally locking to the 10MHz GPS signal (although we do anyway).

For general superposition experiments, the rf and microwave pulses must be short compared to the trap frequency so that no density evolution occurs during the population transfer. Other experiments require arbitrary pulse sequences and timings. We use a programmable HP8672A for this task. Following is a description of the general timing for two-photon pulses. See [61] for details on condensate creation.

Programming of the HP8672A can easily require a few seconds of time given the 100 commands that must be uploaded for complex pulse sequences. This is done in two pieces; one after a command is changed from the experiment-computer keyboard, and the other once the experiment run has begun (after the atoms are transferred into the TOP trap). At this time the amplitude and frequency of various synthesizers is set, and the HP8176A is awaiting a trigger to begin its pulse sequence . Evaporation proceeds and a nearly pure condensate is created in the $F = 1, m_F = -1$ state. The trap can then be ramped to achieve the desired confinement. After things have settled (quadrupole coil temperature for example) a trigger from the computer is sent to the AF synchronization box, which outputs a trigger to the HP8176A only when the TOP field has a specific phase. This way all experiments are locked to the rotating TOP field, so that specific events will occur at the same field direction. This is critical for destructive, near-resonance imaging, obtaining a repeatable position of a dropped condensate, and keeping strange sideband behavior constant (see the Tilted TOP section in this chapter).

Fig. 3.4 shows a timing diagram for a simple separated oscillatory field experiment containing two two-photon pulses.

For initial experiments we drove single-photon microwave transitions from a dropped (B'_q turned to zero) condensate in the $|1, -1\rangle$ state to the $F = 2$ states. Initial linewidths were $\sim$ .3MHz, making this a fair probe of magnetic field magnitude. This is interesting for calibration issues, especially one of rounding the rotating TOP field. Single-photon rf or microwave transitions means they are field sensitive at 0.7 MHz/G for rf drives, and multiples (up to 3) of .7 MHz/G for microwave. Given that the linewidth is interaction time limited, and that the drive must be on for, at most, 1/4 of a TOP rotation to sample only a given angle, means that the transition width is $4\nu_{TOP}$. This effectively detects a field difference of $\frac{4}{10}\nu_{TOP}/.7 \times 10^6$Hz if the line can be split to 1 in 10. For a 7.2kHz rotation frequency this means an eccentricity of 4mG can be observed in the best case scenario.

The two-photon resonance from $|1, -1\rangle$ to $|2, 1\rangle$ was easily observed by applying both rf and microwave drives for a few milliseconds and observing the atoms in the $F = 2$ levels. Figure 3.5 shows typical data. Sidebands are a common feature in these lineshapes and are separated from the main peak by the TOP rotation frequency. An asymmetry is very common, with the right sideband larger than the left. This will be covered in more detail later.

Ramsey's method of separated oscillatory fields [121] was also employed for a host of frequency measurements in characterizing the system. Two common implementations are shown in Fig. 3.6 for dropped condensates. Graph 3.6(a) shows the signal as the time between two $\pi/2$ pulses of length 278 μs is changed, and the two-photon drive is detuned by 850 Hz. The observed oscillation frequency is the difference between the atomic splitting and the drive. Essentially, this is a comparison of the rate of phase accumulation (energy) between the synthesizer

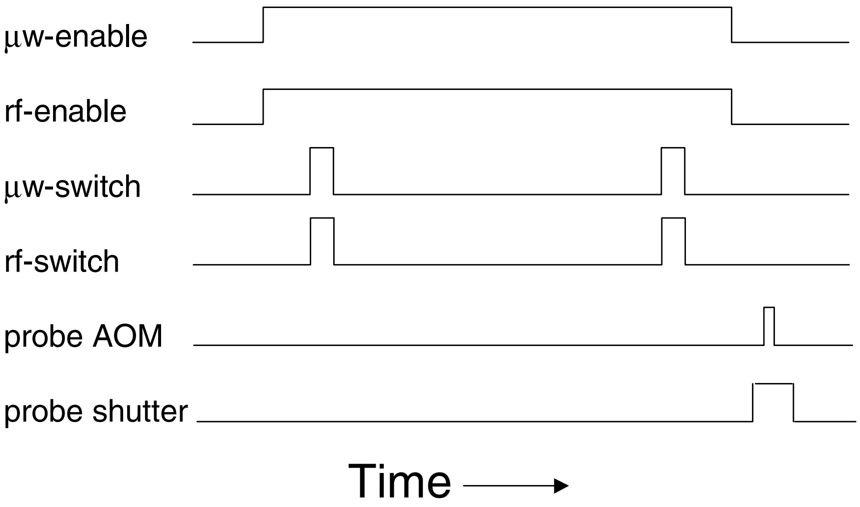

Figure 3.4: A basic timing diagram for a two-pulse experiment. The microwave and rf switch pulses can be any desired length, but are ∼1ms for most π-pulses.

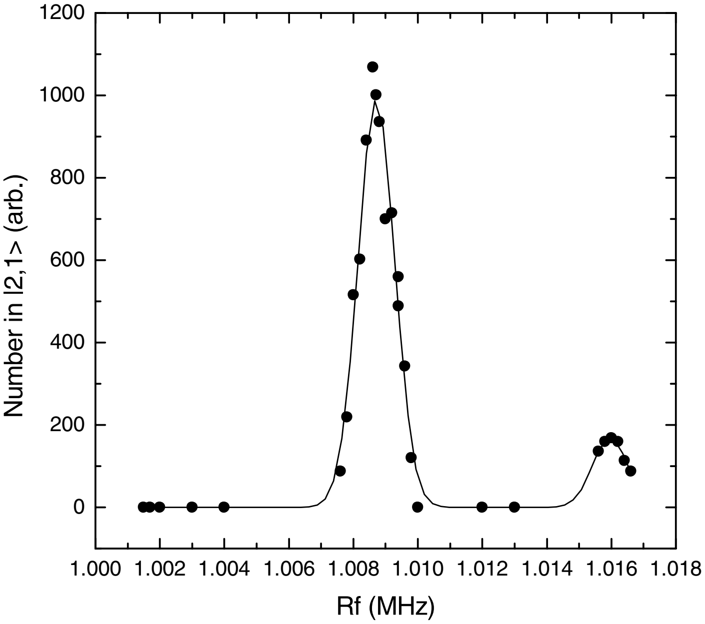

Figure 3.5: A typical Rabi lineshape for the two-photon resonance in a dropped condensate. The microwave is 6833.668 MHz, and the pulse is 690μs long. The sideband is separated by ∼7.2 kHz, equal to the TOP rotation frequency.

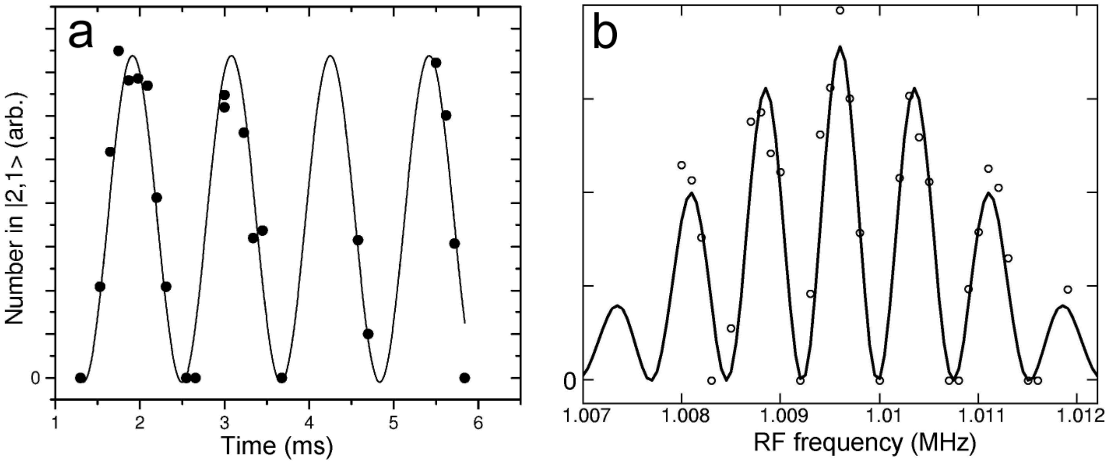

Figure 3.6: Ramsey's method of separated oscillatory fields by changing the time between (a) or the frequency of (b) the two pulses. (a) The fit frequency gives the detuning between the drive and the atomic transition. (b) The solid line is a fit with adjustable amplitude and central frequency.

and the condensate, during the time between the pulses. The mean-field energy is the same for each point in this case; the system is in the same superposition of the two states for each data point. A more common case is shown in Fig. 3.6(b), in which the time between the pulses is constant at 1.02 ms, but the drive frequency changes. Since the superposition changes as a function of detuning, a systematic broadening could occur if the mean-field energy of the two states were unequal. The first case is used extensively in the following chapters as calibration of field amplitudes and in measuring phase properties of a condensate.

3.3 Transition for a trapped condensate

The preceding analysis is sufficient for a static magnetic trap. Additional complications arise, however, when a time-dependent magnetic trap (such as the TOP trap) is used to provide the confinement. Referred to as the "Weird Bohn Effect", the time dependence leads to an additional effective static magnetic field which yields energy level shifts and vertical offsets between $|1,-1\rangle$ and $|2,1\rangle$. It has become a useful tool in double-condensate systems.

3.3.1 Quantum mechanical derivation

The TOP trap involves a magnetic field of magnitude B_0 rotating counterclockwise (as viewed from the positive z-axis) at angular frequency ω_t in the xy-plane,

$$\mathbf{B_0}(t) = B_0(\cos\omega_t t\hat{\mathbf{x}} + \sin\omega_t t\hat{\mathbf{y}}). \tag{3.6}$$

The effective Hamiltonian in a frame co-rotating with the magnetic field transforms as

$$\hat{H}_{\text{eff}} = R(-\omega_t t)\hat{H}_{\text{BR}}R^\dagger(-\omega_t t) - i\hbar R^\dagger(-\omega_t t)\frac{\partial}{\partial t}R(-\omega_t t) \tag{3.7}$$

with the time-dependent rotation operator R defined by

$$R(-\omega_t t) = \exp(\frac{i}{\hbar}F_z\omega_t t). \tag{3.8}$$

The operator F_z is the z-component of the total (nuclear plus electronic) spin vector, and the sign of the argument of R is chosen to rotate the coordinate axes in the same sense as the field. The Breit-Rabi Hamiltonian $\hat{H}_{\text{BR}}$ (with eigenvalues Eq.3.2) is invariant under the transformation. We therefore obtain

$$\hat{H}_{\text{eff}} = \hat{H}_{\text{BR}} - F_z\omega_t. \tag{3.9}$$

The expectation value of this operator on a state $|F, m_F\rangle$ is

$$\begin{aligned} \langle F, m_F|\,\hat{H}_{\text{eff}}\,|F, m_F\rangle = E_{\text{BR}} - \hbar m_F\omega_t = g_F m_F \mu_B B - \hbar m_F\omega_t \\ g_{F=1} = -\frac{1}{4}g_J - \frac{5}{4M_r}g_I \simeq -\frac{1}{2} \\ g_{F=2} = \frac{1}{4}g_J - \frac{3}{4M_r}g_I \simeq \frac{1}{2} \end{aligned}$$

where E_{BR} is written as only the largest part of Eq. 3.2, *i.e.* the first order Zeeman shift. Interpreting the expectation value of $\hat{H}_{\text{eff}}$ as an effective magnetic field $g_F m_F \mu_B B_{\text{eff}}$, we see that the rotating magnetic field becomes simply another static field contribution:

$$B_{\text{eff}} = B_0 - \frac{\omega_t \hbar}{\mu_B g_F} \tag{3.10}$$

3.3.2 Classical derivation

A classical derivation is more intuitive and yields the same result [121]. The equation of motion for a spin vector $\mathbf{F}$ in a constant magnetic field $\mathbf{B}$ is

$$\hbar \frac{d\mathbf{F}}{dt} = \mu_B g_F \mathbf{F} \times \mathbf{B_0}. \tag{3.11}$$

For magnetic field rotating at $\omega_{\mathbf{t}}$, the time derivative in the rotating frame becomes

$$\frac{d\mathbf{F}}{dt} = \overrightarrow{\omega_t} \times \mathbf{F} + \frac{\partial \mathbf{F}}{\partial t}. \tag{3.12}$$

Combining these two and solving for the motion of the vector in the rotating frame gives

$$\begin{aligned} \hbar \frac{\partial \mathbf{F}}{\partial t} &= \mu_B g_F \mathbf{F} \times \mathbf{B}_{\text{eff}} \\ \mathbf{B}_{\text{eff}} &= \mathbf{B_0} + \mathbf{B}_\omega \\ \mathbf{B}_\omega &\equiv \frac{\hbar \overrightarrow{\omega_t}}{\mu_B g_F} \end{aligned} \tag{3.13}$$

which is the same as Eq. 3.10. This extra static field can be interpreted as an imaginary field which causes the spin vector to precess at a Larmor frequency ω_t. The magnitude of B_ω is only 2.6 mG for $\omega_t = 1.8$kHz, but switches sign for the two different hyperfine states. However since $\mathbf{B}_\omega$ is perpendicular to $\mathbf{B_0}$, the total field magnitude remains constant in this picture. Only when another field with some component along $\mathbf{B}_\omega$ is present does this modify the actual magnitude, and hence two-photon transition energy. This is the case for an untrapped condensate, as long as there is an external field along $\mathbf{B}_\omega$. The total field is

$$|B_{\text{total}}| = \sqrt{B_0^2 + (B_z \pm B_\omega)^2} \tag{3.14}$$

where B_z is an external uniform field in the same direction as B_ω and the plus (minus) sign is used for the $|2,1\rangle$ ($|1,-1\rangle$). The field for each state from Eq. 3.14 must be used in Eq. 3.4, and the difference taken to find the transition frequency. A useful approximation for the transition frequency is

$$\Delta\nu = -2796.21 B_0 + 431.361 B_0^2 + 699579 \frac{B_\omega B_z}{B_0} \tag{3.15}$$

valid for $B_0 \gg B_\omega, B_z$. The first data investigating this effect was taken using condensates dropped from the trap, so that the magnetic gradient was off and only the rotating field B_0 and background field B_z present. Figure 3.7 shows this data and plots of the exact version of 3.15 for different directions of B_0 rotation (or equivalently, different signs of B_z. The extra term in Eq. 3.15 applies an offset whose magnitude drops off as B_0 dominates the total field.

The situation is similar for a trapped condensate, except that the confining gradient provides B_z. In the TOP trap gravity displaces the equilibrium position of the condensate from $z = 0$. The total instantaneous field at any point in the trap is

$$|B_{\text{total}}(z)| = \sqrt{(B_0 \cos(\omega_t t) + \frac{B_q'}{2} x)^2 \hat{\mathbf{x}} + (B_0 \sin(\omega_t) + \frac{B_q'}{2} y)^2 \hat{\mathbf{y}} + (-B_q' z \pm B_\omega)^2 \hat{\mathbf{z}}}. \tag{3.16}$$

Figure 3.8 shows graphically the orientation of the fields in the TOP trap. The imaginary field B_ω points along $\overrightarrow{\omega}$. Since $z \neq 0$ when gravity is included the effect of B_w is to modify the vertical quadrupole gradient with an offset. This can be rewritten as an offset in z, *i.e.* ,

$$\begin{aligned} (-B_q' z \pm B_\omega)^2 &= (-B_q'(z \pm z_\omega))^2 \\ z_\omega &\equiv \frac{B_\omega}{B_q'} \end{aligned}$$

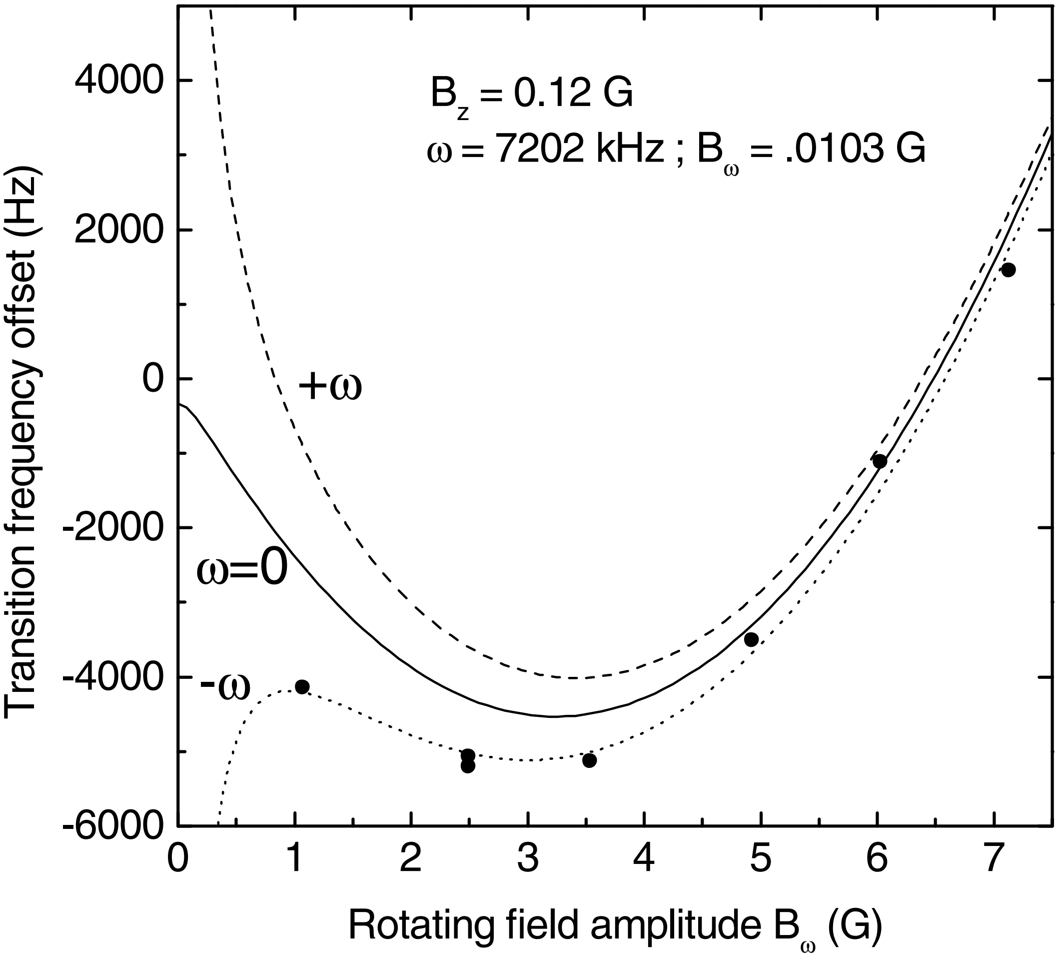

Figure 3.7: The data points are for a dropped condensate. The frequency of rotation of B_0 is 7.2 kHz and the vertical component of the background field B_z is found from a fit of Eq. 3.15. Also shown are the curves for the opposite rotation of B_0 and when there is no rotation.

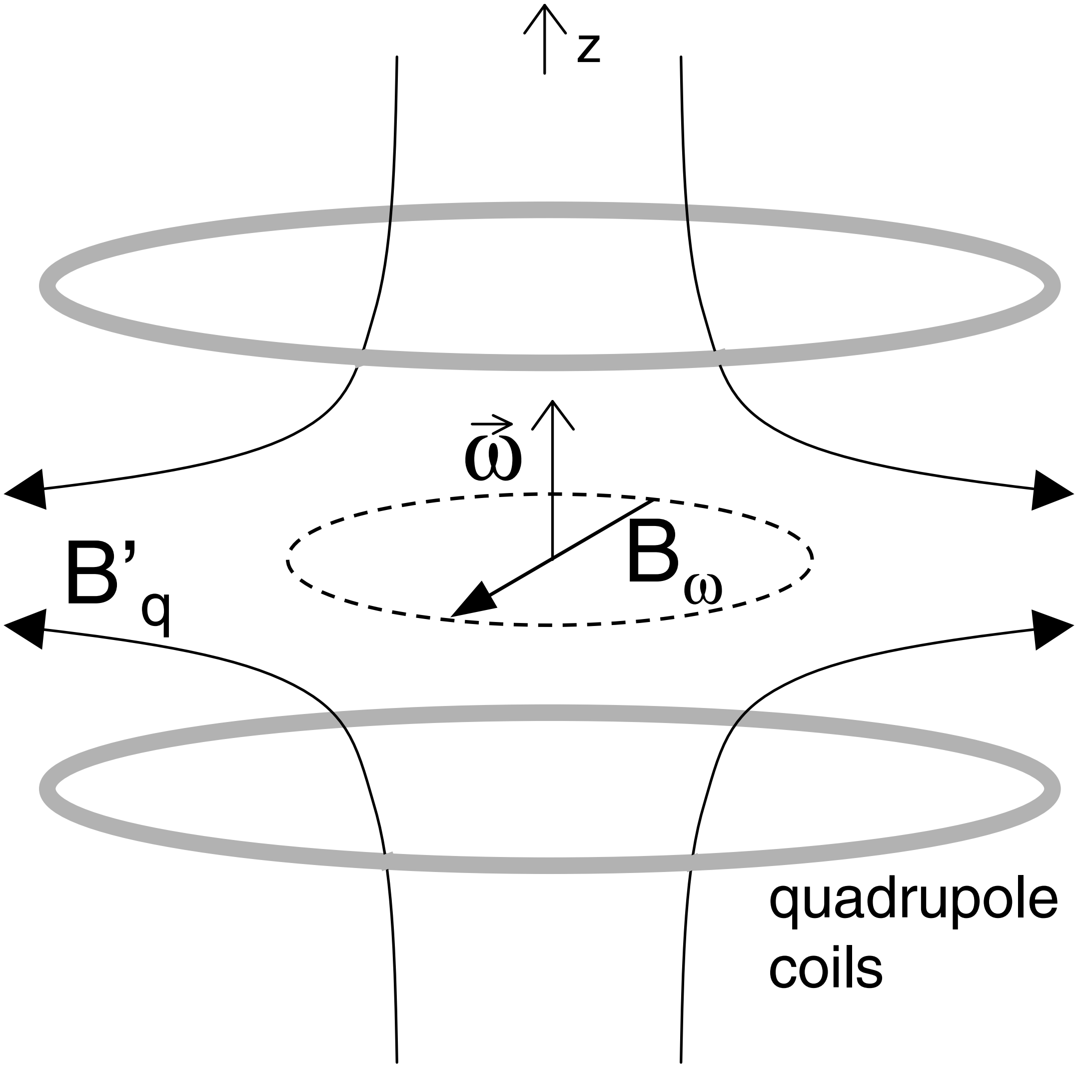

Figure 3.8: Diagram of the magnetic fields in a TOP trap. The curved arrows represent the field line from the quadrupole field B_q produced by the coils. A uniform field B_ω rotates about the central axis, providing an imaginary field B_ω along $\overrightarrow{\omega}$.

It is the total field in Eq. 3.16, along with the position $z \pm z_\omega$ of the atoms in the trap, which must be substituted into Eq. 3.2 to find two-photon transition frequency.

3.3.3 Observable effects

These equations can all be put together to yield useful quantities, such as the relative separation between the states and the transition frequency as a function of trap parameters. For the following quantities, the condensate is assumed to be at its equilibrium position, as defined by the trap parameters B_0, B'_q and B_ω. The following are small effects which are only observable for specific trap geometries, or when looking at differences in large quantities.

In general the position of an atom in a magnetic potential is found by setting the spatial derivative of the total energy to zero. From Eq. 3.2 and Eq. 3.16, the following must be solved for z;

$$\frac{\partial}{\partial z}\left(h\nu(|B_{total}(z)|) + mgz\right) = 0.$$

This is a very complicated equation in z and not easily solved exactly. Using the expansion in Eq. 3.4 gives a quartic equation in the vertical position z whose solution is approximated by the expansion in ϵ

$$\begin{aligned} z &= \mp z_\omega + \frac{B_0}{B'_q}\frac{\eta}{\sqrt{1-\eta^2}} - 2\frac{B_0^2}{B'_q}\frac{\eta}{(1-\eta^2)^2}\epsilon \\ &\quad -2\frac{B_0^3}{B'_q}\frac{3\eta^2+2}{(1-\eta^2)^{\frac{7}{2}}}\epsilon^2 + 16B_0^4\frac{3\eta^3+2\eta}{(1-\eta^2)^4}\epsilon^3 \end{aligned} \tag{3.17}$$

in which $\eta \equiv \frac{mg}{KB'_q}$, $\epsilon \equiv L/K$, and K and L are the coefficients of the linear and quadratic Zeeman terms in Eq. 3.4 respectively. This reduces to Ensher's result (Eq. 6.9 [61]) when the nuclear and higher order Zeeman structure vanish ($\epsilon \to 0$ and $K \to \frac{1}{4}g_J\frac{\mu_B}{h}$). K, L and z_0 depend on the atomic state m_F. The size of the higher order terms is actually quite small compared to zero order. It is only when looking at the difference in vertical position of the two states that these terms play significant role. As will be shown later these differences have quite a large effect in double condensate behavior.

Fig. 3.9 shows the effect of the trap rotation and the higher order magnetic field dependence on the relative vertical position of the two states. The effect of trap rotation is only to apply a vertical offset between the states in Fig. 3.9a. For many double-condensate experiments we are interested in traps where the relative offset is zero so that the condensates completely overlap. Fig. 3.9b is a plot of the rotating field magnitude B_0 necessary for overlap as a function of the quadrupole gradient B'_q. Only a very small range is accessible when the rotating field has a positive direction. Qualitatively the offset from rotation is opposing ($-B_\omega$ case) or enhancing ($+B_\omega$ case) the relative sag caused by the different higher order Zeeman shifts. All of the double-condensate experiments are done with the $-B_\omega$ rotation.

Using Eq. 3.17 for the position of atoms in the trap the absolute magnetic field, and hence the transition frequency, can be found as a function trap parameters. The total field at the equilibrium position of a state is given by the approximation

$$\begin{aligned}
|B_{total}| &= \sqrt{B_0^2 + B_q'^2 z_0^2} - 2B'_q B_0^2 \frac{\eta\epsilon}{(1-\eta^2)^2}\left(\frac{z_0}{\sqrt{B_0^2 + B_q'^2 z_0^2}}\right) \qquad (3.18)\\
&\simeq \frac{B_0}{\sqrt{1-\eta^2}}\\
z_0 &\equiv \frac{B_0}{B'_q}\frac{\eta}{\sqrt{1-\eta^2}}
\end{aligned}$$

where z_0 is the lowest order term in the vertical position from Eq. 3.17. This is independent of the rotating field frequency since its effect is to apply an offset in the vertical field which only moves the equilibrium position, but does not change the field the atoms experience. To calculate the transition frequency between

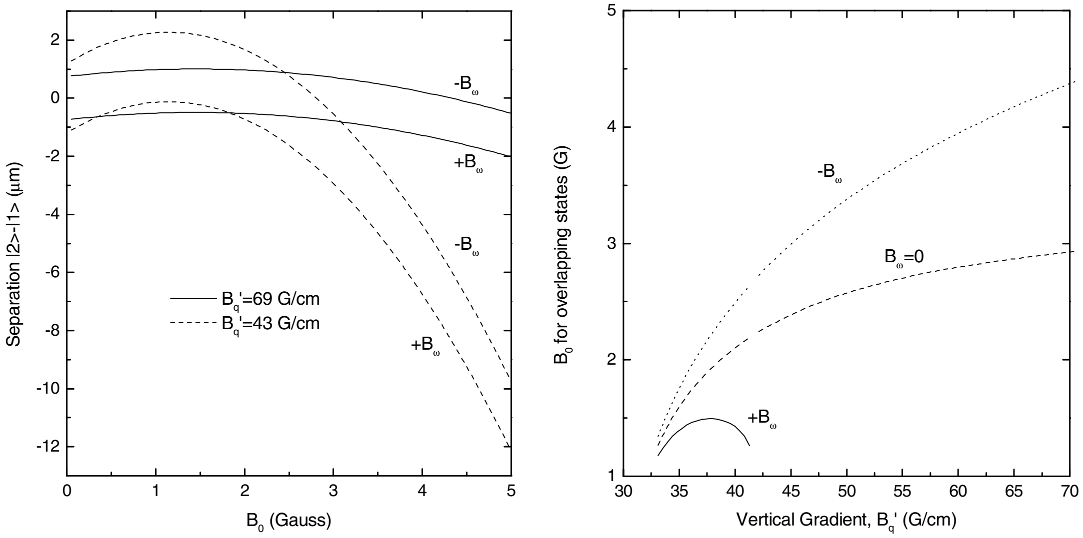

Figure 3.9: (a) The relative positions of the two states in the trap for two different values of the vertical gradient, with $\omega_t = 1800$ kHz. In each pair of lines are the plots for different rotation directions of the TOP field. As $B_0 \rightarrow 0$ the lines for a particular gradient are separated by $2B_w/B'_q = 2z_0$. (b) The magnitude of B_0 necessary to have overlapping condensates as a function of B'_q, for the different rotation directions and without including the rotating effect.

$|1,-1\rangle$ and $|2,1\rangle$, Eq. 3.18 must be used to calculate the field seen by each state. Since the atoms will be at the equilibrium position of the initial state ($|1,-1\rangle$ for instance), Eq. 3.18 is used with the appropriate η, z_0 and ϵ for $|1,-1\rangle$. The field B_2 experienced by $|2,1\rangle$ is not only different through the terms η, z_0 and ϵ, but also because it is offset from its equilibrium position by an amount $2B_\omega/B_q'$, which must be added to z_0 in Eq. 3.18. The transition frequency of Eq. 3.5, minus the hyperfine splitting ν_{hs}, becomes

$$\Delta\nu = -g_I\frac{\mu_n}{h}(B_1+B_2)+\frac{\mu_b}{4h}(g_J+\frac{g_I}{M_r})(B_2-B_1)+\frac{3}{16\nu_{hs}}\left((g_J+\frac{g_I}{M_r})\frac{\mu_b}{h}\right)^2(B_1^2+B_2^2) \tag{3.19}$$

This is plotted in Fig. 3.10 as a function of the rotating field B_0 for two different values of B_q'. The effect of changing the direction of the rotating field is to offset the transition frequency. For many experiments we wish to operate in the region where the transition is insensitive to field noise (or rotating field asymmetries). This is the zero-slope point in Fig. 3.10, where the total field experienced by the atoms is 3.241 G. The rotating field magnitude required to reach this point is given by the approximation

$$\begin{aligned} B_0 &= \sqrt{1-\eta^2(B_q')}\left(\eta B_\omega + 3.241\left(1-\frac{1}{2}(1-\eta^2)\frac{B_\omega^2}{3.241^2}\right)\right) \\ &\simeq 3.241\sqrt{1-\eta^2(B_q')}. \end{aligned} \tag{3.20}$$

The second approximation is very good; it is nearly independent of B_ω (off by 10 mG for a factor of 10 change in the rotation frequency).

Unfortunately, the requirements for overlapping condensates is not the same as the requirement in Eq. 3.20. A contour plot of the slope of the transition ($\partial\Delta\nu/\partial B_0$) is shown in Fig. 3.11 along with the trajectory for overlapping condensates from Fig.3.9b.

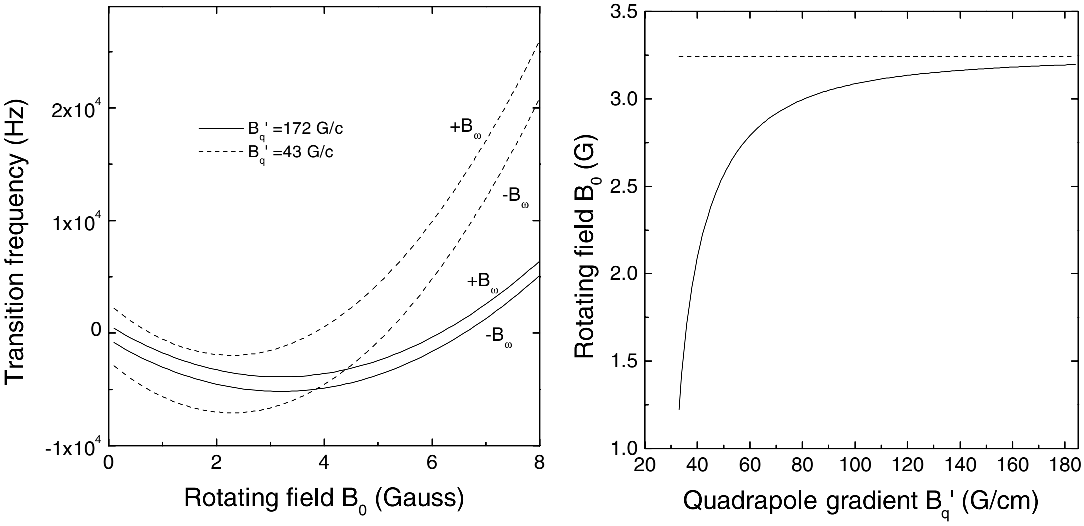

Figure 3.10: (a) The transition frequency as a function of the rotating field B_0, similar to Fig. 3.2(b), but here the complete, time-dependent model is included. Each pair is for a different vertical gradient. Within each pair the effect of the rotating field is shown for the two directions of rotation $\pm B_\omega$. (b) The value of B_0 where the transition is insensitive to changes in field, plotted against B_q'. The dashed line is 3.241 G.

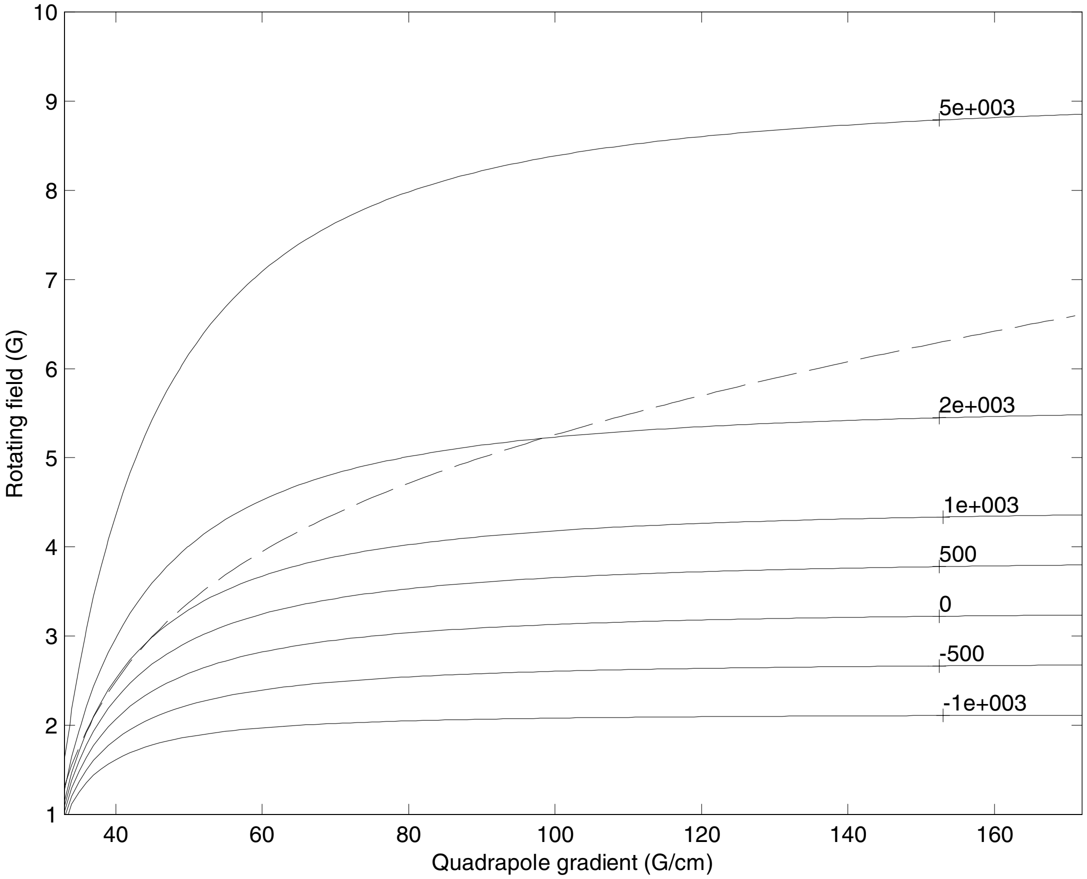

Figure 3.11: The contour plot shows the slope of the two-photon transition with respect to B_0. Lines are labeled in Hz. The dotted line is the B_0 required for completely overlapping traps, for the frequency of field rotation of 1800 Hz.

3.4 Rabi frequency gradient across the condensate

The previous section dealt with the basic effects of the TOP trap and the higher order Zeeman structure on the two-photon transition. This section will specialize to a remarkably useful consequence of these effects; a gradient in the two-photon effective Rabi frequency Ω_{eff} across the condensate. As will be shown in Chapter 7, the gradient provides a way to manipulate the phase of a condensate spatially and temporally. There are essentially three different (although not independent) effects: trap offset, intermediate state detuning, and polarization of the two-photon drive.

3.4.1 Trap offset

The vertical offset between the equilibrium positions of the two states was given in Eq. 3.17 and Fig.3.9. This comes into Ω_{eff} through the detuning of the two-photon drive from resonance:

$$\Omega_{\text{eff}} = \sqrt{\Omega_0^2(z) + \Delta^2(z)} \tag{3.21}$$

where Ω_0, the bare Rabi frequency from Eq. 3.1 and has no z dependence in this case, and

$$\begin{aligned} \Delta(z) &= \delta + \frac{1}{2}\frac{m}{h}\omega^2 z^2 - \frac{1}{2}\frac{m}{h}\omega^2 (z + z_{\text{offset}})^2 \\ &\rightarrow \delta + \frac{m}{h}\omega^2 z_{\text{offset}} z. \end{aligned} \tag{3.22}$$

This equation for $\Delta(z)$ includes an overall detuning δ (a simple detuning of the drive from the resonance) and the detuning due to offset harmonic oscillator potentials. For strong field gradients the offset is simply $2B_\omega/B'_q$. The trap oscillation frequency ω is nearly the same for both states. In the limit that $\Omega_0 \ll \Delta(z)$ or $\delta \gg$ the detuning across the condensate, the effective Rabi frequency becomes simply $\Delta(z)$ and there is a linear gradient in Ω_{eff} along the vertical dimension.

This gradient can be from 0 (overlapping traps) to a few kHz over the extent of the condensate.

3.4.2 Intermediate-state detuning

The bare Rabi frequency Ω_0 from Eq. 3.1 may also be modified by changing the intermediate-state detuning Δ_{IM} as a function of vertical position (refer to Fig. 3.1). Since the $|2,0\rangle$ state has no magnetic field dependence, and the $|2,1\rangle$ and $|1,-1\rangle$ shift essentially together at $\sim \mu_b/(2h) \simeq 0.7$ MHz/G, the virtual intermediate-state will shift, locked with the $|2,1\rangle$ and $|1,-1\rangle$ at 0.7 MHz/G. The gradient B' in which the condensate sits is where gravity is canceled, *i.e.* $B'\mu_b/2 = mg$ (higher order Zeeman terms are ignored). B' is approximately 30.5 G/cm for both $|2,1\rangle$ and $|1,-1\rangle$. The total intermediate state detuning is then

$$\begin{aligned} \Delta_{IM} &= \Delta_{IM0} + \frac{\mu_b}{2h} B' z \\ &= \Delta_{IM0} + \frac{mg}{h} z \\ &= \Delta_{IM0} + 2140 z \frac{\text{kHz}}{\mu\text{m}} \end{aligned} \tag{3.23}$$

where $z = 0$ is at the equilibrium position of the condensate, and Δ_{IM0} is the detuning of the microwave and rf from the $|2,0\rangle$ where $z = 0$. The magnitude of this effect can be controlled by changing the size of the condensate (by changing ω), changing the relative strength of Ω_0 and the detuning, or by changing Δ_{IH}. The size of this effect is variable from a few Hz to kHz. A gradient in Ω_{eff} due to a gradient in Ω_0 is advantageous since the entire condensate is still in resonance, as opposed to a gradient in the detuning Δ in which the transfer between the two states also varies along z.

3.4.3 Drive polarization

The polarization of the two-photon drive can also be made to vary across the vertical direction. This occurs by changing the direction of an atom's quantization axis by varying the relative magnitude of the fields B_0 and B_q'. As the confining potential is lowered, the atoms sag further down due to gravity, experiencing a difference in the vertical magnetic field component. This alters the projection of the microwave and rf drives onto the quantization axis, changing the bare Rabi frequency for each drive in Eq. 3.1. Since the rf and microwave have the same polarization, this effect gets squared for the two-photon transition. Taking the first order term for the position of the atoms in the trap (Eq. 3.17), the bare Rabi frequency and its gradient for the full two-photon transition become respectively

$$\Omega_0 \rightarrow \Omega_0(1-\eta^2) \tag{3.24}$$

$$\frac{\partial \Omega_0}{\partial z} = -2\Omega_0 \frac{B_q'}{B_0}\eta(1-\eta^2)^{3/2}. \tag{3.25}$$

These are plotted in Fig. 3.12. Fig. 3.12a is a plot of the fractional change in Ω_0 at the center of the condensate as the quadrupole gradient is changed. It is interesting that this is independent of the rotating field B_0. Fig. 3.12b is a plot of the fractional gradient in Ω_0. In Fig. 3.12c, this gradient is multiplied by the Thomas-Fermi vertical width (full-width at zero) [53] of the condensate to show the fraction change in Ω_0 across the condensate. In general this effect accounts for only a few Hz across the cloud, but could be made ~ 100 Hz.

The previous analysis assumed that the polarization of the microwave and rf were along the rotating field's axis. This is nominally true, but interaction with the conducting coil forms and supports likely modifies these fields in an unknown way. As an estimate, I assume the field polarization angle to maximize the gradient of polarization across the cloud, which gives an increase by a factor of 2.4. This is the maximum increase, and only applies for a specific B_q' in Fig. 3.12, which depends on the real angle of field polarization. For the case of the Rabi frequency gradient in Chapter 7, this maximum corresponds to ∼ 18 Hz across the condensate.

3.5 Density shift

This shift is not a property of the magnetic trap as all the previous effects have been, but still provides a systematic in the two-photon transition frequency. Repulsive interactions between ^{87}Rb atoms in a BEC lead to an energy offset from the ground state of the harmonic oscillator. Since the strength of the interactions is different for different internal states, there can be a systematic shift in the transition frequency between the states which will depend on relative state populations. This is a small effect by the standards here, but well known in atomic clocks as the clock-shift, or pressure shift [98]. The difference in interaction energy between the states is [53]

$$E = 5\pi\frac{\hbar^2}{m}\left[\left(a_{11}\langle n_1\rangle - a_{22}\langle n_2\rangle\right) + a_{12}\left(\langle n_2\rangle - \langle n_1\rangle\right)\right]. \tag{3.26}$$

where $\langle n\rangle$ is the density-weighted average density in the Thomas-Fermi limit, and a_{ij} is the s-wave scattering length between states i and j. The first group of terms comes from the self-interaction energy and the second group from the mutual interaction between the two states. We are concerned with only the following values; $a_{11} = 107$, $a_{22} = 101$, and $a_{12} = 104$ in units of the Bohr radius $a_0 = 0.529 \times 10^{-8} cm$ [46]. In a usual Ramsey-type clock, the two states involved have equal superpositions during the time between the $\pi/2$-pulses. For typical condensate densities of $5 \times 10^{13}\text{cm}^{-3}$, the shift is 30 Hz.

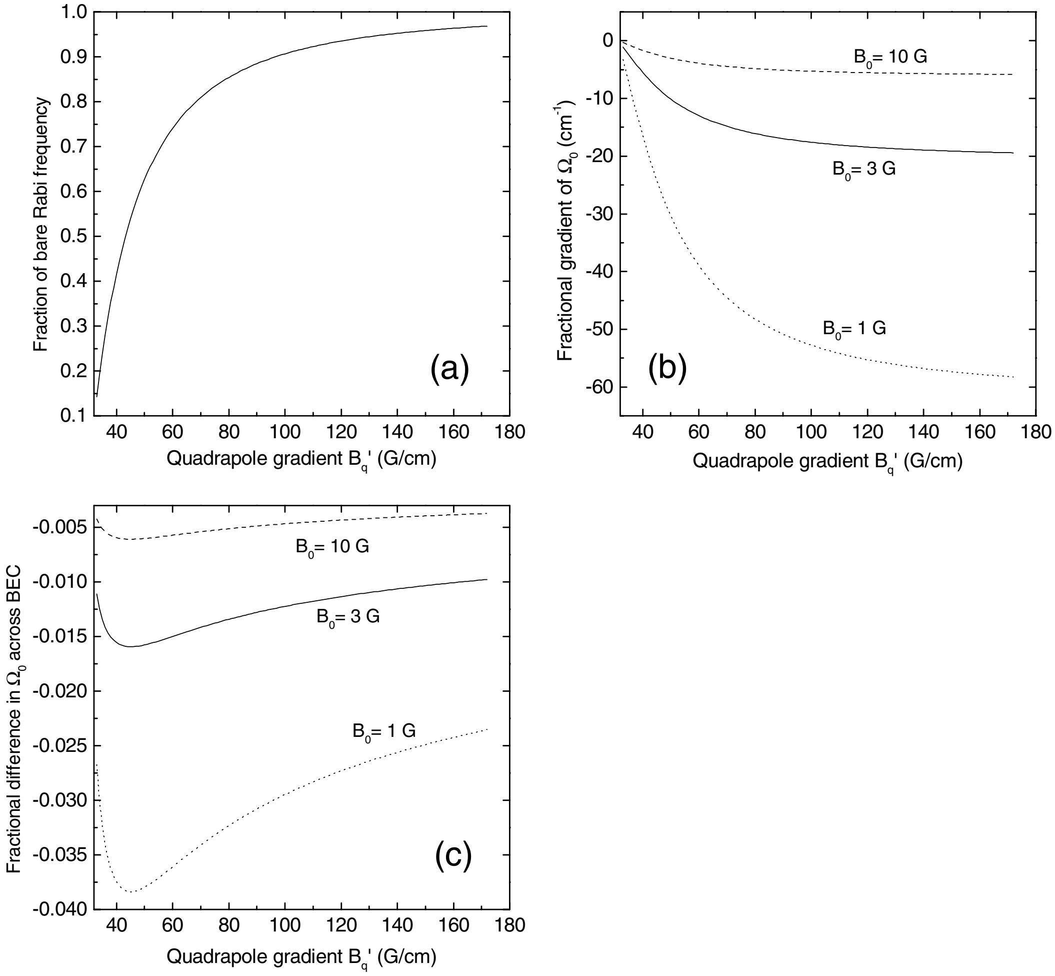

Figure 3.12: (a) The fractional change in bare Rabi frequency as a function of B'_q, due to a spatial gradient in polarization direction of the microwave and rf. (b) The fractional gradient in Ω_0 for three different values of the rotating field B_0. (c) The fractional difference in bare Rabi frequency across the cloud due to a gradient in the two-photon drive polarization. Multiply this by Ω_0 to get the absolute difference in bare Rabi frequency across the condensate's diameter.

3.6 Tilted TOP

One last effect is introduced as a possible explanation for two effects common in two-state experiments; sidebands and radial symmetry breaking. A systematic study of sidebands on the transition profile has not been done, and the only real knowledge we have is that they are separated from the central carrier by the TOP rotation frequency ω_t. Radial symmetry breaking is observed as a separation of two-component condensates in a specific direction perpendicular to the trap's symmetry axis (see Fig. 3.8) as will be discussed later. A possible explanation is a tilt of the axis of $\vec{\omega_t}$ in Fig. 3.8 relative to the axis of the quadrupole coils. The resulting field from a tilt by angle θ in the $\hat{x}$ direction is

$$\begin{aligned} |B_{\text{total}}(z)| &= \Bigg[\left(B_0\cos\theta\cos(\omega_t t) + \frac{B_q'}{2}x \pm B_\omega \sin\theta\right)^2 + \left(B_0\sin(\omega_t) + \frac{B_q'}{2}y\right)^2 \\ &+ \left(-B_q' z \pm B_\omega\cos\theta + B_0\cos\theta\cos(\omega_t t)\right)^2\Bigg]^{\frac{1}{2}}. \qquad (3.27) \end{aligned}$$

Two effects are present here. First, since the condensate experiences a field component in the $\hat{z}$ direction due to gravitational sag, the magnitude of the $\hat{z}$-component oscillates at the TOP frequency ω_t (third term). It causes a modulation of the transition frequency and thus sidebands. This can be thought of as a modulated drive; $\omega(t) = \omega_c + \Delta\omega\cos\omega_m t$ where ω_c and ω_m are the carrier and modulation frequencies, and $\Delta\omega$ is the amount of frequency modulation. To estimate the size of this effect, I start by estimating the on resonance Rabi frequency of the sideband Ω_{sb}, as ~ 0.4 of the Rabi frequency of the carrier Ω_c (determined from fig. 3.5). In the region of wide-band phase modulation the electric field can be written as

$$E(t) = A_c J_0(\beta)\cos\omega_c t - A_c J_1(\beta)(\cos(\omega_c+\omega_m)t - \cos(\omega_c-\omega_m)t) + ... \qquad (3.28)$$

where A_c is the amplitude of the carrier for zero modulation, J_0 and J_1 are Bessel functions, and $\beta \equiv \Delta\omega/\omega_m$ is the modulation index. The ratio of Rabi frequencies is then just that of the amplitudes squared $(J_1(\beta)/J_0(\beta))^2$ which implies $\beta \simeq 1$.

It is now necessary to estimate how big the TOP tilt must be to produce this size of modulation of the two-photon transition. To produce a modulation index of 1, $\Delta\omega \simeq \omega_t = 1800$ kHz. This amount of modulation gives an amount of magnetic field modulation through the derivative of Eq. 3.5, which is 100 Hz/G for $B_{\text{total}} = 3.5$ G. I take instead the very conservative limit of 500 Hz/G, implying a field modulation of 3.6 G which is larger than the total field. Obviously this cannot be the cause of the sidebands.

For completeness, I estimate the effect of a more reasonable tilt. The peak to peak amplitude of oscillation of the total magnetic field for small tilts θ, from Eq. 3.27 is

$$\Delta B_{pp} \simeq 2\eta(B'_q)B_0\theta. \tag{3.29}$$

A tilt of 5^o gives $\Delta B \simeq 0.3$ G out of $\simeq 3.5$ G total field. The slope is again taken to be 500 Hz/G (five times larger than the actual slope at $B_{\text{total}} = 3.5$ G) which means a frequency modulation of $\Delta\omega = 150$ Hz and a modulation index $\beta = \Delta\omega/\omega_{\text{top}} = 150/1800$.

Unfortunately a detailed study of sidebands has not been done, even though they are frequently an annoying presence. There are many features which have yet to be explained: Sidebands are present even for a dropped atom cloud ($B'_q = 0$, $B_\omega \neq 0$), implying the trap is not the cause (although an external field could take the place of the vertical field from the quadrupole); sidebands move and even switch sides about the carrier for different turn on times of the two-photon drive with respect to the rotating TOP field. This was true even when the two-photon pulse length is comparable to the TOP rotation period (It should be stressed that this latter observation was made with a different placement of the microwave waveguide, and has not been investigated for the current placement shown in Fig.

3.3).

A second effect of the tilt is a component of the imaginary field B_ω along the $\hat{x}$ direction (first term), thereby giving an offset similar to that discussed previously in the $\hat{z}$ direction. In this case however, gravity is perpendicular to the offset and so the higher-order Zeeman shifts cannot be used to cancel the offset as in Fig. 3.9. The magnitude of the offset is $4B_\omega \sin\theta/B'_q$. For θ =5 degrees, a vertical gradient of B'_q = 122 G/cm (17 Hz radial frequency), and a TOP rotation of 1800 kHz, this comes out to $\sim$ 0.08μm . See Fig. 5.4 for the data corresponding to this trap, showing the radial offset. To put this offset in perspective, it is compared with the vertical separation in a trap with vertical gradient of 129 G/cm, vertical frequency of 62 Hz, and an offset of 0.4 μm, seen in Fig. 5.5. In that case the time for appreciable separation was 10 ms. In the case of radial separation in Fig. 5.4 the radial separation time was about 100 ms. A rough scaling of the separation time in each case by the offset and the relevant trap frequency gives $(17 \times .08 \times 100) = 136$ and $(62 \times .4 \times 10) = 248$ shows a factor of two difference for a 5 degree tilt. A 10 degree tilt is somewhat unlikely, but the estimate shows the effect is in the right neighborhood.

Chapter 4

Imaging

4.1 Near resonance - absorption imaging

For a majority of the experiments described in this thesis, absorption imaging has been employed. This has been covered in detail in Ensher's thesis [61], but a few additional aspects are addressed here. Essentially, absorption imaging relies on the resonant scattering of light out of a probe beam, and the decrease in probe beam intensity is measured. Intensity decays exponentially through the condensate; $I_m = I_0 e^{-OD}$. The optical depth represents the column density of atoms along the probe direction; $OD(\vec{r}) = \int n(\vec{r}, \vec{z})\sigma_0 d\vec{z}$ for the scattering cross-section σ_0. It is extracted by imaging the spatially dependent probe intensity onto a CCD through the following three pictures; I_{shadow} – the intensity profile with the condensate present, I_{light} – the intensity profile of the probe beam only, and I_{dark} – an image with the probe beam off, so that only external sources of offsets are measured (for example, dark current on the CCD, or room lights). The measured optical depth is then calculated through

$$OD_{\text{meas}}(\vec{r}) = \ln\left(\frac{I_{\text{light}}(\vec{r}) - I_{\text{dark}}(\vec{r})}{I_{\text{shadow}}(\vec{r}) - I_{\text{dark}}(\vec{r})}\right). \tag{4.1}$$

This equation is applied for each pixel on the CCD array. For probe intensities comparable to the saturation intensity (1.6 mW/cm^2), the absorption no longer follows this equation, and Ensher [61] has derived a correction to obtain the real optical depth from the measured $OD_{\text{meas}}(\vec{r})$ and the probe intensity.

There are two more effects worth mentioning. The first has to do with a general correction which can be applied to account for many effects. Since the previous formulae rely on the assumption that all of the probe light interacts with the atoms the same way, the presence of off-resonant or incorrectly polarized light will lead to systematic effects. Since the probe laser linewidth is much less than the atomic linewidth, the light can be broken up into two pieces; on-resonant and correctly polarized light, off-resonant, incorrectly polarized, or scattered light. The first piece is the probe light which provides a signal proportional to the column density through the condensate. The remaining pieces are part of the probe beam but cannot be absorbed by the atoms. These can be lumped together into α, the fraction of the intensity which is not absorbed, and treated the same way as the other offsets I_{dark} . The measured optical depth using Eq. 4.1 becomes

$$OD_{\text{meas}}(\vec{r}) = \ln\left(\frac{I_{\text{light}}(\vec{r}) - I_{\text{dark}}(\vec{r})}{I_{\text{shadow}}(\vec{r}) + \alpha I_{\text{light}}(\vec{r}) - I_{\text{dark}}(\vec{r})}\right). \tag{4.2}$$

It is not practical to directly measure $\alpha I_{\text{light}}(\vec{r})$ simply through another image on the CCD, so its value must be found through other means. Once it is measured, the following rearrangement of Eq. 4.2 may be applied on a pixel by pixel basis to get the actual optical depth:

$$OD_{\text{real}}(\vec{r}) = OD_{\text{meas}}(\vec{r}) - \ln\left(1 - \alpha(\vec{r})e^{OD_{\text{meas}}(\vec{r})}\right) + \ln(1 - \alpha(\vec{r})). \tag{4.3}$$

This is plotted in Fig. 4.1 for three values of α.

An example of the above correction is the "polarization correction", which accounts for the variation in the direction of the atoms' quantization axis as the TOP field rotates during the probing. Ideally, the probing would only occur while the TOP field points along (or toward) the circularly polarized probe beam so that the cycling transition $F = 2, m_F = 2 \rightarrow F' = 3, m_F = 3$ is driven. Since the

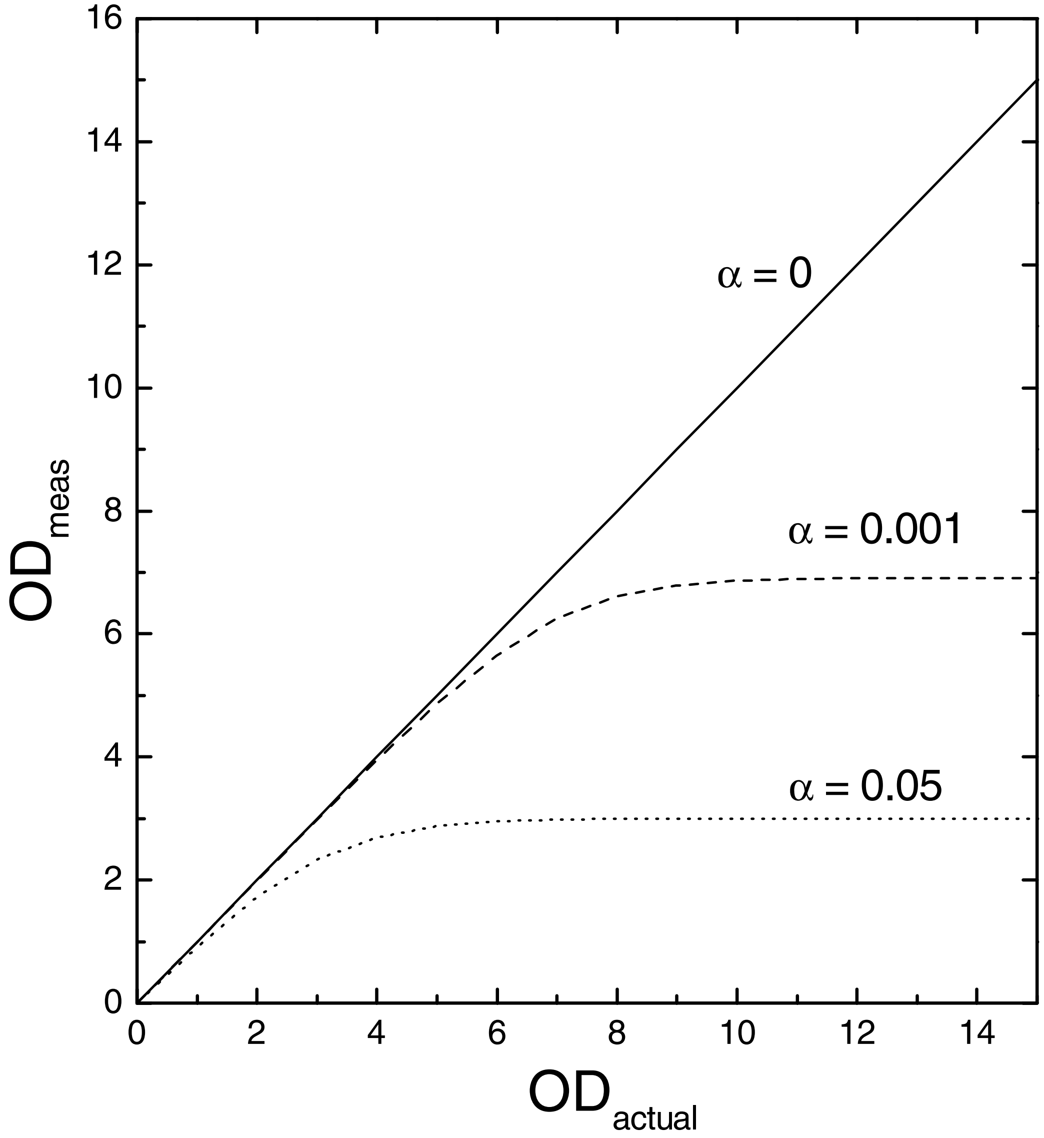

Figure 4.1: For a real optical depth of OD_{actual} the observed value (OD_{meas}) is plotted for different values of the fraction of light which cannot absorbed by the atoms α.

probe has finite duration t_{p}, the field rotating at angular frequency ω_t sweeps out an angle $\theta = t_{\mathrm{p}}\omega_t$. This can either be thought of as a time-varying polarization applied to the $m_F = 2$ state, or as a constant circular polarization applied to a time-varying state superposition. In the second picture the population in the $m_F = 2$ state varies as $\cos^4(\theta/2)$. Integrating this from $-\theta/2 \rightarrow \theta/2$ (assumes that the TOP field points along the probe beam half-way through the probe pulse) gives the fraction of correctly polarized light ($i.e. = 1 - \alpha$) :

$$\begin{aligned} f &= \frac{3}{8} + \frac{1}{\theta}\cos^3\left(\frac{\theta}{4}\right)\sin\left(\frac{\theta}{4}\right) + \frac{3}{2\theta}\cos\left(\frac{\theta}{4}\right) \\ &\simeq 1 - \frac{1}{24}\theta^2 + \frac{1}{768}\theta^4 \end{aligned} \tag{4.4}$$

for small θ. The resulting incorrectly polarized fraction can be substituted into Eq. 4.3 for alpha. In early experiments where $\omega_t = 2\pi \times 7200$ Hz and $t_{\mathrm{p}} = 25.7\mu$s, this accounted for a 10% decrease in observed optical depth for a condensate with real optical depth of 1. This does not take into account other possible transitions.

4.1.1 Lensing

Part of the simple model of absorption imaging is that the light traveling through the condensate is only attenuated by resonant scattering. For sufficiently dense atom clouds, there can also be a large spatial change in the index of refraction. The rays traveling through the cloud will suffer some refraction due to the curvature of the condensate, as well as its density profile. In this way it behaves as both a geometric lens and a gradient-index (GRIN) lens. The type of lens (converging or diverging) depends on the detuning of the probe from resonance as the index is greater or less than one respectively. This behavior can lead to systematics in measurements of the temperature and density. The focal length of a ball of radius R with uniform density is given by

$$f = \frac{R}{2(n-1)} \tag{4.5}$$

where n is the index of refraction (see Eq. 4.10). Lensing is a problem when the focal length is shorter than the focal depth of the imaging system, or when the imaging system is improperly focused. For our imaging setup with an f-number of ~ 5, the focal depth is 200 μm. A condensate of 20 μm radius implies that $(n-1) \ll .05$ for minimal lensing, which occurs for a probe detuning $\Delta > 600$ MHz. At this detuning the observed optical depth is down to 0.05, which is visible but with signal to noise near unity.

A schematic of lensing is shown in Fig. 4.2. The condensate is represented by the dark grey ball and the probe beam is incident from the left. For the blue detuned case, the index is less than 1 so the condensate is a diverging lens. The solid lines represent the path of the probe light and the dashed lines show the boundary outside which the light does not travel through the condensate. At position B, light from the inside of the condensate is refracted outside the cylinder defined by the dashed boundary. Where this occurs (represented by the light grey areas) there is more light than the non-refracting model would suggest. If the focal plane of the imaging system were at B, the resulting optical depth would look basically normal near the center of the condensate (except for an enhanced OD), but would actually go negative at the edges due to the increase in light in the presence of a condensate. If the focal plane where at position A, then the virtual image must be taken into account, represented by the dotted lines. Here there is a cone of excess light, and the resulting optical depth has a corresponding negative dip in the center. Similar but reversed pictures occur in the case of red detuning.

Lensing is a serious complication when probing a condensate in the magnetic

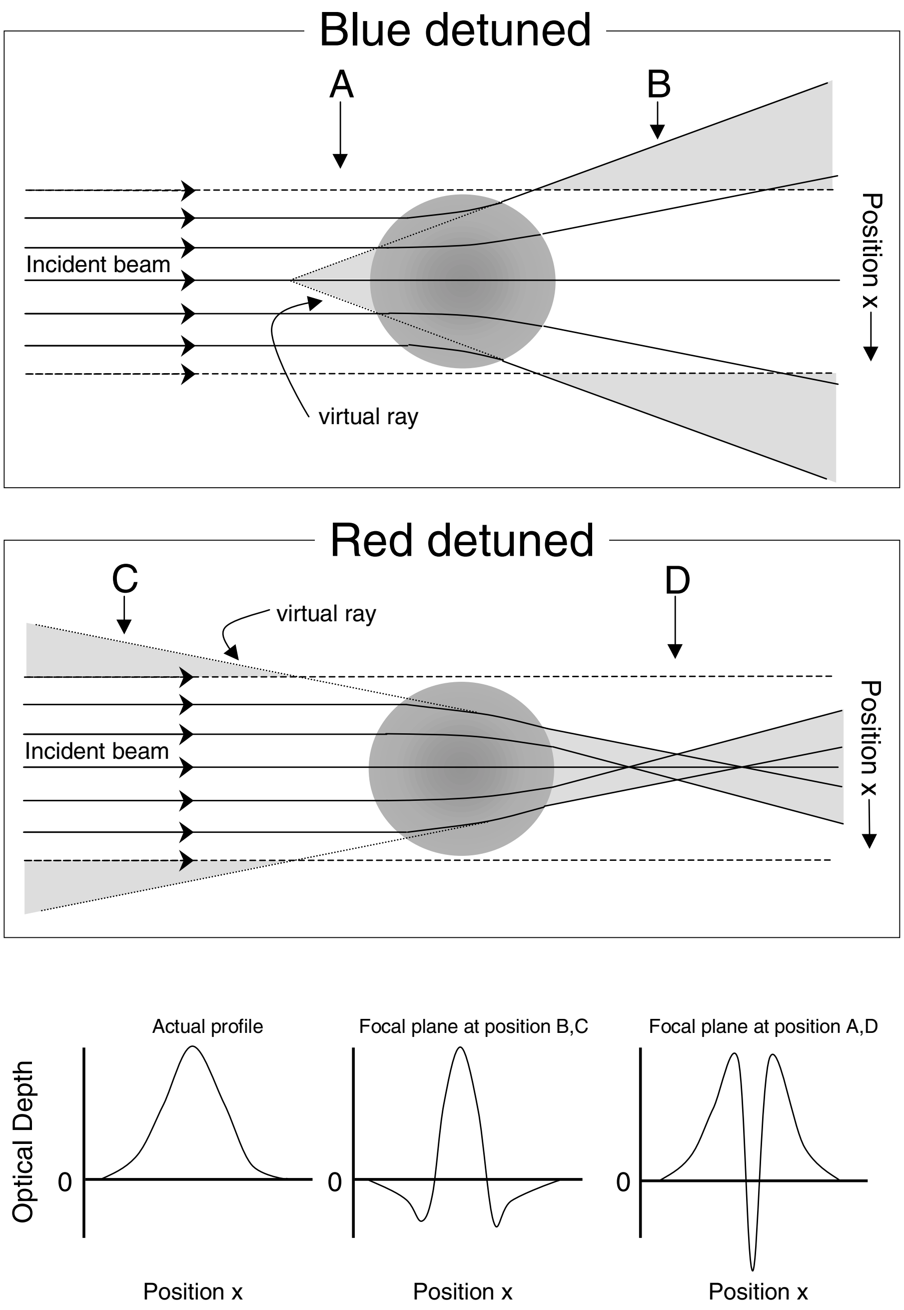

Figure 4.2: Schematic of a uniform ball with index $\neq 1$ in the path of a probe beam incident from the left. Grey regions enclosed by beam paths indicate an increase in the light level over the non-refracting model. Regions outside the dashed lines (a cylinder around the condensate) are where the probe light does not intercept the condensate. Dotted lines represent virtual rays. At the bottom are the actual image in the absence of lensing, and the observed optical depth is shown for various focal plane locations.

trap. On resonance, the index is 1 so lensing is not a problem. However the optical depth is much too large (> 100), so that small contributions to α in Eq. 4.3 can severely effect the optical depth, leading to a saturation. In fact, from Eq. 4.3 the maximum observable optical depth is

$$OD_{\text{max}} = \ln\left(\frac{1}{\alpha}\right) \tag{4.6}$$

which turns out to be ~ 3 for our experiment, implying $\alpha = .05$. Detuning further from resonance does make lensing better, but the index of refraction only drops off as $1/\Delta$ and the signal drops as $1/\Delta^2$ so the "signal-to-lensing" ratio gets worse. For this reason destructive imaging is most useful when looking at dropped, expanded condensates when the density is low and the radius of curvature big.

4.1.2 Signal-to-noise

The signal-to-noise is given in terms of the real optical depth by;

$$S/N = \frac{OD_{\Delta}(1-\alpha)\exp^{-OD_{\Delta}}}{\sqrt{\sigma_S^2 + \sigma_L^2}\,((1-\alpha)\exp(-OD_{\Delta}) + \alpha)} \tag{4.7}$$

where $OD_{\Delta} = OD_{\text{res}}/\left(1 + 4(\Delta/\gamma)^2\right)$ for the on-resonance, real optical depth OD_{res}, Δ is the detuning from resonance, γ is the natural linewidth of ^{87}Rb (5.9 MHz), and σ_L and σ_S is the fractional intensity noise in the light and shadow frames respectively. Noise on the dark frame is ignored in this analysis. This is justified since dark noise is about 1 count versus 7 counts of noise from the other sources listed here (dark noise can vary from chip to chip even for the same type, depending on CCD quality, the quality of the vacuum, and the temperature of the CCD). In the case of shot noise, $\sigma_S = 1/\sqrt{(1-\alpha)I_0\exp(-OD_{\Delta}) + \alpha I_0}$ and $\sigma_L = 1/\sqrt{I_0}$ and the signal-to-noise becomes

$$S/N_{\text{shot}} = \frac{\sqrt{I_0}OD_{\Delta}(1-\alpha)\exp^{-OD_{\Delta}}}{\sqrt{(1-\alpha)\exp(-OD_{\Delta}) + \alpha + 1}\sqrt{(1-\alpha)\exp(-OD_{\Delta}) + \alpha}} \tag{4.8}$$

where I_0 represents the number of photons in the probe (actually, it must also include the quantum efficiency of the detector). Since the signal for near-resonance imaging is a reduction in light level, the S/N_{shot} actually gets worse for large signals. The optical depth with maximum S/N_{shot} is 2.2 when $\alpha = 0$, implying that the detuning Δ should be set to achieve that measured OD. Figure 4.3 shows the optimal optical depth for different values of α.

A major source of noise above shot noise for usual intensities is spatial fluctuations of the probe intensity between the shadow and light frames. This is due to small scale fringes on the probe beam that change position between the I_{shadow} and I_{light}. In this case the noise is linear in the light intensity, and σ is the standard deviation for a sinusoidal function with fractional amplitude A. The signal-to-noise is

$$S/N_{\text{fringe}} = \frac{\sqrt{2}}{A} \frac{OD_\Delta (1-\alpha) \exp^{-OD_\Delta}}{((1-\alpha)\exp(-OD_\Delta) + \alpha)} \tag{4.9}$$

assuming maximum variation in the fringe spacing. The optimal optical depth in this case is also plotted in Fig. 4.3. These are compared to other imaging techniques at the end of this chapter.

4.1.3 Magnification measurement

For many quantitative measurements knowing the imaging magnification is extremely important. If an atom cloud is to be used for measuring the magnification, then the camera must be set at the focal point of the imaging system. Ensher [61] described a method for doing this by destructively imaging small atom clouds in the magnetic trap. This technique was plagued by lensing effects and gave only modest results. Non-destructive imaging brought the ability to tolerate large optical depths so that very small clouds could be imaged in the trap. The position of the camera was then adjusted to give the smallest observed cloud

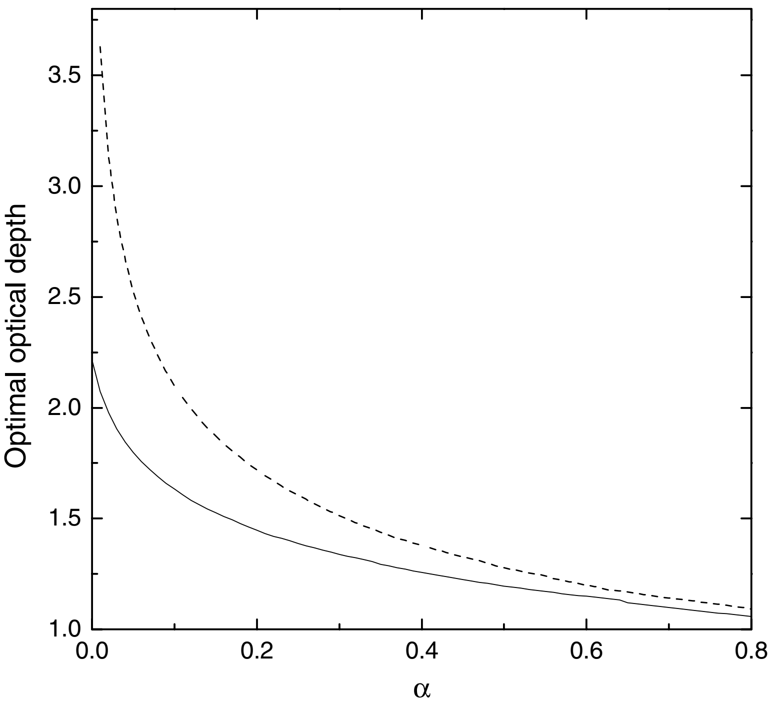

Figure 4.3: α is the fraction of the probe intensity which cannot be absorbed by the atoms. This plot shows the optical depth required for the best signal to noise for a given value of α in the shot noise limit (solid line) and for the intensity noise limit (dashed line).

diameter.

The first method used for a magnification measurement was to obtain a value for g by turning off the trap and watching the atom cloud fall. A new picture was taken for each different time after the trap was turned off. The resulting vertical position was fit to a gravitational acceleration with a size scaling, and an initial velocity. The size scaling directly gives the magnification.

A separate method for measuring the magnification was to use the interference of two beams which cross at the same location of the atom cloud, as illustrated in Fig. 4.4. Essentially, the input angle α was measured, and the fringe spacing from the interference on the CCD was measured to yield the angle β. The magnification is then the ratio α/β. It is crucial that the two beams cross at the location of the atom cloud. This was done by first centering the probe beam on the atoms. While looking at the CCD image, the split-off beam (dotted line) was overlapped with the probe beam on the CCD, guaranteeing that they crossed at the atom cloud since the imaging system was previously set at the focal point for the cloud. The current magnification from this method is 9.4, or 1 camera pixel = 2.5μm in the trap. This method and the dropping method yield very similar results, so one is not clearly better than the other. They are complimentary though since they rely on very different measurements. A possible systematic affecting the optical measurement is curvature in the glass windows that changes the angle between the two beams before the lens L1. This effect could be manifested in different ways between the optical method and dropping method, since they use different axes and regions of the window(s).

4.1.4 Double condensate imaging

Early double condensate experiments used destructive imaging of ballistically expanded condensates. Ensher [61] provides an explanation of the sequence

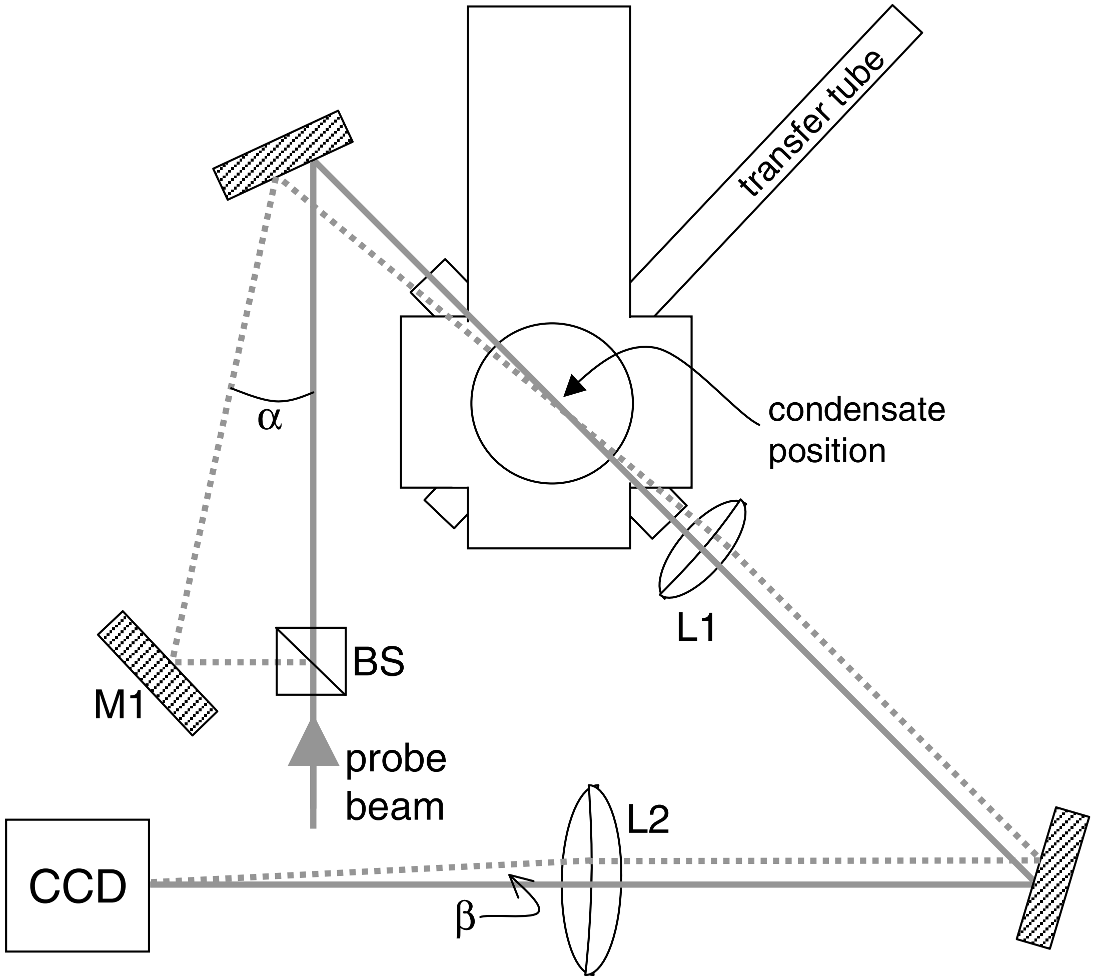

Figure 4.4: A schematic for measurement of the imaging system magnification using interference. The probe beam is split into two pieces which cross with angle α where the condensate would be. They overlap again on the CCD array, but at a different angle β, measured by observing the fringe spacing of the interference pattern on the CCD . The ratio of α/β determines the magnification.

of laser pulses necessary to see either of the $|1,-1\rangle$ or $|2,1\rangle$ states. However, to image $|1,-1\rangle$ in the presence of $|2,1\rangle$ it was necessary to "blow away" the $|2,1\rangle$ atoms with a ~ 2 ms pulse of MOT light about 10 ms before the $|1,-1\rangle$ atoms were imaged (the expansion time was typically 22 ms, so the MOT pulse occurred after ~ 12 ms of expansion). For significant attenuation (8×10^{-3}) of the MOT beams this was sufficient to not disturb the $|1,-1\rangle$ atoms.

In order to image both states in a single shot a similar technique was used. The $|2,1\rangle$ atoms were first imaged using a $F=2 \rightarrow F'=3$ probe pulse. About 1 ms later the attenuated MOT light was flashed on for 2.8 ms to discard the $|2,1\rangle$ atoms as described above. One millisecond after that, the $|1,-1\rangle$ atoms were imaged by applying a short repump pulse and then the probe pulse [61]. Since there is significant time between the imaging of the states, the $|1,-1\rangle$ condensate expands and drops further as seen in Fig. 4.5.

4.2 Polarization Imaging

Polarization imaging was used as a first attempt at non-destructive imaging of a condensate. When a condensate is in a single state, the Clebsh-Gordon coefficients K (Fig. 4.6 and Tab. 4.1) are in general different for left (σ_-) and right (σ_+) circularly polarized light. If the input probe beam is linearly polarized, then the output beam will have its polarization axis rotated slightly, since the σ^+ and σ^- components experience different phase shifts through the condensate. This is the same birefringent process exploited in polarization spectroscopy [55].

For light with frequency ω and detuning Δ from the atomic transition, the phase shift [10] through a media of length d is

$$\begin{aligned} \phi &= \frac{d\omega}{c} Re\,(n(\Delta)) \\ Re\,(n(\Delta)) &= 1 + \frac{Ne^2}{8\pi\epsilon_0 m\omega} \sum_i \frac{\Delta_i}{\Delta_i^2 + (\gamma/2)^2} K_i \end{aligned} \tag{4.10}$$

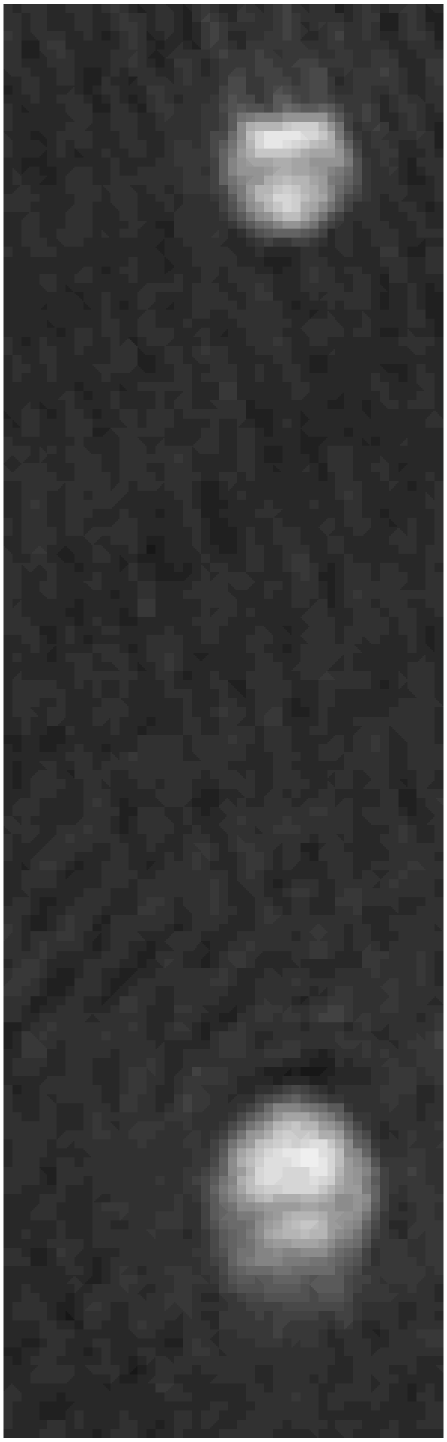

Figure 4.5: Image of both the $|2,1\rangle$ (top) and $|1,-1\rangle$ (bottom) condensates after dropped from the magnetic trap. In the trap the $|2,1\rangle$ sits below the $|1,-1\rangle$.

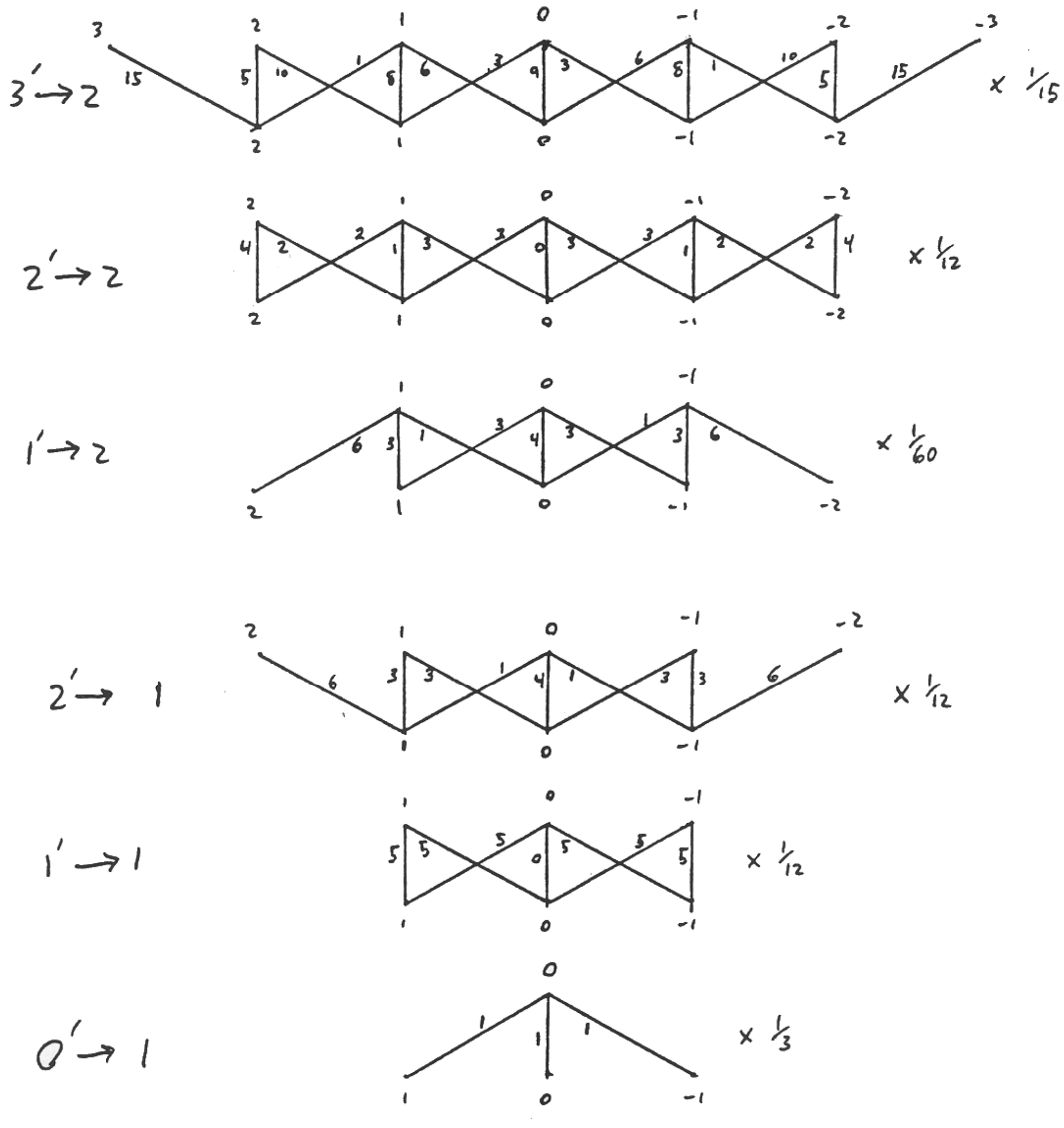

Figure 4.6: Branching ratios for ^{87}Rb .

state	σ_+	σ_-	π
$\|2,2\rangle$	1/2	1/6	1/3
$\|2,1\rangle$	5/12	1/4	1/3
$\|1,-1\rangle$	5/12	1/4	1/3

Table 4.1: The effective Clebsh-Gordon coefficients for light far detuned from the $5P_{3/2}$ states.

where Nd is the integrated through density, e and m are the charge and mass of the electron and the sum is over all possible transitions. It must also be true that the Clebsh-Gordon coefficients are normalized $\sum_i K_i = 1$. Specializing to only two levels (for σ^+ and σ^-) which are assumed to be at nearly the same detuning from the initial state (as compared to Δ), the difference in phase shift is

$$\delta\phi = \sigma_0 \frac{Nd}{8\pi}\gamma \frac{\Delta}{\Delta^2 + (\gamma/2)^2}(K^+ - K^-) \tag{4.11}$$

in which σ_0 is the on resonant cross-section for the atom to scatter a photon. Since the on-resonance optical depth is simply $\sigma_0 Nd$, this can be rewritten in order to compare with destructive imaging;

$$OD_{\text{res}} = \frac{8\pi}{(K^+ - K^-)}\frac{\Delta}{\gamma}\delta\phi \tag{4.12}$$

when $\Delta \gg \gamma$.

The setup to measure the rotation of polarization due to $\delta\phi$ is shown in Fig. 4.7. A Glan-laser input polarizer (P1) defines the polarization of the incoming probe beam. The condensate is imaged when the rotating magnetic field has the correct phase to point along the probe beam so that the linear polarization is composed of equal parts σ^+ and σ^-. A second Glan-laser polarizer (P2) at angle θ to the first allows a measurement of the amount of rotation of the polarization. For an input intensity (after the first polarizer) I_0 and a relative phase shift of $\delta\phi$, the polarization is rotated by $\delta\phi/2$. The intensity at the CCD is

$$I_m = I_0 \cos^2(\theta - \delta\phi/2)\,. \tag{4.13}$$

As in the destructive measurements, three images are taken in order to measure the beam intensity distribution and any offsets. The optical depth can be written in terms of the measured quantities and applied on a pixel by pixel basis (similar to Eq. 4.1):

$$OD_{\rm res} = \frac{16\pi}{(K^+ - K^-)}\frac{\Delta}{\gamma}\left(\cos^{-1}\sqrt{\frac{I_{\rm shadow} - I_{\rm dark}}{I_{\rm light} - I_{\rm dark}}} - \theta\right). \tag{4.14}$$

The quantity $\delta\phi/(\sigma_0 N d)$ from Eq. 4.12 (using the full sum Eq. 4.10) is plotted in figure 4.8 for the three trapped states of ^{87}Rb . In (c) data is shown for a non-condensed cloud of $|2,2\rangle$ atoms over regions of minimal scattering rate. For (c) the probe laser frequency was determined by measuring the beat frequency between it and the MOT laser with an avalanche photodiode.

This signal may be used for nondestructive measurements of double condensate systems. For large detunings ($\Delta \gg \gamma$) from both the $|2,1\rangle$ and $|1,-1\rangle$ states, the signal for atoms in either hyperfine state and the trappable m_F Zeeman state is

$$\delta\phi = \frac{OD_{\rm res}}{8\pi}\frac{\gamma}{\Delta}\frac{|m_F|}{6} \tag{4.15}$$

where the presence of $|m_F|$ is only a useful coincidence; it has no physical meaning. When the probe is tuned between the resonances for $|1,-1\rangle$ and $|2,1\rangle$, the signal is positive for $|2,1\rangle$ atoms and negative for $|1,-1\rangle$ atoms since the detuning Δ switches signs. This makes polarization imaging useful for double condensate measurements since the states are distinguishable. In this case the range of phase shift is the difference between all the atoms in $|1,-1\rangle$ and all the atoms in $|2,1\rangle$;

$$\delta\phi = \frac{OD_{\rm res}}{24\pi}\frac{\gamma}{\Delta}. \tag{4.16}$$

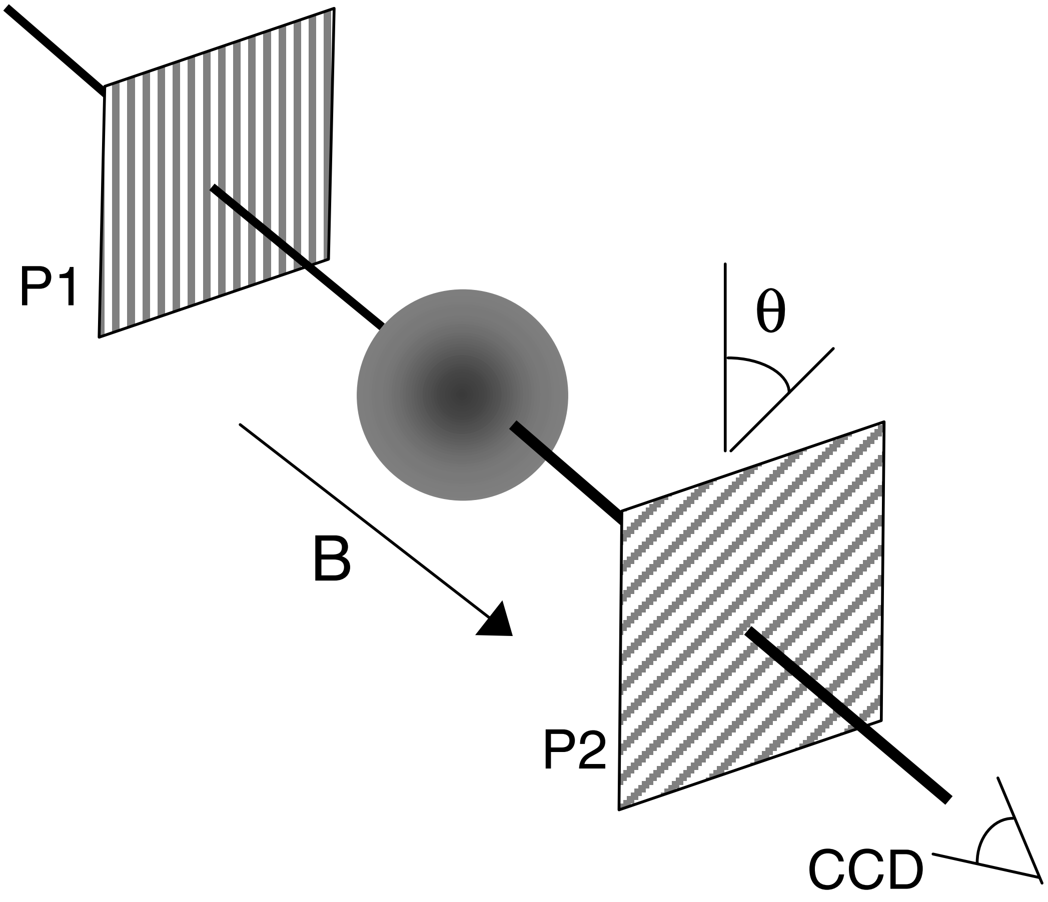

Figure 4.7: Schematic for polarization imaging. The probe beam incident from the upper-left travels through a polarizer (P1) to purify the polarization. It travels through the condensate whose birefringence rotates the polarization of the probe. The beam exits through the second polarizer (P2) which is at an angle θ to the first. The transmission through P2 depends on the amount of polarization rotation caused by the condensate which is proportional to the column density.

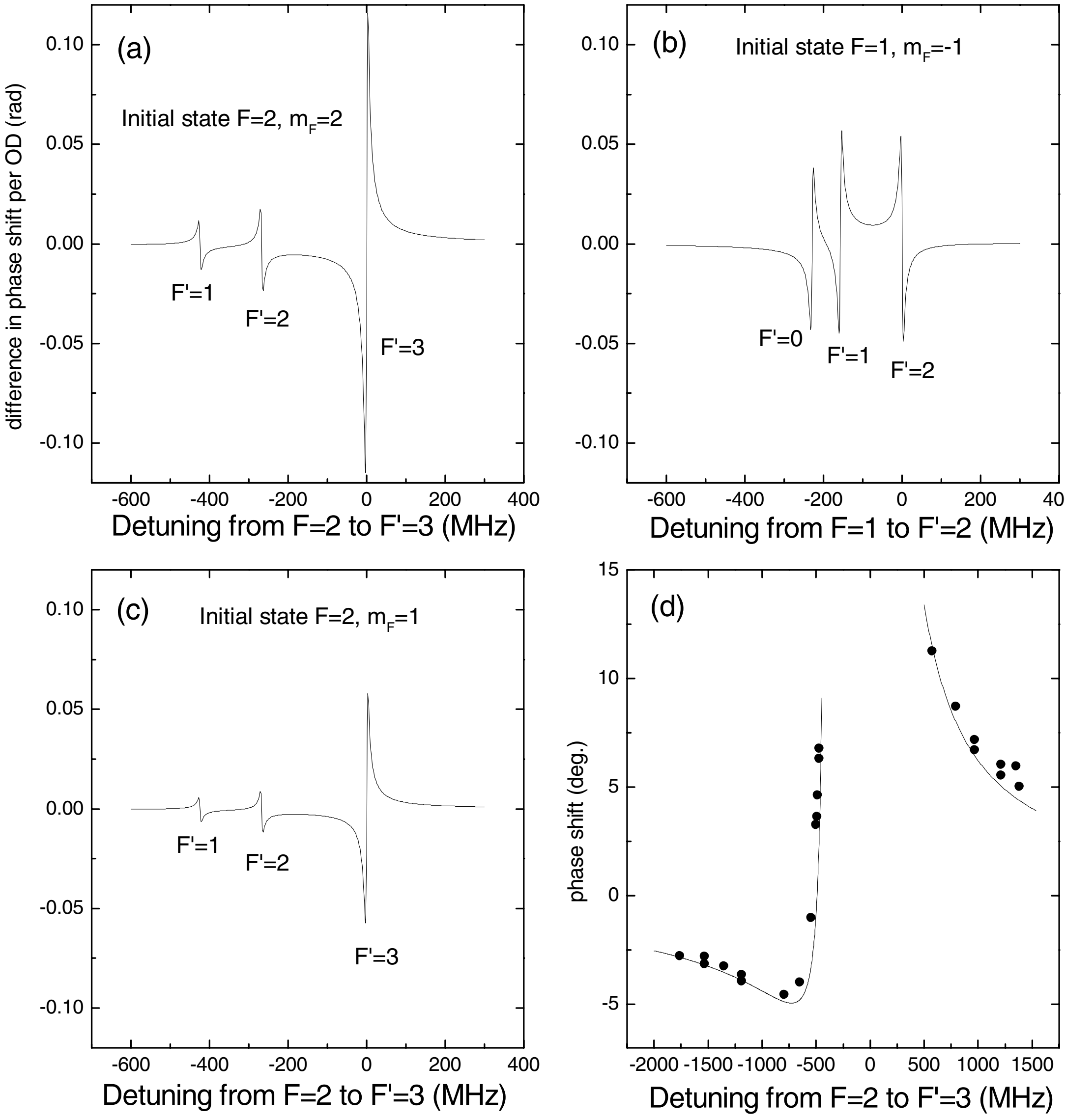

Figure 4.8: Plots of the signal from polarization imaging as a function of detuning. (a) For atoms in the $F = 2, m_F = +2$ state. (b) For atoms in the $F = 1, m_F = -1$ state. (c) For atoms in the $F = 2, m_F = +1$ state. (d) Rotation of the probe's polarization as a function of detuning for atoms in the $F = 2, m_F = +2$ state. The data points are for a cloud with optical depth ~ 70.

4.2.1 Signal-to-noise

The signal to noise for polarization imaging is

$$S/N = \delta\phi(\Delta, OD_{\text{res}}) \frac{\sin\left(\theta - \delta\phi(\Delta, OD_{\text{res}})/2\right)}{\cos\left(\theta - \delta\phi(\Delta, OD_{\text{res}})/2\right)} \frac{1}{\sqrt{\sigma_L^2 + \sigma_S^2}} \tag{4.17}$$

where $\delta\phi(\Delta, OD_{\text{res}})$ is given in Eq. 4.11. For the shot noise limit on the probe intensity, $\sigma_S^2 = 1/I_0 \cos^2(\theta - \delta\phi(\Delta, OD_{\text{res}}))$ and $\sigma_L^2 = 1/I_0 \cos^2\theta$ the signal to noise is

$$S/N_{\text{shot}} = \sqrt{I_0}\delta\phi(\Delta, OD_{\text{res}}) \frac{\sin(\theta - \delta\phi(\Delta, OD_{\text{res}})/2)\cos\theta}{\sqrt{\cos^2(\theta - \delta\phi(\Delta, OD_{\text{res}})) + \cos^2\theta}} \tag{4.18}$$

When the noise is dominated by fringes with fractional amplitude A on the probe intensity, the signal to noise is simply

$$S/N_{\text{fringe}} = \delta\phi(\Delta, OD_{\text{res}}) \frac{\sin(\theta - \delta\phi(\Delta, OD_{\text{res}})/2)}{\cos(\theta - \delta\phi(\Delta, OD_{\text{res}})/2)} \frac{\sqrt{2}}{A} \tag{4.19}$$

Both of these have a maximum near $\theta = \pi/2$ when the phase shift $\delta\phi$ is small. Data was taken looking at a condensate expanded 10 ms from a 80 Hz axial frequency trap. Figure 4.9 shows this and a fit of the shot noise limiting form of Eq. 4.18.

Birefringence of the vacuum windows contributes an offset which can add to the noise. The birefringence was measured by rotating the input polarization with a waveplate, and correspondingly rotating the input polarizer. The output polarizer was then rotated to find the extinction ratio. It was found that the best extinction ratio was for vertically polarized light, at which point the extinction was ~ 100 times worse than the polarizers themselves (Glan laser polarizers were measured to be 5×10^{-6}). The worst extinction was 2×10^{-2} for horizontal polarization.

Eqs. 4.18 and 4.19 indicate that the signal to noise can be shot noise limited at $\theta = \pi/2$. However the small amount of light which makes it though both

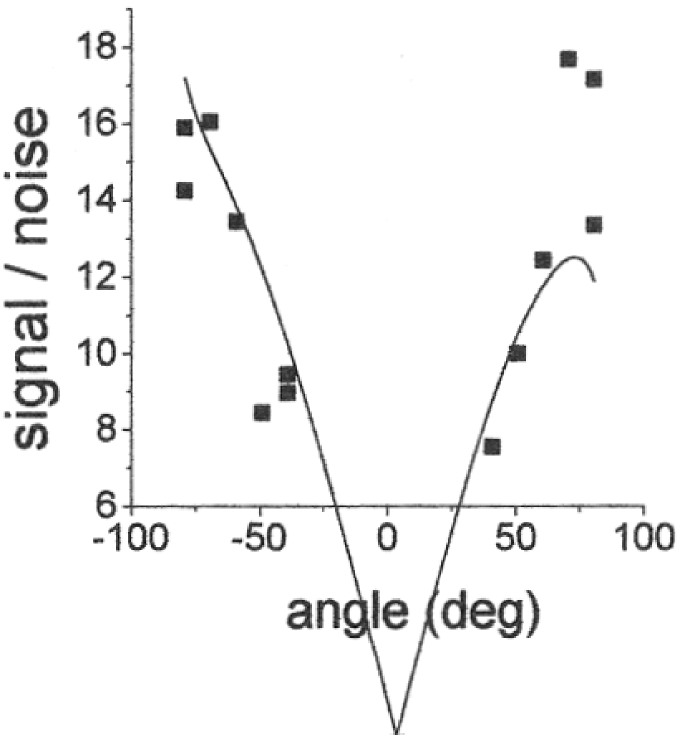

Figure 4.9: Plot of experimental signal to noise as a function of crossing angle θ between the two polarizers. For this data $\delta\phi = 3.6$ degrees. The solid line is a fit of the shot-noise limiting form.

polarizers (due to window birefringence and finite polarizer extinction) means that the minimum noise is the shot noise (or fractional noise) on this light. These comments are somewhat unnecessary though, since we must allow some light through in order to do a pixel by pixel calibration of the light intensity; the signal at each pixel is determined not only by the phase shift from the condensate, but also by spatial variations in probe intensity. These variations cannot be measured if $\theta = \pi/2$, without removing the second polarizer (which would no doubt result in a change in the spatial variations for a real-world polarizer). This is a general problem with dark-ground imaging schemes, even though they yield superior signal to noise in other applications (like polarization spectroscopy). It should be mentioned that schlieren [11] imaging does not suffer from this since high spatial frequency components do make it to the imaging plane.

4.3 Phase-contrast imaging

Phase-contrast imaging [12, 37] is another nondestructive technique currently in use. It relies on a comparison between the phase shifts of the light traveling through the condensate versus that which does not travel through. The effect may be derived using a straight forward argument (see Appendix A for a complete derivation).

At the plane perpendicular to the imaging axis, and just after the condensate, the electric field can be written as

$$E(x,t) = E_0 \cos(\omega t + \phi(x)) \tag{4.20}$$

where $\phi(x)$ is a spatially dependent phase shift on the probe light from its interaction with the condensate. Assuming the phase shift is small this is

$$E(x,t) = E_0(\cos(\omega t) + \phi(x) \sin(\omega t)). \tag{4.21}$$

For small phase shifts this of course does not yield a signal since the time average of $|E|^2$ does not depend on $\phi(x)$. We require an additional phase shift in only one of the terms in Eq. 4.21. If a $\pi/2$ shift is applied to only the second term, then the intensity is

$$I(x) = I_0(1 + 2\phi(x)) \tag{4.22}$$

which reproduces the same phase pattern as that produced by the condensate.

Since the intensity is linearly dependent on the phase shift, the signal reverses signs depending on which side of resonance the probe beam is located. For a mixture of condensates in the $|1,-1\rangle$ and $|2,1\rangle$ states, a beam tuned in the middle of the transitions gives a positive signal for $|1,-1\rangle$ atoms and a negative signal for $|2,1\rangle$ atoms. When the states are spatially overlapping, the signal is proportional to the population difference.

The implementation is shown in figure 4.10. Light which is not affected by the condensate (solid lines) is focused at P1 by the first imaging lens. The part of the light which is diffracted by the condensate (dashed lines) is collimated at P1 since the condensate is at the focal point of the first lens. These two components are the two terms in Eq. 4.21. Since they are spatially separated by the lens, a $\pi/2$ phase shift can be applied by inserting a window with a “phase dot” – a layer of MgF with the proper thickness. The diameter of the dot must be large compared to the waist size of the probe beam, but small compared to the diffracted beam. For our experiment with beam size $\sim$ 2 mm and condensate size $\sim 20\mu$m, the focused probe is 50 μm and the diffracted beam is 5000 μm, providing a large possible range for the phase dot size. We chose 100 μm diameter in order to be able to image non-condensed atom clouds (at least the colder ones) that are much larger in size than the condensate.

In general it is not trivial to align the phase dot with the probe beam. The

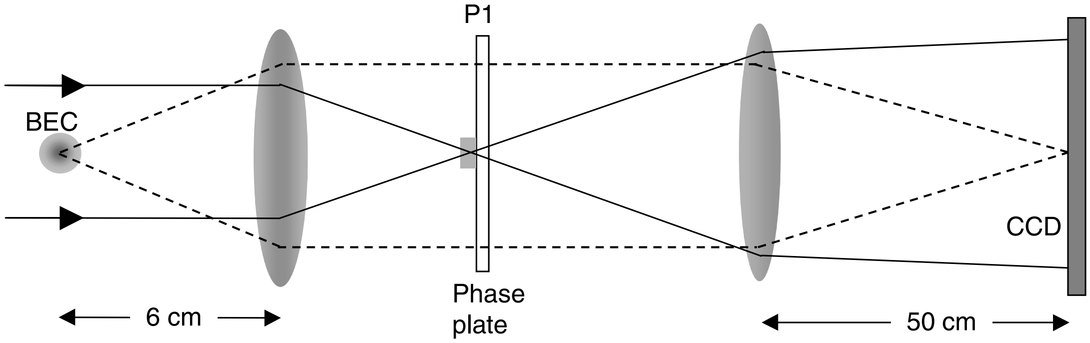

Figure 4.10: Schematic for phase contrast imaging. A probe beam is incident from the left, and obtains a spatially dependent phase shift from the condensate. It travels through the first imaging lens which focuses the probe light onto the phase dot at P1. The phase dot imparts a $\pi/2$ phase shift to only the probe beam, but not to the diffracted light from the condensate. The second lens completes the microscope and images the condensate onto the CCD array.

most successful technique is to first place the dot so that it is not at the focal point of the first lens, so the dot does not encompass the focusing probe. A bull's eye pattern is then observed between the second lens and the CCD. As the phase dot is moved toward the beam focus the bull's eye pattern grows until, at the focus, the profile is flat.

4.3.1 Non-destructive imaging techniques

Both destructive and polarization imaging depend on atom orientation to define a symmetry axis. This is defined by the direction of the rotating TOP field. In the extreme case where the axis switches direction (1/2 of a TOP period later), near-resonance imaging sees a large change in the detuning from resonance, and polarization imaging sees reversed Clebsh-Gordon coefficients, resulting in an opposite polarization rotation. Linearly polarized and far detuned, phase-contrast imaging gives nearly equal signals no matter which direction the TOP field points (see Table 4.1). Where the other methods require strobing of the probe light in order to wait for proper field alignment in the rotating TOP trap, phase-contrast images may be taken at any time, or even continuously.

Discrete, non-destructive pictures of a condensate are taken using kinetics mode of the Princeton Instruments camera (with ST138 controller). In this mode, the camera waits for either an internal or external trigger, at which time it advances the charge on each row of pixels by a set number of rows. A region of N rows may be defined as the exposed area by physically masking the remaining $512 - N$ rows directly in front of the CCD. Once a trigger is received, the charge accumulated on the N rows is advanced into the unexposed area. This advancement occurs at a user-specified speed of 19.2 × (integer multiples up to 16) μs per row. Once the shift is complete the camera waits for a new trigger and repeats the process until the array is filled. The internal trigger mode has a fixed repetition rate, but it is simple to provide arbitrary triggers in the external trigger mode. This latter method can be used to obtain any desired probe timing. Once the CCD is filled, the charge is read from the entire array, digitized and sent to the computer for analysis. In general, we are able to get $\sim$ 12 to 30 pictures of an individual condensate, depending on the condensate size (*i.e.* trap frequencies) and center-of-mass slosh. Figure 4.11 shows a non-destructive series of pictures of a condensate undergoing Rabi oscillations between the $|2,1\rangle$ and $|1,-1\rangle$ states, with a Rabi period of about 5 images.

A semi-continuous movie may also be taken by scrolling the charge on the CCD at a constant rate (or, one can think of scrolling each row discretely as an individual frame). The scroll speed is still given by integer multiples of 19.2 μs per row for internal triggering, which means that the total time ranges from 10 ms to 157 ms. External triggers again enable arbitrarily long frames. Since the condensate image occupies many pixel rows, this method smears out vertical (along the direction of scrolling) density information. However, it is extremely useful for quickly measuring center-of-mass slosh, and quantitatively useful in measuring Rabi frequencies. Figure 4.12 shows a continuous movie of (a) a condensate undergoing Rabi oscillations between the $|2,1\rangle$ and $|1,-1\rangle$ states, and (b) radial and axial center-of-mass slosh.

4.3.2 Signal to noise

Assuming the phase dot thickness is $\pi/2$ and ϕ is small, the signal to noise in phase-contrast is

$$S/N_{\text{shot}} = \frac{\sqrt{I_0}\phi}{\sqrt{(\phi+1)(\phi+2)}} \tag{4.23}$$

for shot noise, and for "fringe noise" it is

$$S/N_{\text{fringe}} = \frac{\phi\sqrt{2}}{A(\phi+1)\sigma} \tag{4.24}$$

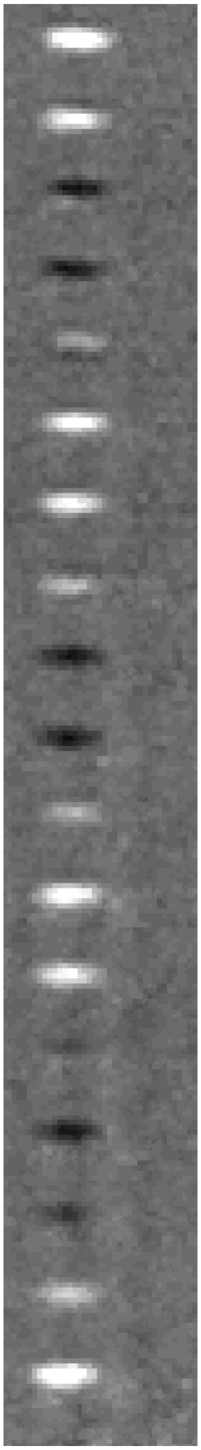

Figure 4.11: Discrete, non-destructive imaging of a condensate undergoing Rabi oscillations. For each image, the probe beam is flashed on and off quickly, and the resulting CCD charge scrolled away from the exposed area. The phase contrast signal is positive (white) for the $|1,-1\rangle$ state and negative (black) for the $|2,1\rangle$ state. The two-photon drive is on during for the duration of the images.

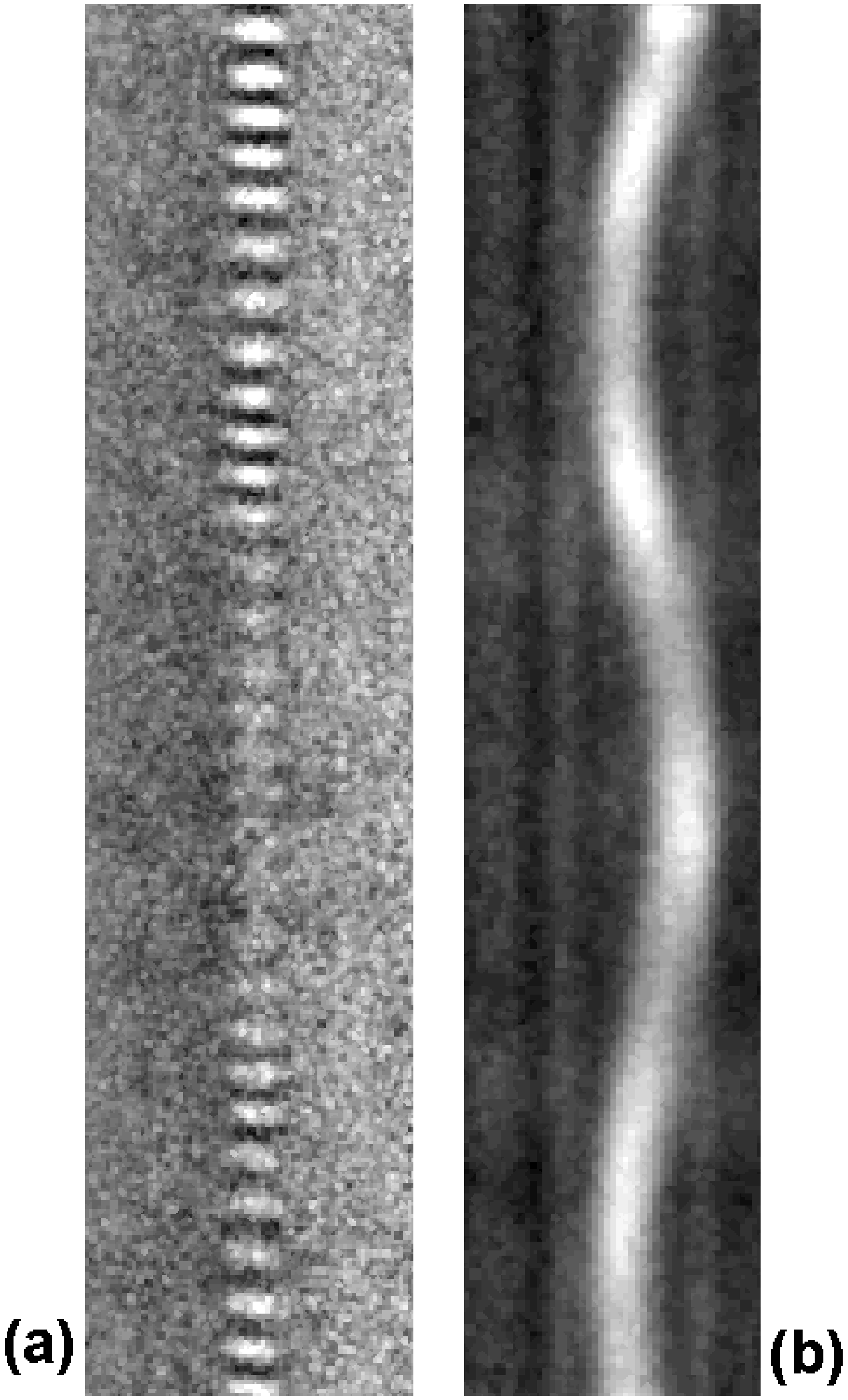

Figure 4.12: Continuous, non-destructive images. (a) A condensate undergoing Rabi oscillations (with collapse and revival). (b) A single condensate in the $|1,-1\rangle$ state oscillating radially (horizontally in the picture) and axially (vertically in the picture). The axial oscillation is manifested as an increase (decrease) in the signal as the condensate moves with (against) the CCD scrolling.

The shot noise limit was experimentally observed in figure 4.13 for a trapped condensate in a 62 Hz axial trap.

4.4 Comparisons

The next section compares the three imaging techniques based on their usefulness for a specific measurement. The criteria are measurement of density distributions, signal to noise, double condensate signal, and non-destructive movies.

Single and two-state condensate density distributions are best imaged after ballistic expansion with destructive imaging. The main reason is that the imaging resolution is $\sim 5\mu$m, too small for a common 10 μm cloud (although reasonable for 50μm condensates in very weak traps). With destructive imaging we are sensitive to $< 5\%$ deviations in overall condensate size when looking at collective excitations. The major drawback here is that time dependence cannot be studied using a single condensate; each time step point must be taken with a fresh condensate, requiring more experiment stability. It is also necessary to mathematically reconstruct the condensate's image as it was in the trap before expansion using the nonlinear Schrödinger equation. However, qualitative reconstruction is generally possible using scaling and scattering length arguments.

Signal to noise in overall condensate number is generally the best for polarization imaging in the trap. This is the case when the noise is dominated by spatial intensity fluctuations on the probe laser since the polarizers may be crossed to eliminate background light. In order to get spatial information, the profile of the probe must be flat on the scale of the condensate in order to forgo the background subtraction which is not possible for crossed polarizers. If the imaging resolution is larger than the condensate, then it is better to destructively image a dropped cloud near resonance.

Phase-contrast is the best technique for double condensate imaging and for

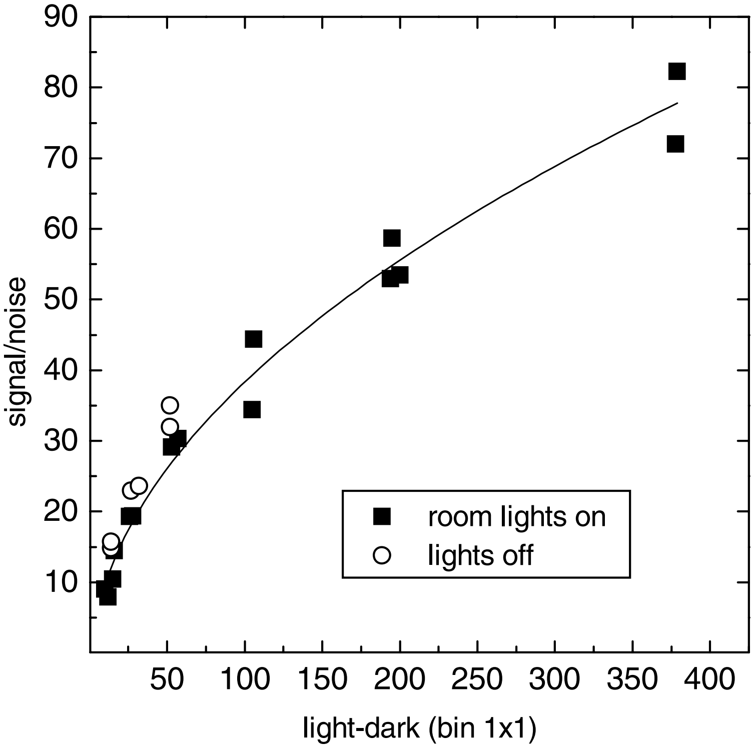

Figure 4.13: Plot of the experimental signal to noise of a condensate in the trap, as a function of probe light level I for phase contrast imaging. The solid line is a fit to the shot noise limit which is proportional to $\sqrt{(I)}$.

multiple images of the same condensate. Although polarization imaging has better signal to noise for crossed polarizers, no state specific information is possible (both + and - polarization rotations give the same signal) in that configuration. Phase-contrast is still better than polarization (with uncrossed polarizers) due to its smaller dependence on magnetic field direction.

The biggest noise contribution is usually spatial variations in the beam intensity that change position between the condensate picture and the background picture. These seem to be due to interference implanted by multiple reflections from optical surfaces, or diffraction from aperaturing of the beam or from small imperfections on the optics (dust for example). The size scale is often near the scale of whatever is being imaged, which seems to indicate that multiple patterns and sizes are present. There are a few techniques which have helped to diminish the effect of the stripes. Changing the alignment of optics (beamsplitters, polarizers) before and after the trap has helped. Occasionally, changing the magnetic trap parameters from the condensate image to the background image has an effect. Since the rotating magnetic field produces audible noise, it causes vibrations in the optics and windows, which modulates the fringe pattern. It has helped to find specific phases and amplitudes of the rotating field to minimize the difference between the two frames.

Chapter 5

Double Condensate experiments – density related [2]

5.1 Introduction

An alluring aspect of atomic Bose-Einstein condensates has been their ideal representation of the fundamental physics of particle statistics. Other systems such as ^{3}He and superconductors mask the basic phenomenon through overwhelming inter-particle interactions, due to their relatively high densities. Atomic condensates also experience interatomic potentials, but the separation between atoms is much larger than the scale of these interactions, making the condensate dilute in this sense. Despite complicated interatomic potentials, the mean-field interaction in condensates is well-characterized by a single parameter, the s-wave scattering length a. Qualitatively, a system is dilute when the scattering "volume" is much smaller than the inverse density, *i.e.* $a^3 n \ll 1$. These interactions have an important effect on most condensate physics, including density and momentum distributions [106, 80], collective excitations [91, 107], specific heat [60, 69], speed of sound [37], and limited condensate number[42]. In the present context of double condensates, there are three important values of the scattering; the self-repulsion for each state and the mutual repulsion between the states.

The first demonstration of a binary mixture of condensates by Myatt *et al.*[108] produced overlapping condensates of the $5S_{1/2}$ $|F=1, m_f=-1\rangle$ and $|F=2, m_f=2\rangle$ states of ^{87}Rb. The ratio of the magnetic moments of these states is 1:2, so the condensates experience different potentials in a magnetic trap and are displaced unequally from the trap center by gravity. Due to an accidental coincidence between the singlet and triplet scattering lengths of ^{87}Rb, collisional loss is reduced and any mixture of spin states will be relatively long-lived [108, 94, 45]. Here, we use mixtures of $|1,-1\rangle$ and $|2,1\rangle$ states, which possess several advantages. First, these two states have essentially identical magnetic moments, and hence feel identical confining potentials. Second, one can conveniently and quickly change atoms from the $|1,-1\rangle$ state to the $|2,1\rangle$ state by a two-photon transition (microwave plus rf). Finally, we can selectively image the different components using appropriately tuned lasers.

Using the two-photon drive the $|1,-1\rangle$ and $|2,1\rangle$ states can be treated as a two level system. When the two-photon drive is off the energy difference is much larger than the energy available from kinetic or potential contributions (a few kHz compared to 6.8 GHz), so that two condensates in each of these states are distinguishable, scalar condensates. In the presence of the drive, atoms interconvert between the hyperfine states coherently. This chapter is not concerned with the phase or coherence between the two states, but only with their density profile and dynamics as governed by the scattering lengths.

The evolution of the double condensate system, including release from the trap and subsequent expansion [79], is governed by a pair of coupled Gross-Pitaevskii equations for condensate amplitudes Φ_i:

$$i\hbar\frac{\partial\Phi_i}{\partial t} = \left(-\frac{\hbar^2\nabla^2}{2m} + V_i + U_i + U_{ij}\right)\Phi_i \tag{5.1}$$

where $i, j = 1, 2$ $(i \neq j)$, V_i is the magnetic trapping potential for state i, the mean-field potentials are $U_i = 4\pi\hbar^2 a_i|\Phi_i|^2/m$ and $U_{ij} = 4\pi\hbar^2 a_{ij}|\Phi_j|^2/m$, m is the mass of the Rb atom, and the intraspecies and interspecies scattering lengths are a_i and a_{ij}. This equation is numerically integrated by various authors to compare with experiment.

The following experiments are all done on a time scale faster than the decay of atoms from inelastic processes. In Eq. 5.1 it is the real part of a which governs the elastic, and the imaginary part which determines the inelastic collisions. For our system of condensates, it is the inelastic spin-exchange process which occurs the fastest, whereby two $|2,1\rangle$ atoms collide to produce one $|2,0\rangle$ and one $|2,2\rangle$ atom (or possibly $|1,0\rangle$ and $|2,2\rangle$). These atoms are effectively lost from the trap. We have measured an upper limit to this loss rate as $3 \times 10^{-13}\mathrm{cm}^3/\mathrm{s}$.

5.2 Dynamical response-instantaneous change in scattering length

As an initial experiment we apply a short π-pulse to convert the initial $|1,-1\rangle$ condensate instantaneously into a $|2,1\rangle$ condensate. Our analysis of the ensuing behaviour does not require the interatomic term in Eq. 5.1 since the two states do not exist at the same time. Because these two states have slightly different values of a, the sudden change in self-interaction gives rise to oscillatory spatial behavior of the condensate wave function [96]. The scattering length ratio can be extracted from a model using analytical equations of motion for the condensate widths [96, 95, 52] based on Gross-Pitaevskii theory.

We have investigated the dynamical behavior of the condensate after more than 99.5% of the atoms are transferred from the $|1,-1\rangle$ state to the $|2,1\rangle$ state. After the transfer, the condensate is allowed to evolve in the trap for a time interval T before the cloud is released from the trap and probed. The experiment is repeated for different values of T, and the axial and radial widths of the condensate are measured using a fit to the two-dimensional condensate image, using the integrated-through Thomas-Fermi form. Fig. 5.1 illustrates the time dependence of both the axial and radial size of the atom cloud. Qualitatively, the data for both dimensions are consistent with a “compression” oscillation. The condensate shrinks for very early times, indicating a weaker mean-field repulsion in the $|2,1\rangle$ state.

In order to describe the response to the change in scattering length, we use the Gross-Pitaevskii (GP) equation for the condensate wave function, with a time-dependent interaction term:

$$i\hbar\frac{\partial\Phi(\mathbf{r},t)}{\partial t} = \left[-\frac{\hbar^2\nabla^2}{2m} + V(\mathbf{r}) + U(t)|\Phi(\mathbf{r},t)|^2\right]\Phi(\mathbf{r},t)\ , \qquad (5.2)$$

where $U(t) = 4\pi\hbar^2 a(t)/m$. For $t < 0$, $a(t) = a_1$, the scattering length for $|1,-1\rangle$ atoms on $|1,-1\rangle$ atoms. For $t > 0$, $a(t) = a_2$, the $|2,1\rangle$ on $|2,1\rangle$ scattering length. The condensate is formed in its ground-state in which the density profile $n(\mathbf{r}) = |\Phi(\mathbf{r})|^2$ is constant in time, and with the axial and radial widths (w_z, w_r) determined by $V(\mathbf{r})$, a_1, and the number of atoms N. After a sudden change in $a(t)$, $\Phi(\mathbf{r},t)$ is projected onto a coherent superposition of its new ground-state and collective vibrational modes. Instead of solving the complete GP equation, one can use the Thomas-Fermi (TF) approximation, which corresponds to neglecting the quantum pressure term in the kinetic energy of the condensate. In this case, one can replace the GP equation with a pair of scalar equations of motion for the condensate widths [96, 95, 52]:

$$\ddot{w}_i + (2\pi\nu_i)^2 w_i - \left(\frac{15\hbar^2 N a(t)}{7^{5/2}m^2}\right)\frac{1}{w_r^2 w_z w_i} = 0\ . \qquad (5.3)$$

Here the widths $w_r = \sqrt{\langle r^2\rangle}$ and $w_z = \sqrt{\langle z^2\rangle}$ are the radial and axial rms radii, and the subscript i is to be replaced with either r or z for the respective widths. The TF approximation holds when N is large [13] and, in this limit, the GP theory coincides with the hydrodynamic theory of superfluids [130].

Time-dependent behavior is predicted by numerically integrating Eqs. 5.3. The initial conditions ($t < 0$) are that the widths are at the values determined by the ground-state solution, $\dot{w}_r = \dot{w}_z = 0$, and $a(t) = a_1$. After $t = 0$, $a(t) = a_2$ and the integration proceeds for time T. We model the removal of the trap by setting $\nu_r = \nu_z = 0$ and continue the numerical integration for the 22 ms free expansion. The axial and radial widths subsequently expand with different speeds. In the TF approximation, the ratio between the two expanded widths, averaged over T, can be shown to depend only on ν_r, ν_z and the expansion time [52]. In our case, the theory predicts $w_z/w_r = 1.29$, in good agreement with the measured value $w_z/w_r = 1.31$. The oscillations of the widths correspond to a superposition of two $m = 0$ modes. Since no angular momentum is imparted to the condensate by the change of scattering length, these are the only modes excited. The calculated mode frequencies are $\nu/\nu_r = 1.80$ and $\nu/\nu_r = 4.99$, and turn out to be independent of the amplitude in the range considered here. The two modes contribute to the oscillations in z and r with a different phase and amplitude, the axial motion behaving mainly as the fast mode and the radial motion as the slow one.

In each direction, the ratio of the amplitudes of the two modes is predicted to be constant over the range of possible scattering lengths relevant to the experiment. Thus, only the initial size and an overall amplitude are used as adjustable parameters in comparison of theory with experiment. The solid lines in Fig. 5.1 show the theoretical prediction using the best fit value of the oscillation amplitude, which is related to the scattering length ratio a_1/a_2. The predicted oscillations agree remarkably well with the shape of the data, for both the frequency and the phase of the two modes. From the fit amplitude we obtain the ratio of the scattering lengths $a_1/a_2 = 1.062 \pm 12$, which is consistent with the ratio of 1.059^{+4}_{-6} obtained in a theoretical calculation of binary collision parameters [46, 131].

Analysis of the data is complicated slightly by an observed systematic dependence of the oscillation amplitude on the magnitude of the rf drive during the two-photon pulse. We believe that this effect is partly due to a small dressing of the atoms to the $|1, 0\rangle$ or $|2, 0\rangle$ state by the rf, and partly due to a coupling

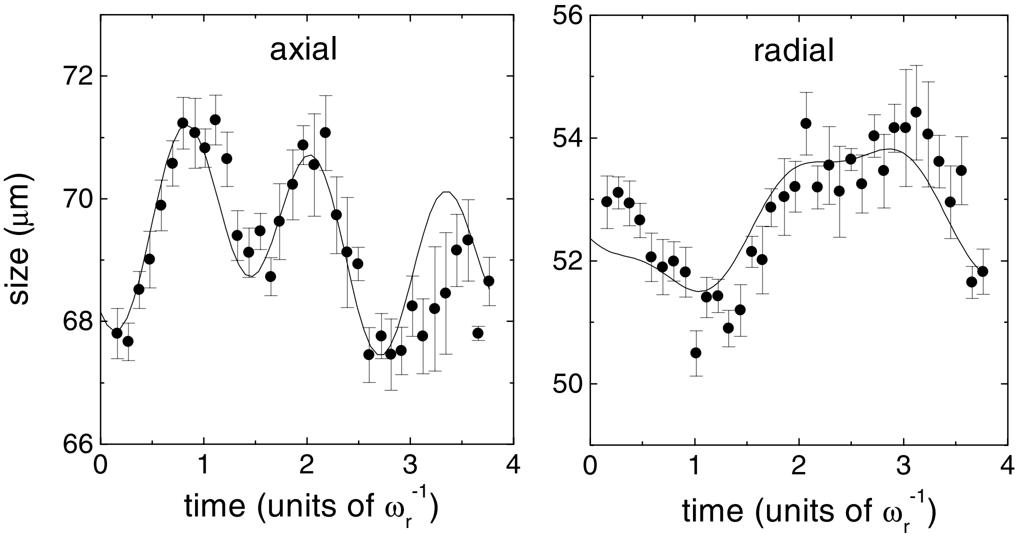

Figure 5.1: Oscillation in the width of the cloud in both the axial and radial direction due to the instantaneous change in scattering length. The widths are for condensates as a function of free evolution time in units of the radial trap period ($\omega_r^{-1} = 9.4$ ms), followed by 22 ms of ballistic expansion. Each point is the average of approximately 10 measurements. Note that the fractional change in width is quite small. The solid line is a fit of the model to the data, with only the amplitude of the oscillation and the initial size as free parameters.

of the rf onto electronics controlling the trap potential. Both result in a change in strength of the confining potential during the two-photon pulse which returns to normal when the pulse is complete. After this impulsive perturbation, the BEC can be thought of as freely evolving with an initial "velocity" in the width ($\dot{w}_r, \dot{w}_z \neq 0$). This is in contrast to the discrete change in scattering length, in which the BEC width has an initial offset from the equilibrium width, but no initial velocity. The systematic is manifested as an initial offset in the phase of the resulting oscillation, which is indeed observed for large rf amplitudes. Our result for the ratio was obtained by extrapolating to zero rf amplitude with a quadratic fit as shown in Fig. 5.2.

5.3 Mixtures of condensates

In this experiment, we report results from initial studies of simultaneously trapped BECs in the $|2\rangle$ and $|1\rangle$ states. The condensates begin with a well-defined relative phase, spatial extent, and "sag" — the position at which the magnetic trapping forces balance gravity for each state. The fine experimental control of this double condensate system permits us to study its subsequent time-evolution under a variety of interesting conditions, most notably those in which there remains substantial spatial overlap between the two states.

The double condensate system is prepared from the single $|1\rangle$ condensate by driving the two-photon transition. We are able to transfer quickly any desired fraction of the atoms to the $|2\rangle$ state by selecting the length and amplitude of the two-photon pulse. The two condensates are created with identical density distributions, after which they evolve and redistribute themselves for some time T. We then turn off the magnetic trap and allow the atoms to expand for 22 ms for imaging.

We selectively image the densities of either of the two states (n_1 and n_2) or

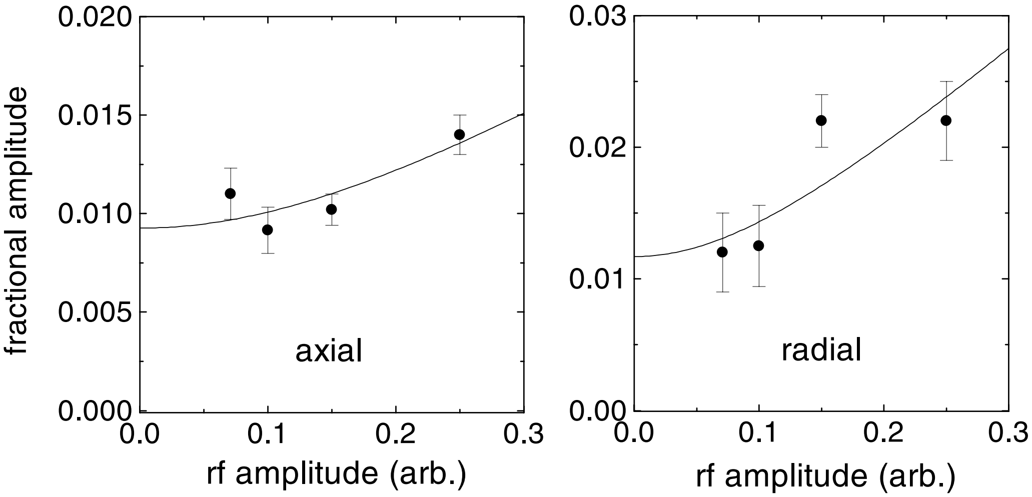

Figure 5.2: Dependence of the oscillation amplitude on the rf strength in the two-photon transition. The vertical axis represents the fitted value of the fractional excitation amplitude, with error bars from uncertainty in the fit. The solid line shows extrapolation to zero rf amplitude.

the combined density distribution (n_T) by changing the sequence of laser beams applied to the condensates for probing (see Chapter 4). Since the expansion and imaging are destructive processes, each image is taken with a different condensate; the excellent reproducibility of the condensates permits us to study the time-evolution of the system by changing the time T. The images of the condensates do not always appear in the same absolute locations on the CCD-array detector, however, and we compensate for this shot-to-shot jitter by reconstructing the relative positions of the condensates from the images of n_1, n_2, and n_T at each time T.

The evolution of the double condensate system, including the release from the trap and subsequent expansion [36, 79], is governed by a pair of coupled Gross-Pitaevskii equations in Eq. 5.1. In the Thomas-Fermi limit, the condensate density distributions are dominated by the potential energy terms of Eq. (5.1). Consequently, the expanded density distributions retain their spatial information and emerge with their gross features (such as the relative position of the condensates) intact.

The similarity in scattering lengths a_1, a_2, and a_{12} implies that the total density n_T will not change significantly from its initial configuration even though the two components may redistribute themselves dramatically during the evolution time T. In ^{87}Rb, the scattering lengths are known at the 1% level to be in the proportion $a_1 : a_{12} : a_2 :: 1.03 : 1 : 0.97$, with the average of the three being 55(3) Å [46, 105]. The near-preservation of the total density n_T can be approached theoretically by deriving from Eq. (5.1) the hydrodynamic equations of motion [136] for n_T and evaluating them in the limit that the fractional differences between the scattering lengths are small. The pressures that tend to redistribute n_T must also be small. A similar argument pertains if the minima of the trapping potentials V_1 and V_2 are displaced from one another (see below) by a distance that is small compared to the size of the total condensate; once again, the effects on the equilibrium distribution of the individual components may be profound but the total density should remain largely unperturbed [63].

The rotating magnetic field of the TOP trap gives rise to a subtle behavior that permits us to displace the minima of the trapping potentials V_1 and V_2 with respect to one another (Chapter 3). By adjusting trap parameters, we can change the sign of the relative sag or cause it to vanish while preserving (to first order) the same radial (ν_r) and axial ($\nu_z = \sqrt{8}\nu_r$) trap oscillation frequencies.

In a first experiment, we choose a trap that has zero relative sag ($\nu_z = 47$ Hz) and transfer 50% of the atoms to the $|2\rangle$ state with a ~ 400 μs pulse. When $T = 30$ ms, we observe a "crater" in the image of the $|1\rangle$ atoms (Fig. 5.3a). The "crater" corresponds to a region occupied by the $|2\rangle$ atoms (Fig. 5.3b), indicating that the $|1\rangle$ atoms have formed a shell about the $|2\rangle$ atoms. This is consistent with the theoretical prediction that it is energetically favorable for the atoms with the larger scattering length ($|1\rangle$) to form a lower-density shell about the atoms with the smaller scattering length ($|2\rangle$) [119]. At later times the $|2\rangle$ atoms break radial symmetry and drift transversely away from the center of the cloud, possibly due to a tilt of the rotating TOP field with respect to the quadrupole field axis shown in Fig. 5.4.

In order to explore the boundary between the two condensates, we perform a series of experiments in a trap in which we displace the trapping potentials such that the minimum of V_2 is 0.4 μm lower than that of V_1, or approximately 3% of the (total) extent of the combined density distribution in the vertical direction. The subsequent time-evolution of the system is shown in Figs. 5.5 and 5.6. The two states almost completely separate (Fig. 5.5a-c) after 10 ms; they then "bounce" back until at $T = 25$ ms the centers-of-mass are once more almost exactly superimposed (Fig. 5.6), although a distinctive (and reproducible) vertical

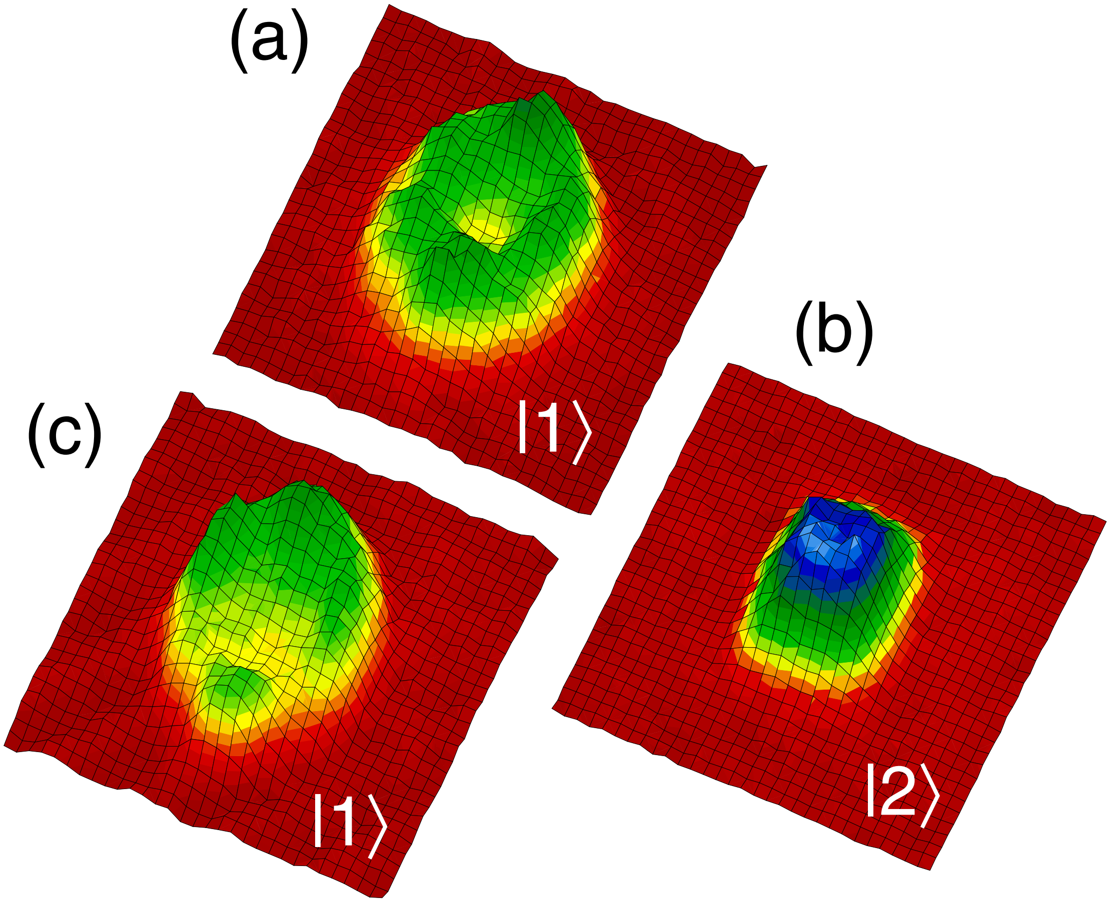

Figure 5.3: (a) The image of the $|1\rangle$ condensate exhibits a “crater,” corresponding to a shell in which the $|2\rangle$ atoms (b) reside. For this trap, $\nu_z = 47$ Hz with zero relative sag. By changing the strength of the magnetic quadrupole field we can introduce a nonzero relative sag, which shifts the location of the “crater” (c). (Each square in this post-expansion image is 136 μm on a side.)

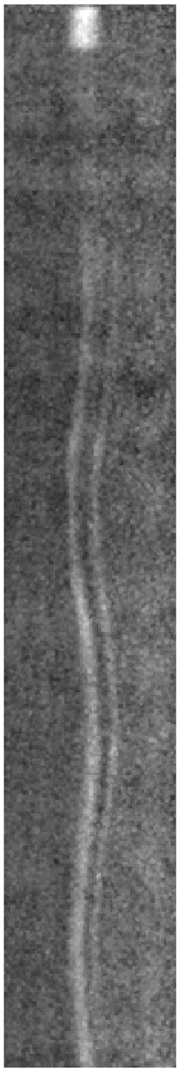

Figure 5.4: A streak camera image of a 50-50 mixture of $|1,-1\rangle$ and $|2,1\rangle$ atoms in a condensate. The trap is 47 Hz axial. Time increases from the top to the bottom (total time is 154 ms), and left-right is the "radial" direction. At the top of the frame, a $|1,-1\rangle$ condensate (white) is put into a 50-50 mixture by a $\pi/2$ pulse. At the end of the pulse the condensate becomes grey; invisible to the phase-contrast imaging. As time progresses we begin to see separation of the two states, with the $|1,-1\rangle$ atoms favoring a shell outside the $|2,1\rangle$ atoms. For even longer times the cylindrical symmetry is broken as the $|2,1\rangle$ atoms move to the right.

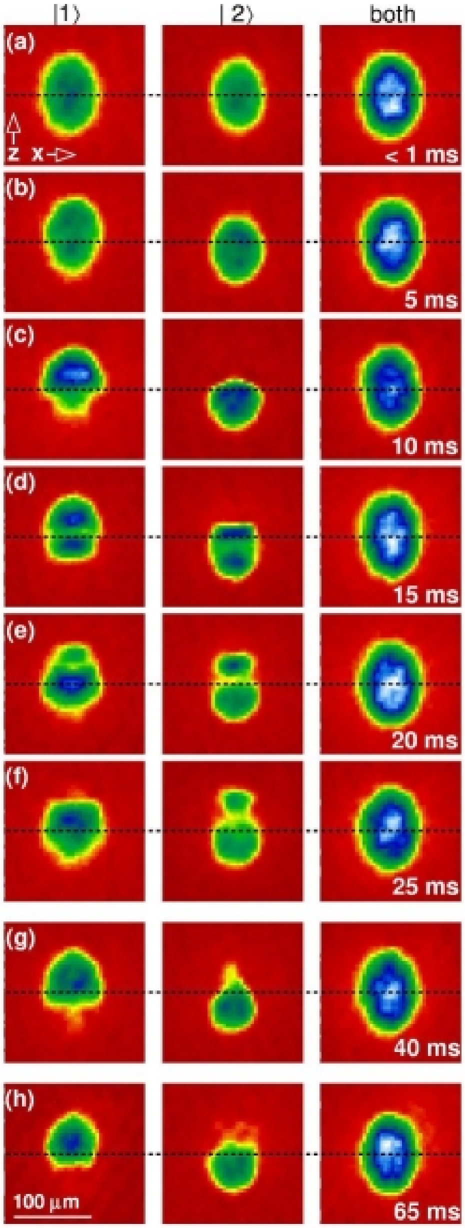

Figure 5.5: Time-evolution of the double-condensate system with a relative sag of 0.4 μm (3% of the width of the combined distribution prior to expansion) and a trap frequency $\nu_z = 59$ Hz.

structure has formed (Fig. 5.5d-e-f). By $T = 65$ ms, the system has apparently reached a steady state (Fig. 5.5g-h, Fig. 5.6) in which the separation of the centers-of-mass is 20% of the extent of the entire condensate. From these images we observe: (i) the fractional steady-state separation of the expanded image is large compared to the fractional amount of applied symmetry breaking, as we expect for a repulsive interspecies potential; (ii) the placid total density profile (rightmost column of Fig. 5.5) betrays little hint of the underlying violent rearrangement of the component species; and (iii) the component separation is highly damped, although it is not yet certain what mechanism [124, 117, 96, 116, 103, 65] is responsible. With respect to the damping, the excitation is not small and may therefore be poorly modeled by theories that treat the low-lying, small-amplitude excitations [70, 47, 72, 62, 118] of double condensates.

It should be noted that after many months since this data was taken, the long time behavior is not reproduced. The qualitative behavior is the same but no longer do we see the center of mass of the two states damp as significantly as in Fig. 5.5. A few experimental details have changed. The rotating TOP field is controlled by electronics with much less noise. We have also adjusted the roundness of the TOP field. It is possible that our evaporation has changed so that a smaller thermal fraction remains now than at the time of this experiment.

Finally, we show the optical density as a function of relative number and position on the condensate vertical axis in order to better appreciate the amount of overlap between the two states at $T = 65$ ms (Fig. 5.7), which remains substantial despite the underlying separation. Each plot is averaged across a ~ 14 μm wide vertical cut through the centers of the two condensates. From the overlap shown, one could determine the magnitude of the interspecies scattering length a_{12} by comparison to theoretical calculations conducted within the Thomas-Fermi ap-

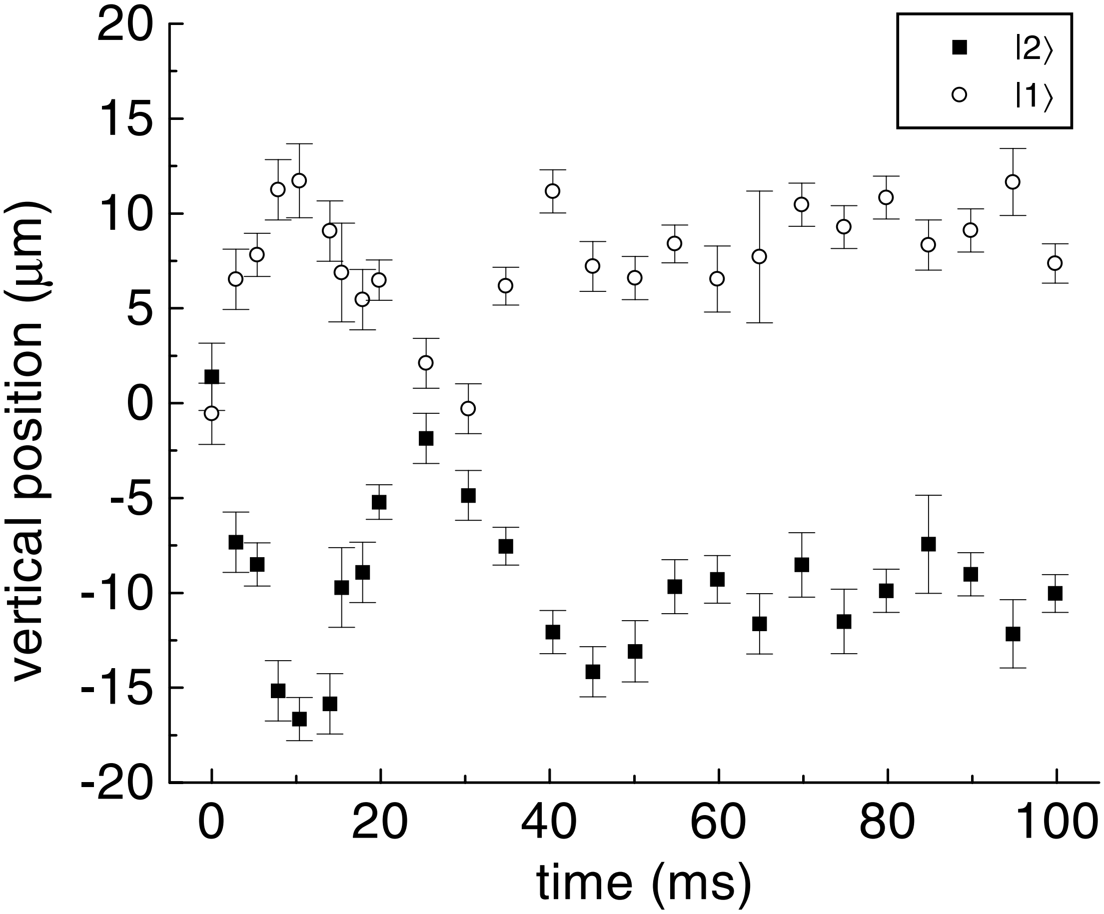

Figure 5.6: The relative motion of the centers-of-mass of the two condensates under the same conditions as those in Fig. 5.5.

proximation [78] and numerical solutions of the Gross-Pitaevskii [118] or Hartree-Fock [64] equations.

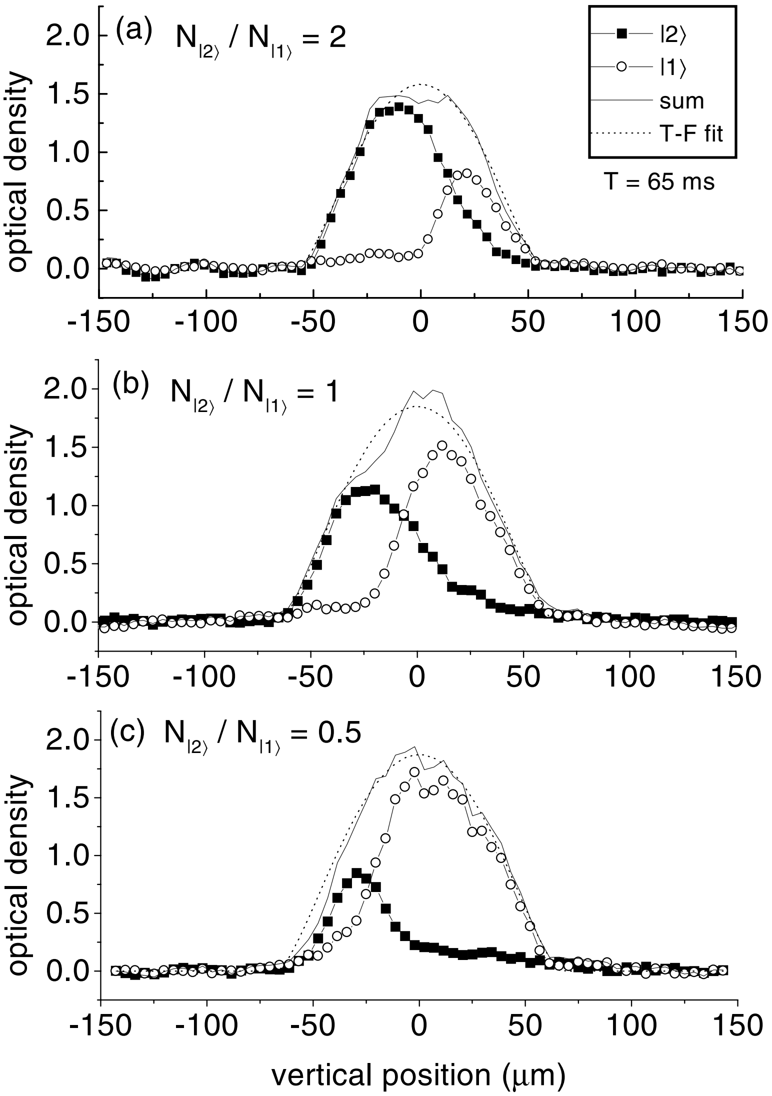

Figure 5.7: Vertical cross-sections of the density profiles at $T = 65$ ms for different relative numbers of atoms in the two states. The combined density distribution (solid line) is shown for comparison to the Thomas-Fermi parabolic fit (dashed line). The trap parameters are the same as those in Fig. 5.5.

Chapter 6

Double condensate experiments – phase related [3]

The relative quantum phase between two Bose-Einstein condensates is expected to give rise to a variety of interesting behaviors, most notably those analogous to the Josephson effects in superconductors and superfluid ^{3}He [40]. Experiments with condensates realized in the dilute alkali gases [36, 54, 43] have recently drawn considerable theoretical attention, with a number of papers addressing schemes [88, 83, 123] by which to measure the relative phase. Two independent condensates are expected to possess [41] (or develop upon measurement [87, 49]) a relative phase which is essentially random in each realization of the experiment. The experimental observation at MIT of a spatially uniform interference pattern formed by condensates released from two independent traps confirms the existence of a single relative phase [14]. In the next three chapters the phase is measured and manipulated in ways which have strong analogies to liquid helium physics. In this first experiment, we use an interferometric technique to measure the relative phase (and its subsequent time-evolution) between two trapped condensates [15] that are created with a particular relative phase. This system permits us to characterize the effects of couplings to the environment on the coherence [16] between the condensates.

As in our previous work [105, 76], we create a condensate of approximately 5×10^5 Rb-87 atoms, confined in the $|F = 1, m_f = -1\rangle$ ($|1\rangle$) state in a TOP magnetic trap. The rotating magnetic field ($\nu_{\rm AF} = 1800$ Hz) is ramped to 3.4 G and the quadrupole gradient to 130 G/cm, resulting in a trap with an axial frequency $\nu_z = 59$ Hz. The fields are chosen to make the hyperfine transition frequency nearly field-independent [75]. We create the second condensate by applying a short (~ 400 μs) two-photon pulse that transfers 50% of the atoms ($\frac{\pi}{2}$-pulse) from the $|1\rangle$ spin state to the $|F = 2, m_F = 1\rangle$ ($|2\rangle$) spin state. The coupling drive has an effective frequency of 6834.6774 MHz and is detuned slightly (~ 100 Hz) from the expected transition frequency in our trap [17]. After an evolution time T and an optional second $\frac{\pi}{2}$-pulse, we release the condensates from the trap, allow them to expand, and image either of the two density distributions [105]. The post-expansion images preserve the relative positions and gross spatial features of the condensates as they were in the trap [76, 18].

The evolution of the double condensate system, including the coupling drive, is governed by a pair of coupled Gross-Pitaevskii equations for condensate amplitudes Φ_1 and Φ_2:

$$i\hbar\dot{\Phi}_1 = (T + V_1 + U_1 + U_{12})\,\Phi_1 + \frac{\hbar\Omega(t)}{2} e^{i\omega_{\rm rf}t}\Phi_2 \tag{6.1}$$

and

$$i\hbar\dot{\Phi}_2 = (T + V_2 + V_{\rm hf} + U_2 + U_{21})\,\Phi_2 + \frac{\hbar\Omega(t)}{2} e^{-i\omega_{\rm rf}t}\Phi_1 \tag{6.2}$$

where $T = -(\hbar^2/2m)\nabla^2$ is the kinetic energy, m is the mass of the Rb atom, $V_{\rm hf}$ is the magnetic field-dependent hyperfine splitting between the two states in the absence of interactions, condensate mean-field potentials are $U_i = 4\pi\hbar^2 a_i n_i/m$ and $U_{ij} = 4\pi\hbar^2 a_{ij} n_j/m$, $n_i = |\Phi_i|^2$ is the condensate density, and the intraspecies and interspecies scattering lengths [105, 76] are a_i and $a_{ij} = a_{ji}$. For the trap parameters given above, the harmonic magnetic trapping potentials V_1 and V_2 are displaced from one another by 0.4 μm along the axis of the trap [75]. The coupling drive is represented here in the rotating wave approximation and is characterized by the sum of the microwave and rf frequencies, ω_{rf}, and by an effective Rabi frequency $\Omega(t)$, where

$$\Omega(t) = \begin{cases} 2\pi \cdot 625 \text{ Hz}, & \text{coupling drive on;} \\ 0, & \text{coupling drive off.} \end{cases} \tag{6.3}$$

Phase-sensitive population transfer between the $|1\rangle$ and $|2\rangle$ states occurs with the drive on, but the two condensates become completely distinguishable once the drive is switched off [76]. The first $\frac{\pi}{2}$-pulse [Fig. 6.1(b)] creates the $|2\rangle$ condensate with a repeatable and well-defined relative phase with respect to the $|1\rangle$ condensate at $t = 0$. The relative phase between the two condensates subsequently evolves at a rate proportional to the local difference in chemical potentials between the two condensates $\omega_{21}(\vec{r}, t)$, which in general is a function of both time and space. Couplings to the environment [20] can induce an additional (and uncharacterized) diffusive precession of the relative phase, leading to an rms uncertainty in its value $\Delta\varphi_{\text{diff}}$ [101, 21]. After an evolution time T, therefore, the condensates have accumulated a relative phase $\int_0^T \omega_{21}(r, t)\, dt + \Delta\varphi_{\text{diff}}(T)$. During the same time, the coupling drive accumulates a phase $\omega_{\text{rf}}T$. A second $\frac{\pi}{2}$-pulse [Fig. 6.1(e)] then recombines the $|1\rangle$ and $|2\rangle$ condensates, comparing the relative phase accumulated by the condensates to the phase accumulated by the coupling drive. The resulting phase-dependent beat note is manifested in a difference in the condensate density between the two states. Immediately after the second pulse the density in the $|2\rangle$ state (n_{2f}) is

$$n_{2f}(\vec{r}) = \frac{1}{2}n_1(\vec{r}) + \frac{1}{2}n_2(\vec{r}) + \sqrt{n_1(\vec{r})n_2(\vec{r})} \cos\left[\left(\int_0^T \omega_{21}(\vec{r}, t)\, dt\right) - \omega_{\text{rf}}T + \Delta\varphi_{\text{diff}}(T)\right]. \tag{6.4}$$

In this equation, n_i denote the densities prior to the application of the second $\frac{\pi}{2}$-pulse. The interference term in Eq. 6.4 shows that measurement of $n_{2f}(\vec{r})$ in the overlap region is sensitive to the relative phase. Each realization of the experiment (with a freshly-prepared condensate) yields a measurement of the relative phase

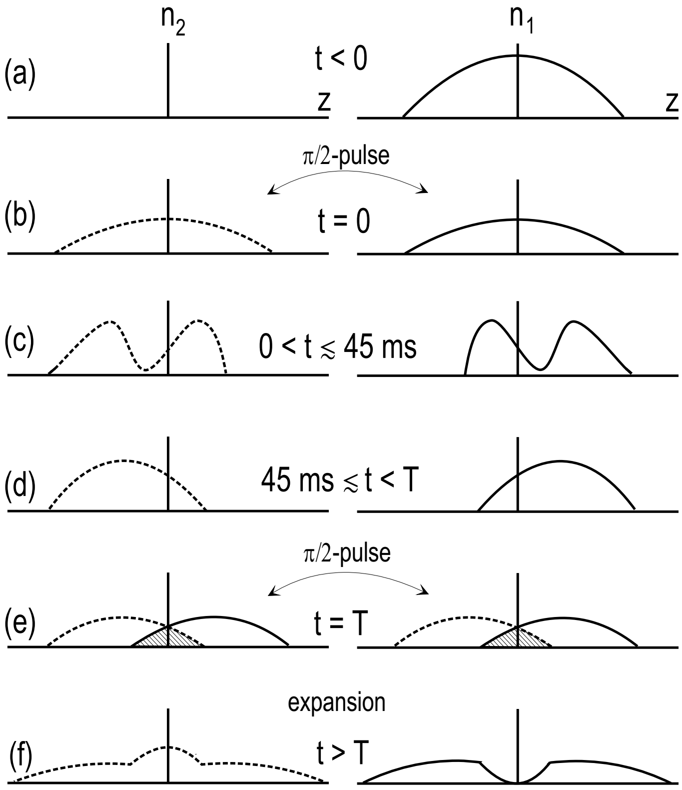

Figure 6.1: A schematic of the condensate interferometer [19]. (a) The experiment begins with all of the atoms in condensate $|1\rangle$ at steady-state. (b) After the first $\frac{\pi}{2}$-pulse, the condensate has been split into two components with a well-defined initial relative phase. (c) The components begin to separate in a complicated fashion due to mutual repulsion as well as a 0.4 μm vertical offset in the confining potentials (see also Fig. 3 of Ref. [76]). (d) The relative motion between the components eventually damps with the clouds mutually offset but with some residual overlap. Relative phase continues to accumulate between the condensates until (e) at time T a second $\frac{\pi}{2}$-pulse remixes the components; the two possible paths by which the condensate can arrive in one of the two states in the hatched regions interfere. (f) The cloud is released immediately after the second pulse and allowed to expand for imaging. In the case shown, the relative phase between the two states at the time of the second pulse was such as to lead to destructive interference in the $|1\rangle$ state and a corresponding constructive interference in the $|2\rangle$ state.

for a particular T; by varying T, we can measure the evolution of the relative phase.

At short times T, for which the overlap between the condensates remains high, varying the moment at which the second $\frac{\pi}{2}$-pulse is applied causes an oscillation of the total resulting number of atoms in the $|2\rangle$ state. The oscillation occurs at the detuning frequency $\delta = \omega_{21} - \omega_{\mathrm{rf}}$ and is completely analogous to that observed in separated-oscillatory-field measurements in thermal atomic beams [121] or in cold (but noncondensed) atoms in a magnetic trap [50]. The fringe contrast, initially 100%, decreases as the condensates separate. After ~ 45 ms the relative center-of-mass motion damps and comes to equilibrium, leaving the components with a well-defined overlap region at their boundary, as shown in Figs. 6.1(d) and 6.2(a); see also Fig. 5(b) of Ref. [76]. Application of a second $\frac{\pi}{2}$-pulse at $T > 45$ ms results in a density profile in which the interference occurs only in the overlap region; see Figs. 6.1(f) and 6.2(b). We look at the density of atoms in the $|2\rangle$ state at the center of the overlap region [22] in order to examine the intriguing issue of the reproducibility of the relative phase accumulated by the condensates during the complicated approach to equilibrium. If the phase diffusion term in Eq. 6.4 is so large that the uncertainty is greater than π, then repeated measurements for the same values of T will yield an incoherent (*i.e.*, random) ensemble of interference patterns. In the opposite extreme, (*i.e.*, very little phase diffusion), repeated measurements will give essentially the same interference pattern at T in each experimental run. We plot the optical density in the center of the overlap region as a function of T in Fig. 6.3, and observe an oscillation at the detuning frequency with a visibility of approximately 50%, corresponding to an rms phase diffusion $\Delta\varphi_{\mathrm{diff}}(T) < \frac{\pi}{3}$. At longer times the maximum contrast observed in a single realization of the experiment decreases slightly, possibly due to the increasing presence of thermal atoms as the condensates decay.

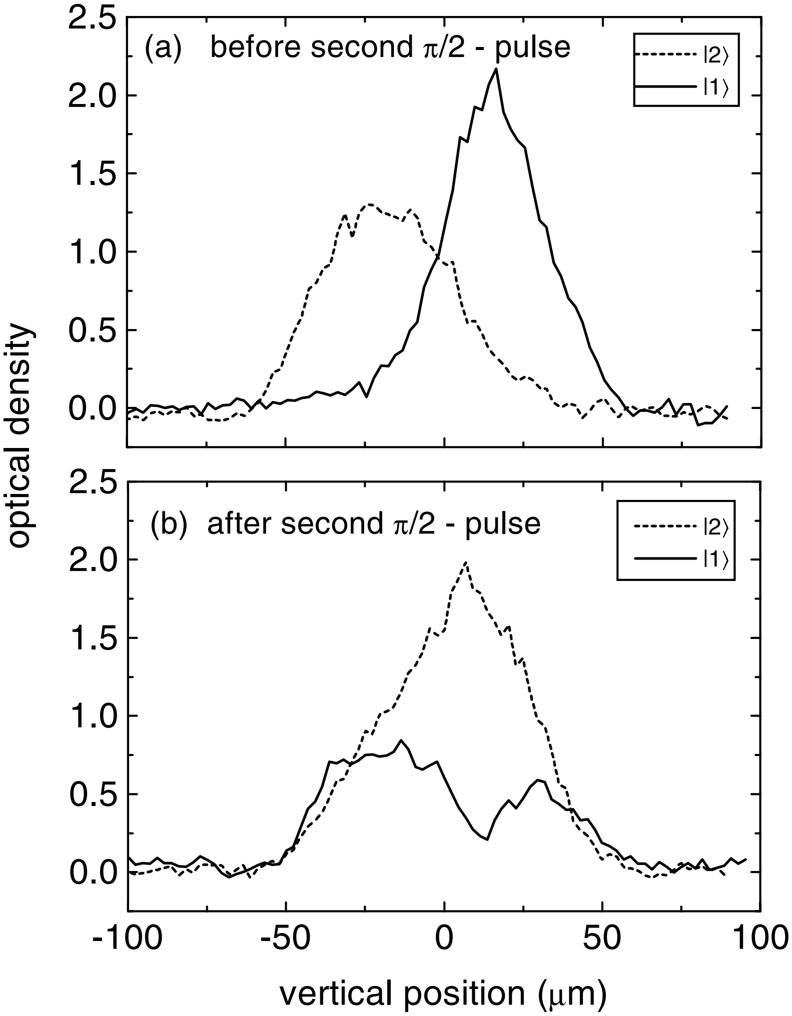

Figure 6.2: (a) The post-expansion density profiles of the condensates in the steady-state attained after a single $\frac{\pi}{2}$-pulse. These density profiles vary little from shot-to-shot (and day-to-day). (b) The density profiles after the second $\frac{\pi}{2}$-pulse. The density in the overlap region depends on the relative phase between the two condensates at the time of the pulse; in the case shown, we observe constructive interference in the $|2\rangle$ state and destructive interference in $|1\rangle$. The patterns in (b) are much less stable than those in (a), possibly as a result of unresolved higher-order condensate excitations, issues associated with the expansion, or technical instabilities of the apparatus.

The stable interference patterns show that the condensates retain a clear memory of their initial relative phase despite the complicated rearrangement dynamics of the two states following the first $\frac{\pi}{2}$-pulse. This is rather surprising, since the center-of-mass motion of the double condensate system is strongly (and completely) damped, and, in general, decoherence times in entangled states tend to be much shorter than damping times [48, 132, 44]. The intuition one develops in understanding few-particle quantum mechanics may not apply to experiments involving condensates. The phase between the two condensates seems to possess a robustness which preserves coherence in the face of the "phase-diffusing" couplings to the environment.

The oscillation pattern of Fig. 6.3 seems to wash out by 100 ms. The peaks and valleys still retain nearly the full contrast, but any given location in time will show a random phase relationship between the two condensates. This can be explained as a π variation in phase at 100 ms, implying a $2\pi \times 5$ Hz $\times\hbar$ variation in the relative energy of the two condensates. This is likely due to magnetic field fluctuations in instead of phase diffusion or decoherence from thermal atoms [71]. For the trap of 130 G/cm and a rotating field of 3.4 G, the field sensitivity of the two-photon transition is ~ 250 Hz/G, implying field fluctuations of 20 mG. A 10% variation in the quadrupole, and a 0.6% variation in the rotating field magnitude can explain this if the time scale is between ~ 100 ms and ~ 3 minutes . If it were faster than 100 ms it would average out, and if it were longer than 3 minutes, we would notice that successive shots where reproducible. Measurement indicate that a 10% variation of the quadrupole field is unreasonable, but the rotating field changes by 1 to 2 % on a time scale of ~ 200 ms. It is therefore very reasonable that our system has irreproducible phase from technical issues.

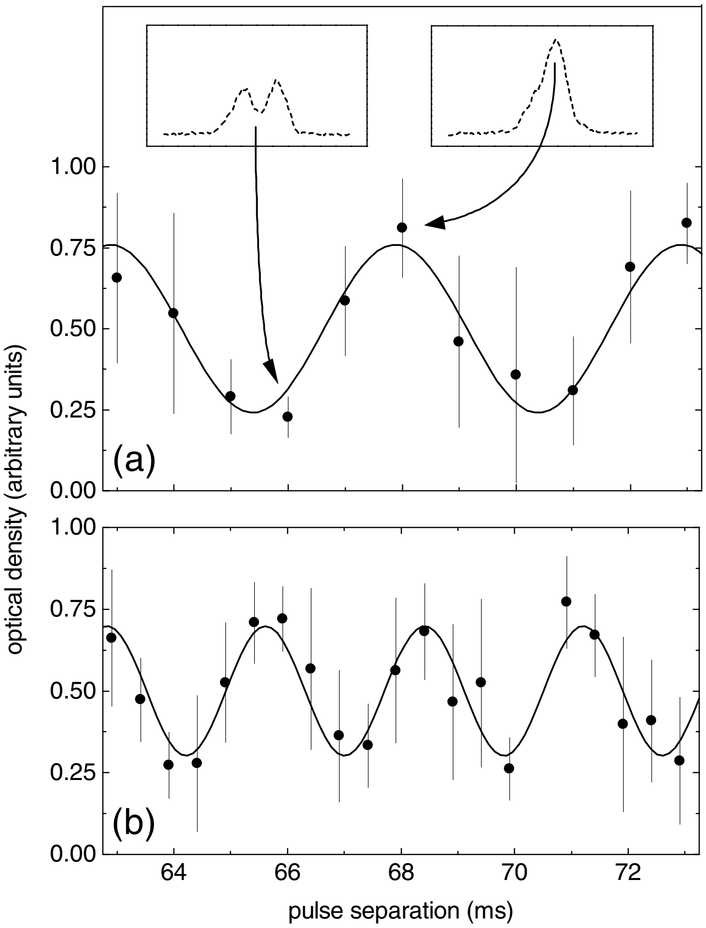

Figure 6.3: The value of the condensate density in the $|2\rangle$ state is extracted at the center of the overlap region (inset) and plotted (a) as a function of T. Each point represents the average of 6 separate realizations and the thin bars denote the rms scatter in the measured interference for an individual realization. The thick lines are sinusoidal fits to the data, from which we extract the angular frequency $\omega_{21} - \omega_{\rm rf}$. In (b), the frequency of the coupling drive $\omega_{\rm rf}$ has been increased by $2\pi \cdot 150$ Hz, leading to the expected reduction in fringe spacing.

Chapter 7

Unique phase patterns [4]

Quantization and persistence of current in superconductors and superfluids can be understood in terms of the topology of the order parameter. Current arises from a gradient in the phase of the order parameter. Quantization of flow around a closed path is a consequence of the requirement that the order parameter be single-valued; metastability, or "persistence", arises from the fact the number of phase windings (the multiple of 2π by which the phase changes) around the path can be changed only by forcing the amplitude of the order parameter to zero at some point. If the energy this requires exceeds that available from thermal excitations, then the current will be immune to viscous damping. This familiar argument relies, however, on the order parameter's belonging to a very simple rotation group. The order parameter in superfluid ^{4}He, for example, is a single complex number. Its phase can be thought of as a point lying somewhere on a circle, and is subject to the topological constraints mentioned above. The order parameter of a more complicated superfluid, on the other hand, will in general be capable of ridding itself of unwanted kinetic energy by moving continuously through a higher-dimensional order-parameter space in such a way as to reduce, even to zero, its winding number. Presumably this ability will reduce a superfluid's critical velocity; in the limit that the order-parameter space is fully symmetric, the critical velocity may even vanish [23].

7.1 Twisting the phase

Our experiments utilize a gas-phase Bose-Einstein condensate with two internal levels [24]. This is equivalent to a spin-1/2 fluid: the order parameter has SU(2) rotation properties. A differential torque across the sample is applied to the order parameter so that with time it becomes increasingly twisted. Eventually the sample distorts through SU(2) space so that the steadily applied torque now has the effect of untwisting the order parameter, which returns nearly to its unperturbed condition. The pattern of twisting and then untwisting is manifested experimentally as a washing-out followed by a recurrence of an extended series of oscillations in the population between the spin states. Related behavior has been previously observed in A-phase ^{3}He [111]; a major difference in this work is that we can directly observe components of the order parameter with temporal and spatial resolution.

Magnetically confined ^{87}Rb can exist in a superposition of the two internal states $|1\rangle$ and $|2\rangle$. The two internal states are separated by the relatively large ^{87}Rb hyperfine energy, but in the presence of a near-resonant coupling field the states appear, in the rotating frame, to be nearly degenerate. The condensate can then dynamically convert between internal states. The order parameter for the condensate is the pair of complex field amplitudes Φ_1 and Φ_2 of states $|1\rangle$ and $|2\rangle$. Evolution of these fields is governed by a pair of coupled Gross-Pitaevskii equations which model the coupling drive, the external confining potential, kinetic energy effects and mean-field interactions [50, 76, 57]. The SU(2) nature of the order parameter (Φ_1,Φ_2) is more evident if we write

$$\Phi_1 = \cos(\theta/2)e^{-i\phi/2}n_t^{1/2}e^{i\alpha} \tag{7.1}$$

and

$$\Phi_2 = \sin(\theta/2)e^{i\phi/2}n_t^{1/2}e^{i\alpha} \tag{7.2}$$

where θ, ϕ, n_t, and α are purely real functions of space and time. θ and ϕ give the relative amplitude and phase of the two internal components, and may be thought of respectively as the polar and azimuthal angles of a vector whose tip lies on a sphere in SU(2) space. The total density and mean phase, n_t and α respectively, remain relatively constant [75] during the condensate evolution described in this paper.

The starting point for the measurements is a magnetically confined cloud of $\sim 8 \times 10^5$ evaporatively cooled, Bose-Einstein-condensed ^{87}Rb atoms near zero temperature. The combined gravitational and magnetic potentials [114] yield an axially symmetric, harmonic confining potential V_1 (V_2) for particles in the $|1\rangle$ ($|2\rangle$) state, in which the aspect ratio of the axial oscillation frequency in the trap to the radial frequency ω_z/ω_r can be varied from 2.8 to 0.95 [61]. V_1 and V_2 are nearly identical but can optionally be spatially offset a distance z_0 in the axial direction (see Chapter 3). The coupling field has a detuning δ from the local $|1\rangle$ to $|2\rangle$ resonance. If z_0 is nonzero, δ depends on the axial position z, with $\delta(z) - \delta(z = 0)$ linear in z and in z_0. The strength, characterized by the Rabi frequency Ω, of the coupling field also varies with an axial gradient.

We are able to measure the population of both spin states nondestructively using phase-contrast microscopy [12, 38]. We tune the probe laser between the resonant optical frequencies for the $|1\rangle$ and $|2\rangle$ states. Since the probe detuning has opposite sign for the two states, the resulting phase shift imposed on the probe light has opposite sign, such that the $|1\rangle$ atoms appear white and the $|2\rangle$ atoms appear black against a gray background on the CCD array. We can acquire multiple, nondestructive images of the spatial distribution of the $|1\rangle$ and $|2\rangle$ atoms at various discrete moments in time, or we can acquire a quasi-continuous time record (streak image) of the difference of the populations in the $|1\rangle$ and $|2\rangle$ states, integrated across the spatial extent of the cloud.

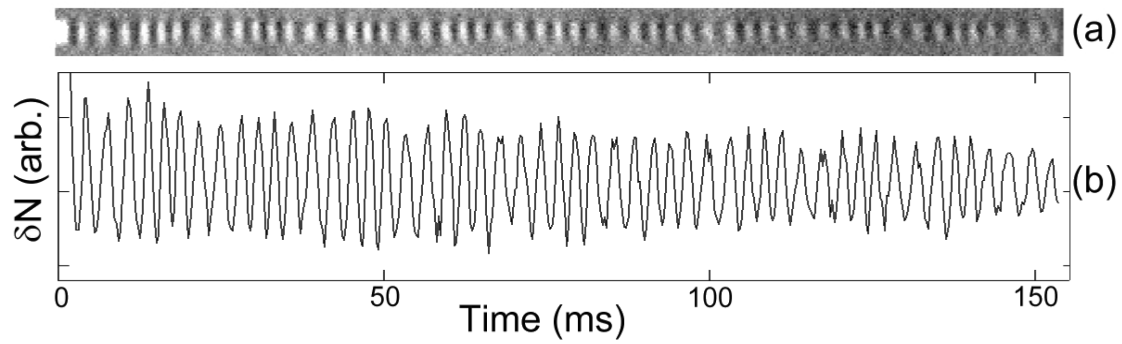

Figure 7.1: (a) With the trap parameters adjusted for high spatial uniformity in Ω_{eff}, we drive the coupling transition and record a streak-camera image of 60 Rabi oscillations between the $|1\rangle$ (white) and $|2\rangle$ (black) states. The vertical dimension of the figure is 80 μm. (b) The value of δN, the total number of atoms in $|2\rangle$ minus the total in $|1\rangle$, is extracted from the image in part (a). The contrast ratio remains near unity — observed loss of signal is due to overall shrinkage of the condensate through collisional decay.

The effect of the coupling drive is to induce a precession of the order parameter at the local effective Rabi frequency $\Omega_{\text{eff}}(z) \equiv (\Omega(z)^2 + \delta(z)^2)^{1/2}$. In a preliminary experiment, we chose parameters so as to make Ω_{eff} nearly uniform, with $\omega_z = 2\pi \times 63\text{Hz}$, $\omega_r = 2\pi \times 23$ Hz, $\Omega \simeq 2\pi \times 340$ Hz and $\delta(z) \simeq 0$. A condensate at near-zero temperature was prepared in the pure $|1\rangle$ state. The coupling drive was then turned on suddenly, inducing an extended series of oscillations of the total population from the $|1\rangle$ to the $|2\rangle$ state ("Rabi oscillations") [Fig. 7.1]. The robustness of the Rabi oscillations is proof that our imaging does not significantly perturb the quantum phase of the sample [25](population transfer via Rabi oscillations is phase-sensitive).

If there is an axial gradient to Ω_{eff}, then a relative torque is applied to the order parameter across the condensate, which can cause a twist to develop along the axial direction. If we naively model the sample as a collection of individual atoms, each held fixed at its respective location, then the order parameter at each point in space rotates independently at the local effective Rabi frequency, Ω_{eff}.

In Fig. 7.2(a) and Fig. 7.3we see the implications of the “fixed-atom” model for $\Omega = 2\pi \times 700$ Hz and $\delta(z) = 2\pi \times (100+14z)$Hz with z in microns: a twist develops in the order parameter which leads to a washing out of the Rabi oscillations [Fig. 7.2(c)]. In contrast, the kinetic energy provides stiffness for a true condensate. Simulation of the condensate [26] shows that, for early times, the order parameter begins twisting as in the “fixed-atom” model but the twisting process self-limits about 40 ms into the simulation. At this point there is nearly a full winding across the condensate. Thereafter, though the two ends of the order parameter continue to twist with respect to one another, the order parameter has been sufficiently wrapped around the SU(2) sphere that the effect of further torque is to return the condensate close to its unperturbed condition [Fig. 7.2(d)]. The Rabi oscillations exhibit a corresponding revival [Fig. 7.2(e)]. The factor driving the untwisting process is the increasing kinetic energy cost associated with an increasing twist in the order parameter. For a simple U(1) order parameter, continuously increasing the winding ultimately results in a “snap”, in which the order parameter is driven to zero and a discontinuous (and presumably dissipative [27]) process releases the excess windings. The revival in the present case is made possible by the larger rotation space available to a two-component cloud.

Under experimental conditions similar to those of the simulations in Fig. 7.2, we have observed as many as three complete cycles of Rabi-oscillation decay and recurrence. These data appear in Ref. [133]. In this paper we present data that correspond to the case of a more vigorous twisting. We increase the axial dimension of the condensate cloud by a factor of four; the kinetic energy cost of twisting the condensate is correspondingly lower, so that at the point in time when the condensate is maximally distorted there are four windings across the cloud. The parameters of the experiment were as follows: $\omega_r = \omega_z = 2\pi \times 7.8$ Hz and mean $\Omega_{\text{eff}} = 2\pi \times 225$Hz. There was a gradient in both δ and Ω across the

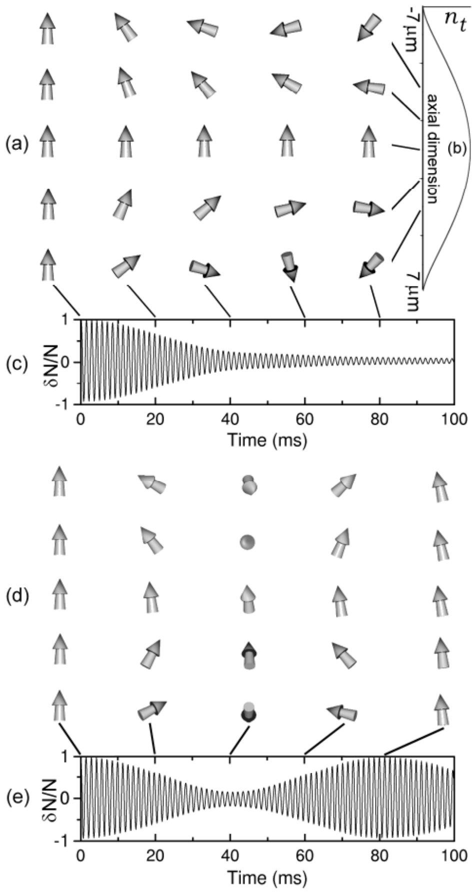

Figure 7.2: (a) We represent the polar-vector order parameter as an arrow in these simulations. The angle θ from the vertical axis determines the relative population, and the azimuthal angle ϕ is the relative phase of states $|1\rangle$ and $|2\rangle$ (see Eqs. 1). Each column in the arrow-array is at fixed time, and each row at fixed axial location. $\hat{\Omega}$ is perpendicular to the plane of the page, so that a uniform, on-resonance Rabi oscillation would correspond to all the arrows rotating in unison, in the plane of the image. The tips of all the arrows are (on the relatively fast time scale of Ω_{eff}) tracing out circles nearly parallel to the plane of the page (in our rotating-frame representation, small excursions out of the page are a consequence of finite detuning). In the figures, we "strobe" the motion just as the central arrow approaches vertical, to emphasize the more slowly evolving "textural" behavior. (b) The total density of the condensate n_t maintains a Thomas-Fermi distribution (integrated through one dimension, as imaged) and changes only slightly during the evolution of the cloud. (c) In a simple model of individual, fixed atoms, a continuous inhomogeneity in Ω_{eff} will cause the Rabi oscillations in δN to wash out. (d) When a condensate is simulated [19], the kinetic energy causes the order parameter to precess through the full SU(2) space, coming out of the page to cast off the winding and thus reduce its kinetic energy. (e) The corresponding plot of δN shows that when the arrows are once more aligned, the Rabi oscillations recur.

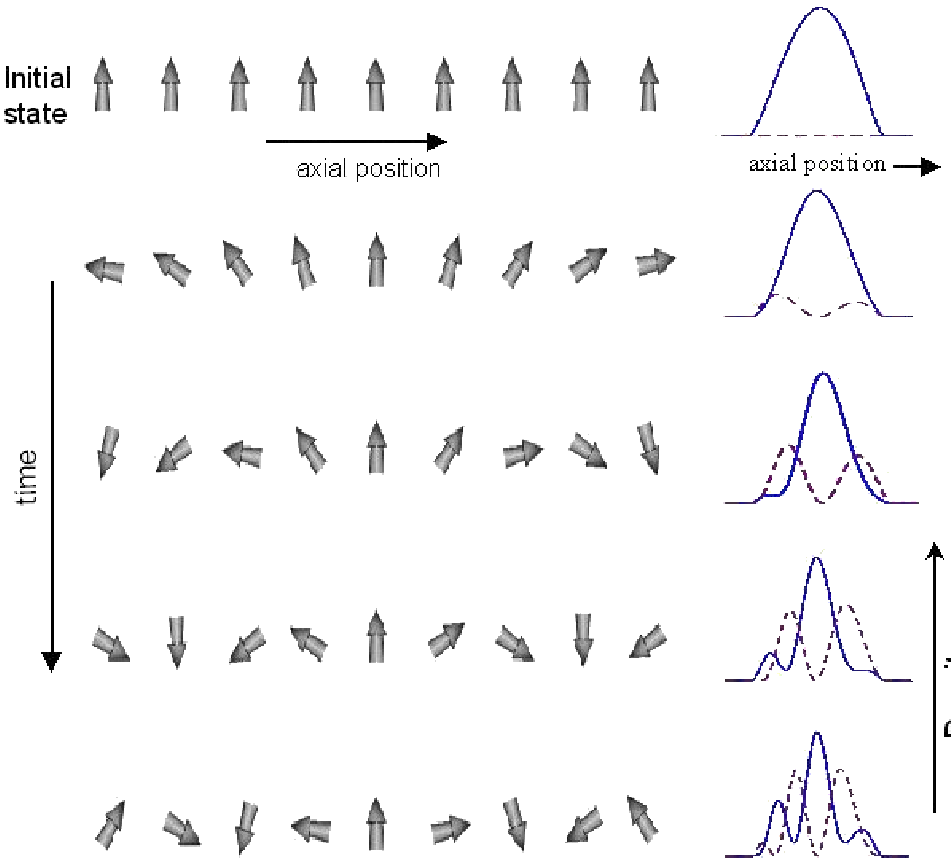

Figure 7.3: Note this schematic is rotated with respect to the previous. This model is similar to Fig. 7.2a, with density plots included. Solid lines represent the $|1,-1\rangle$ density cross section and dashed lines are the $|2,1\rangle$ density (of course, one Rabi period later they switch). Individual atoms are treated as discrete two level systems each with a different along the axial position. The detuning causes a gradient in effective Rabi frequency which means the population transfer slowly accumulates differences across the cloud. This is manifested as increasingly fine structure on the modeled density profile.

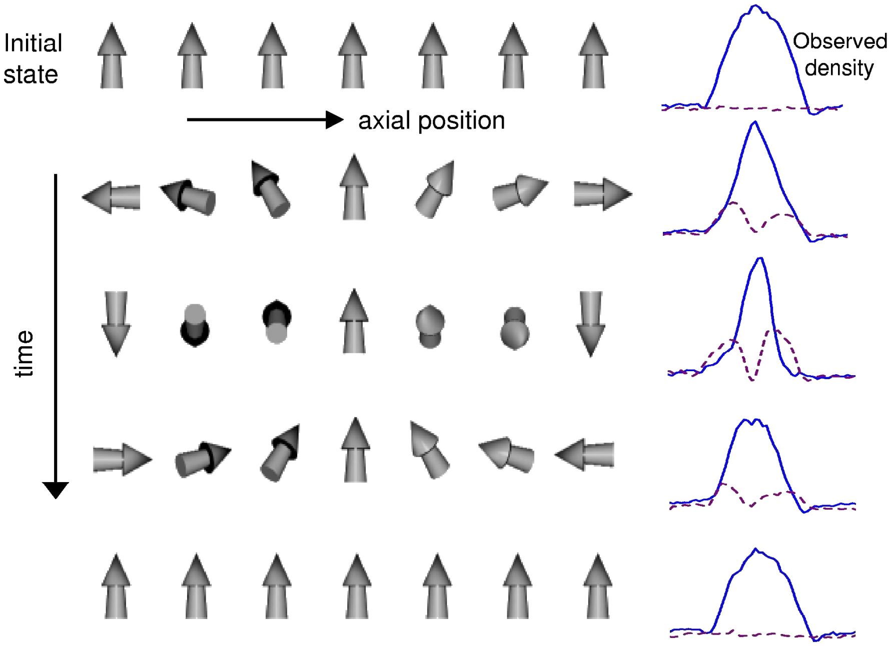

Figure 7.4: The actual density behaves quite differently than the model in Fig. 7.3 suggests. Initially the phase winds up similar to the no-kinetic energy model. After time, the phase begins to unwind on its own, appearing to retrace its steps to find the original density distribution. The arrows are only a qualitative model suggested by the density evolution, but are very similar to the simulation in Fig. 7.2d.

$54\mu m$ axial extent of the cloud, resulting in a $\sim 2\pi \times 60$Hz difference in Ω_{eff} from top to bottom of the condensate. The result of the experiment is seen in Fig. 7.5. The observed recurrence of the Rabi oscillations at 180 ms [Fig. 7.5(a)], when corrected for overall decay of the cloud, corresponds to 60 percent contrast. We find it remarkable that the distorted order-parameter field seen in Fig. 7.5(b) at times 65 and 75 ms should find its own way back to a nearly uniform configuration.

The simulations qualitatively reproduce the integrated number and state-specific density distributions observed in the experiments. For large inhomogeneity in Ω_{eff}, however, the simulations predict the development of small-scale spatial structure not observed in the experiment. The simulations contain no dissipation, whereas finite-temperature damping may occur in the experiment [28].

Heuristically, what value do we expect for the recurrence time t_{recur} for the data in Fig. 7.5? The difference in Ω_{eff} from the top to the bottom of the condensate is about 60 Hz. From the data in Fig. 7.5(b) we see that the recurrence occurs only after four windings have one-by-one been twisted in and then twisted out of the condensate. A rough estimate then would be $t_{\text{recur}} = (4+4)/60\text{Hz}= 133$ ms, shorter than the observed value of 180 ms, but reasonable given that edge effects have been neglected. This scaling is born out in Fig. 7.7, aside from an offset in the rf detuning, which has not yet been understood.

An interesting theoretical challenge would be to develop simple arguments that would allow an *a priori* prediction of the spacing of the windings at the instant of maximum twist. For particularly strong torques, one might expect the total density to be suppressed to zero along a plane transverse through the cloud, so as to allow for discontinuous relaxation of the order parameter. Indeed we have seen such behavior in numerical simulations. Under what conditions should suppression of total density, rather than continuous evolution through SU(2) space, be the

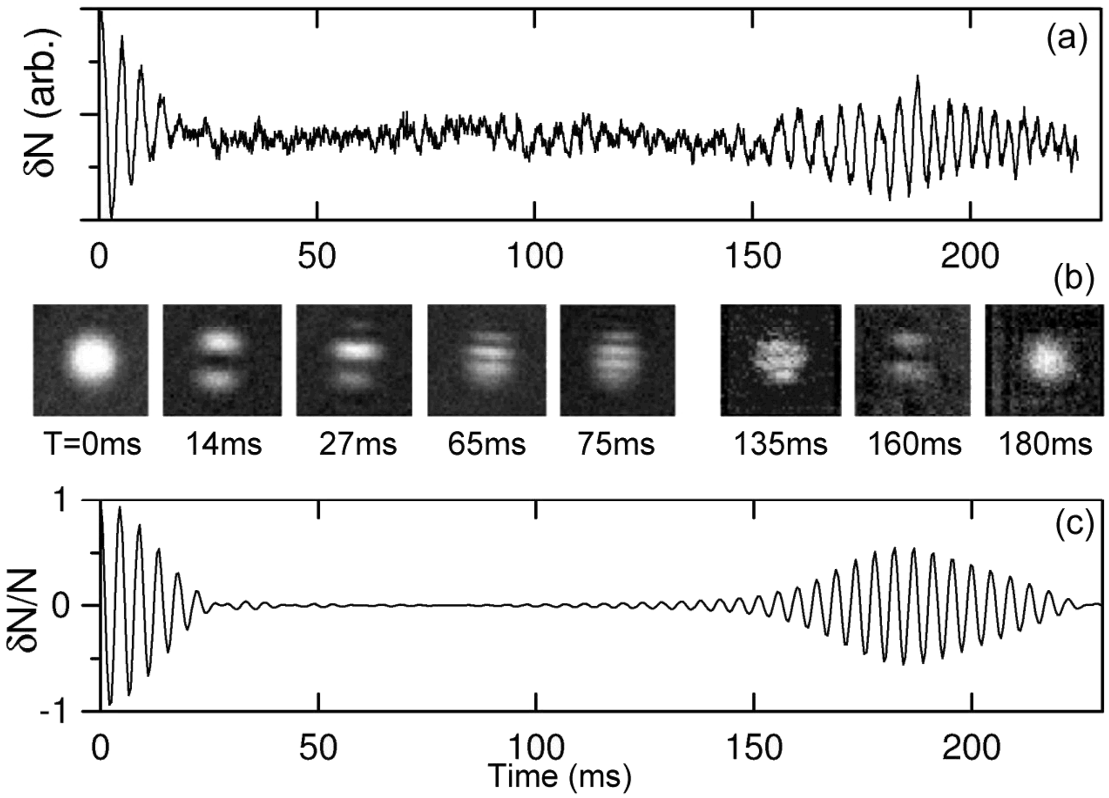

Figure 7.5: A condensate with large axial extent undergoes twisting. (a) The streak camera data shows a rapid decay in the Rabi oscillation in the integrated population difference, from full contrast at t=0 to near zero by $t = 20$ms. The oscillations recur at 180 ms. (b) Individual phase-contrast images (at distinct moments in time) of the spatial distribution of $|1\rangle$-state atoms show that the spatially inhomogeneous Rabi frequency is twisting the order parameter, cranking successively more windings into the condensate until by $\sim$ 75 ms four distinct windings are visible. Further evolution results not in more but in fewer windings until, at time 180 ms, the order parameter is once more uniform across the cloud. Each image block is 100 μm on a side, and the probe laser is tuned much closer to the $|1\rangle$ state than to the $|2\rangle$ state. (c) The numerical simulation reproduces the qualitative features of the corresponding experimental plot (a). The simulation used $\delta(z) = 0$, $\Omega(z = 0) = 2\pi \times 225$Hz and a $2\pi \times 60$Hz spread in Ω across the extent of the condensate.

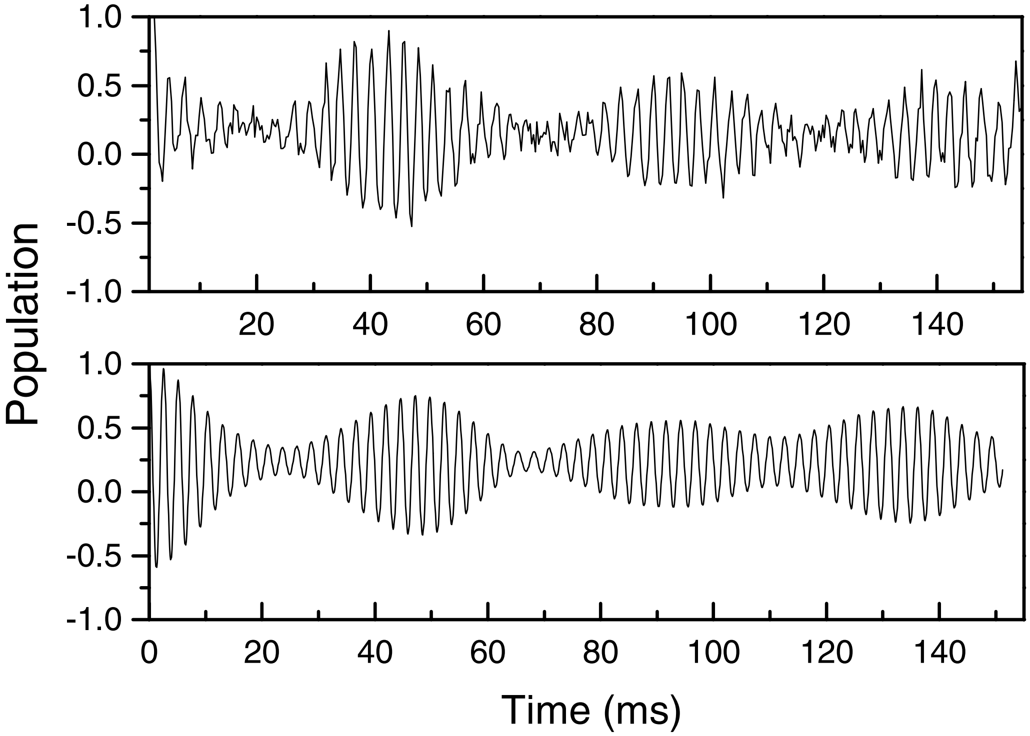

Figure 7.6: Experiment (top) and theory (bottom) for a condensate undergoing Rabi oscillations between the two spin states, with a gradient in the two-photon drive detuning. The overall detuning of the two-photon drive from resonance is 80 Hz red. The gradient is determined by the 0.4 μm offset between the traps of frequency 62 Hz in the axial direction.

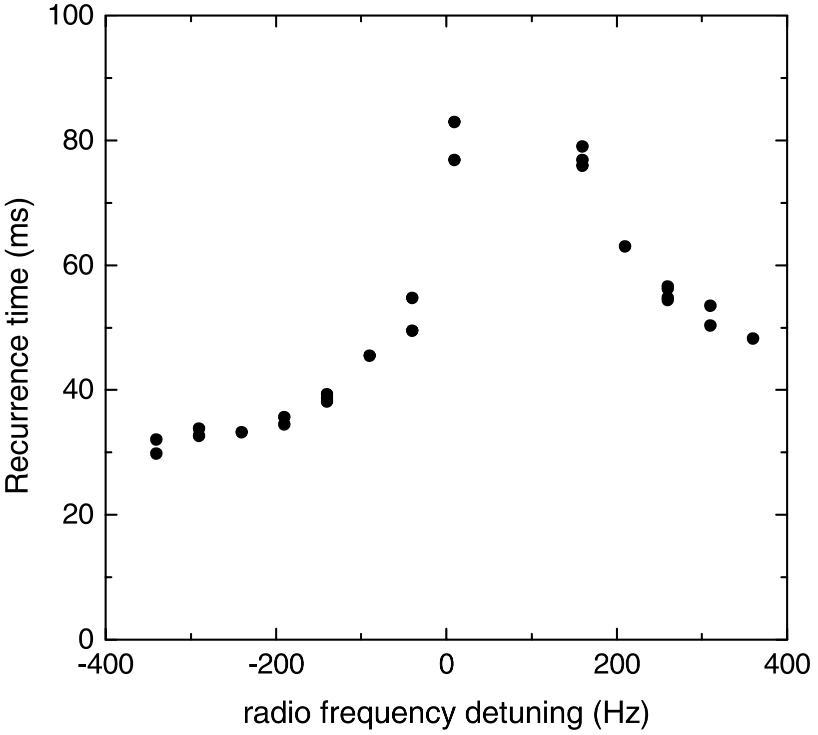

Figure 7.7: The time for the first recurrence of the Rabi oscillations as a function of detuning. This data was for a 62 Hz (axial) trap with a bare Rabi frequency of 370 Hz.

preferred mode of relieving accumulated stress?

7.2 Dressed states

We have observed that the presence of the coupling drive need not result in population oscillations. For any given frequency and coupling strength, there are two steady-state solutions which are completely analogous to the dressed-states solutions of the single-atom problem [29]. The lower and upper dressed states for a single atom ($|a\rangle$ and $|b\rangle$ respectively) are

$$\begin{aligned} |a\rangle &= \frac{1}{\sqrt{2}}\sqrt{1+\frac{\Delta(z)}{\Omega_e(z)}}\,|1,-1\rangle - \frac{1}{\sqrt{2}}\sqrt{1-\frac{\Delta(z)}{\Omega_e(z)}}\,|2,1\rangle\,, \\ |b\rangle &= \frac{1}{\sqrt{2}}\sqrt{1-\frac{\Delta(z)}{\Omega_e(z)}}\,|1,-1\rangle + \frac{1}{\sqrt{2}}\sqrt{1+\frac{\Delta(z)}{\Omega_e(z)}}\,|2,1\rangle\,, \end{aligned} \tag{7.3}$$

where $\Delta(z)$ is the detuning from resonance, and $\Omega_e(z) = \sqrt{\Delta(z)^2 + \Omega(z)^2}$ is the effective Rabi frequency. The population in these states is independent of time. These are the true, local dressed states for our double condensate system if mean field is taken into account in the terms $\Delta(z)$ and $\Omega_e(z)$ (for times short compared to the time for density evolution to occur).

We have been able experimentally to put the condensate in such states via an adiabatic process: the strength of the drive is increased gradually from zero, and the frequency (initially far detuned) is gradually ramped onto resonance. The fraction transferred to the $|2,1\rangle$ is determined by

$$\begin{gathered} 1 - e^{-2\pi\Gamma} \\ \text{where } \Gamma = \frac{\pi\Omega^2}{2}\frac{1}{\partial\nu/\partial\mathrm{t}} \end{gathered} \tag{7.4}$$

for the rate of frequency ramp $\partial\nu/\partial t$. Our frequency ramp speed is such that the transfer is $> 95\%$ for a ramp completely through resonance. This ramp corresponds to adiabatic rapid passage transfer. If the ramp is halted on resonance

($\Delta = 0$), the condensate is in the lower dressed state $|a\rangle$. This resulting "dressed condensate" is extremely stable— after the ramp is complete, the cloud remains motionless in a near-equal superposition of the two bare states. Figure 7.8 shows the population in the $|2, 1\rangle$ state as a function of time.

After a pure dressed state is created, the drive amplitude may be turned down slowly so that the condensate moves adiabatically from the dressed state to the spin states. Since the two spins sit in slightly offset traps, the spin states begin to separate. In the limit that the drive strength goes to zero, the ground state of the double condensate system is produced. This ground-state mixture of the two spin states no longer has a fixed phase relationship since the drive is turned off – it is equivalent to the condensate mixture that would be formed if both states were simultaneously evaporated into condensation. The density distributions of the spin states for two different drives are shown in Fig. 7.9.

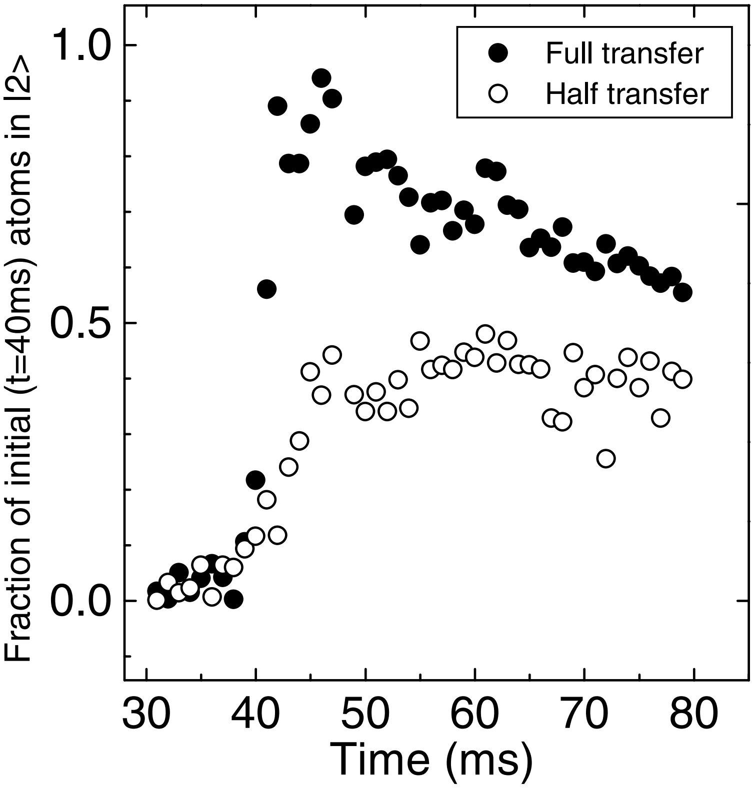

Figure 7.8: The drive frequency is ramped from 10kHz below to near resonance in 40 ms. The two curves show data for a ramp to resonance resulting in 100% transfer, and a ramp to on resonance resulting in 50% transfer. The decay after 40 ms is the loss due to spin exchange of $|2, 1\rangle$ atoms.

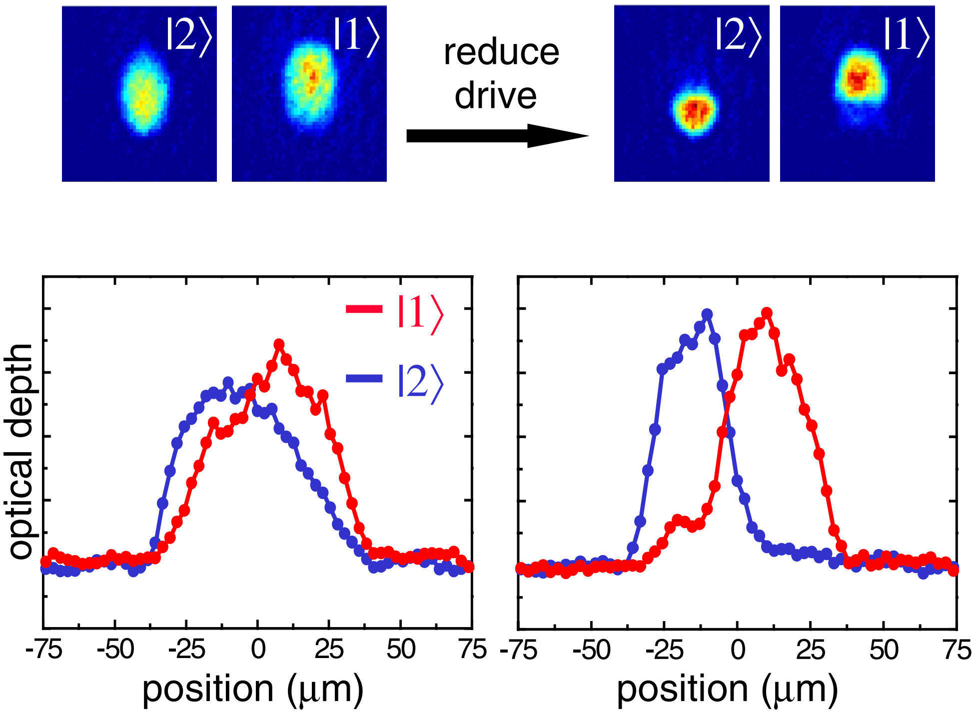

Figure 7.9: Density profiles of dressed condensates, for two values of the drive power. As the drive is reduced, the dressed state becomes an equal mixture of the spin states.

Chapter 8

Vortex creation [5]

The ability to fundamentally alter the topological properties of a condensate has already proven useful. When the coupling drive is turned off, the SU(2) properties vanish, and states $|1\rangle$ and $|2\rangle$ become distinct species, each forced to live in its separate U(1) space. Figure 7.5 illustrates how this can be used to change $\Phi_1(z)$ in a controlled manner. With a variation on this technique we have created a vortex-state condensate.

The concept of a vortex is at the center of our understanding of superfluidity. A vortex is a topological feature of a superfluid – in a closed path around the vortex, the phase undergoes a 2π winding and the superfluid flow is quantized. Following the experimental realization of a dilute atomic Bose-Einstein condensate (BEC) [30], much theoretical effort has been directed towards the formation and behavior of vortices in atomic BEC [31, 32, 120]. This chapter presents the experimental realization and imaging of a vortex in BEC. We use the method proposed by Williams and Holland [6] to create vortices in a two-component BEC. An interference technique is used to obtain phase images of the vortex state and confirm the 2π phase winding required by the quantization condition. We have also carried out preliminary studies of the stability of the vortices.

Vortices are created in superfluid helium by cooling a rotating bucket of helium through the superfluid transition, and a vortex forms for each unit of angular momentum. This does not work for BEC because it is formed in a harmonic magnetic trap. When the condensate first forms it occupies a tiny cross-sectional area at the center of the trap and is too small to support a vortex. Eventually, the condensate grows to sufficient size that it can support vortices, but the time scale for vortices to be generated in the vortex-free condensate due to coupling with the rotating environment is unknown, and may well be longer than the lifetime of the condensate. This is the potential difficulty with using an optical "stirring beam" or magnetic field distortion to rotate the cloud during condensation, as has been frequently proposed. Another proposal has been to use optical beams with appropriate topologies to "imprint" a phase on an existing condensate. This technique must drive the local density to zero at some point and then rely on uncertain dissipative processes for the condensate to relax into a vortex state.

We have avoided these uncertainties by creating vortices using a coherent process that directly forms the desired vortex wave function via transitions between two internal spin states of ^{87}Rb. The two spin states, henceforth $|1\rangle$ and $|2\rangle$, are separated by the ground-state hyperfine splitting and can be simultaneously confined in identical and fully overlapping magnetic trap potentials. A two-photon microwave field induces transitions between the states. As we have seen in previous experiments, this coupled two-component condensate is exempt from the topological rules governing single-component superfluids - rules that make it difficult to implant a vortex within an existing condensate in a controlled manner. In the coupled system, we can directly create a $|2\rangle$ (or $|1\rangle$) state wave function having a wide variety of shapes [6] out of a $|1\rangle$ (or $|2\rangle$) ground-state wave function by controlling the spatial and temporal dependence of the microwave-induced conversion of $|1\rangle$ into $|2\rangle$.

We control the conversion by shifting the transition frequency using the AC Stark effect. A spatially inhomogeneous and moveable optical field (a focused laser beam) provides the desired spatial and temporal control of the AC Stark shift. The vortex state is an axially symmetric ring with a 2π phase winding around the vortex core where the local density is zero. To create a wave function with this spatial symmetry, the laser beam is rotated around the initial condensate as in Fig. 8.1a. The desired spatial phase dependence is obtained by detuning the microwave frequency from the transition, and rotating the laser beam at the appropriate frequency ω to make the coupling resonant. For large microwave detunings δ, the necessary rotation frequency is simply δ. For smaller detunings, the rotation frequency must be the effective Rabi frequency of the microwave transition [33]. As shown in Fig. 8.1b for large detunings, the energy resonance condition now means that atoms can only change internal state through the coupling of the time-varying perturbation, and are therefore obliged to obey any selection rule that the spatial symmetry of that perturbation might impose. The center of the condensate (at the axis of the beam rotation) feels no time-varying change, while regions near the circumference of the condensate feel a near-sinusoidal variation, with a phase delay equal to the azimuthal angle θ around the circumference of the cloud. Williams and Holland show that this is precisely the geometry best suited to couple the condensate into a vortex state. It should be emphasized that it is not simply the mechanical forces of the optical field that excite the vortex: a laser beam rotating clockwise can produce clockwise or counterclockwise vortex circulation, depending on the sign of the microwave detuning.

In the absence of the microwave coupling field, the two states can be thought of as two distinguishable, interpenetrating superfluids that interact with each other and with themselves via a mean-field repulsion proportional to the local densities. The interaction coefficients differ slightly [105, 46], so the $|1\rangle$ fluid has slight positive buoyancy with respect to the $|2\rangle$ fluid [75]. When the $|1\rangle$ fluid has a net angular momentum, it forms an equatorial ring around the central $|2\rangle$

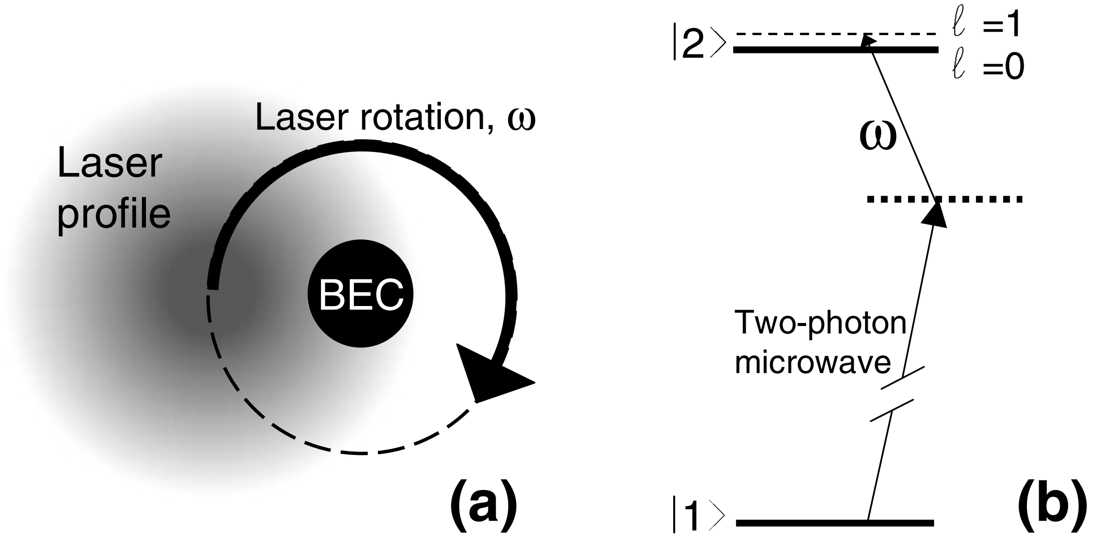

Figure 8.1: (a) A basic schematic of the technique used to create a vortex. An off-resonant laser provides a rotating gradient in the AC Stark shift across the condensate as a microwave drive of detuning δ is applied. (b) A level diagram showing the microwave transition to very near the $|2\rangle$ state, and the modulation due to the laser rotation frequency that couples only to the angular momentum $l = 1$ state when $\omega = \delta$. In the figure, the energy splitting (< 1 Hz) between the $l = 1$ and $l = 0$ states is exaggerated.

fluid. The $|1\rangle$ fluid partially penetrates the constant-phase $|2\rangle$ fluid, which creates a central potential barrier. Conversely, a $|2\rangle$ vortex forms a ring that tends to contract down into the $|1\rangle$ fluid. We use the overlap of the $|1\rangle$ and $|2\rangle$ fluids to image the phase profile of the vortex state via the interconversion interference technique that we introduced in [76]. In the presence of a near-resonant microwave field (and no perturbing optical field), the two states interconvert at a rate sensitive to the local difference in the quantum phases of the two states. Thus the application of a resonant $\pi/2$ microwave pulse transforms the original two-fluid density distribution into a distribution that reflects the local phase difference, a "phase interferogram." Looking at the condensate both before and after the interconversion pulse provides images of both the amplitude and phase of the vortex ring.

The basic experimental setup for forming condensates and driving them between different spin states is the same as in [105]. Using laser cooling and trapping, followed by trapping in a TOP magnetic trap and evaporative cooling, we produce a condensate of typically $\sim 8 \times 10^5$ atoms in the $|1\rangle$ state ($F = 1$, $m_F = -1$). We then adiabaticaly convert the trap to a spherically symmetric potential by reducing the quadrupole magnetic field gradient [61]. This leaves us with a condensate 54 microns in diameter in a trap with oscillation frequencies of 7.8 ±0.1 Hz in the radial and axial directions for both spin states. In this trap, a $|1\rangle$ state condensate has a lifetime of 75 s and the $|2\rangle$ state ($F = 2$, $m_F = +1$) about 1 s. Oscillating magnetic fields can then be pulsed on to drive the microwave transition between the $|1\rangle$ and $|2\rangle$ states. The power and oscillation frequency of the fields are adjusted to obtain the desired effective Rabi frequency for the $|1\rangle$ to $|2\rangle$ transition. To create a vortex in $|2\rangle$ we add a 10 nW, 780 nm laser beam that has a waist of 180 μm and is detuned 0.8 GHz blue of resonant excitation of the $|2\rangle$ state. Using piezoelectric actuators we rotate the beam in a $\sim$75 μm radius circle around the condensate at 100 Hz. The following procedure is used to obtain the precise location of the laser beam that is required to create a vortex. We first set the effective Rabi frequency to 100 Hz by adjusting the detuning of the microwave frequency away from resonance in the presence of the light. Typically the resonant Rabi frequency is 35 Hz and the total detuning about 94 Hz from the $|1\rangle$ to $|2\rangle$ transition. By making fine adjustments of the detuning we then optimize the amount of transfer (typically 50%) to the $|2\rangle$ state, as shown in Fig. 8.2. We then adjust the center of rotation of the beam to obtain the most symmetric rings. After ~ 70 ms the vortex has been formed, and we turn off the laser beam and the microwave drive.

We can take multiple images of a vortex both during and after formation using nondestructive state-selective phase contrast imaging [38]. Rapid control of the microwave power and frequency allows us to apply various pulse sequences to explore many different options for the creation, manipulation, and observation of a single vortex. For example, we can put the initial condensate into either the $|1\rangle$ or $|2\rangle$ state and then make a vortex in the $|2\rangle$ or $|1\rangle$ state respectively, and we can obtain phase interferograms or quickly switch the internal state of the vortex at any time after the rotating laser beam is off. We can also watch the evolution of the vortex over time scales from milliseconds to seconds. All of these techniques are nondestructive to both the density and phase.

In Fig. 8.3 we show a detailed picture of the phase profile of a $|2\rangle$vortex. To obtain this we first take a picture of the vortex (Fig. 8.3a), then we apply a resonant microwave π-pulse. Half-way through the 4 ms long π-pulse, we take a second image (Fig. 8.3b), and at the completion of the pulse we take a third image (Fig. 8.3c) that shows the original density distribution of the interior $|1\rangle$ state. Normalizing by the density distributions of the vortex and interior states we obtain the phase image in Fig. 8.3d [34]. The figure dramatically shows the variation

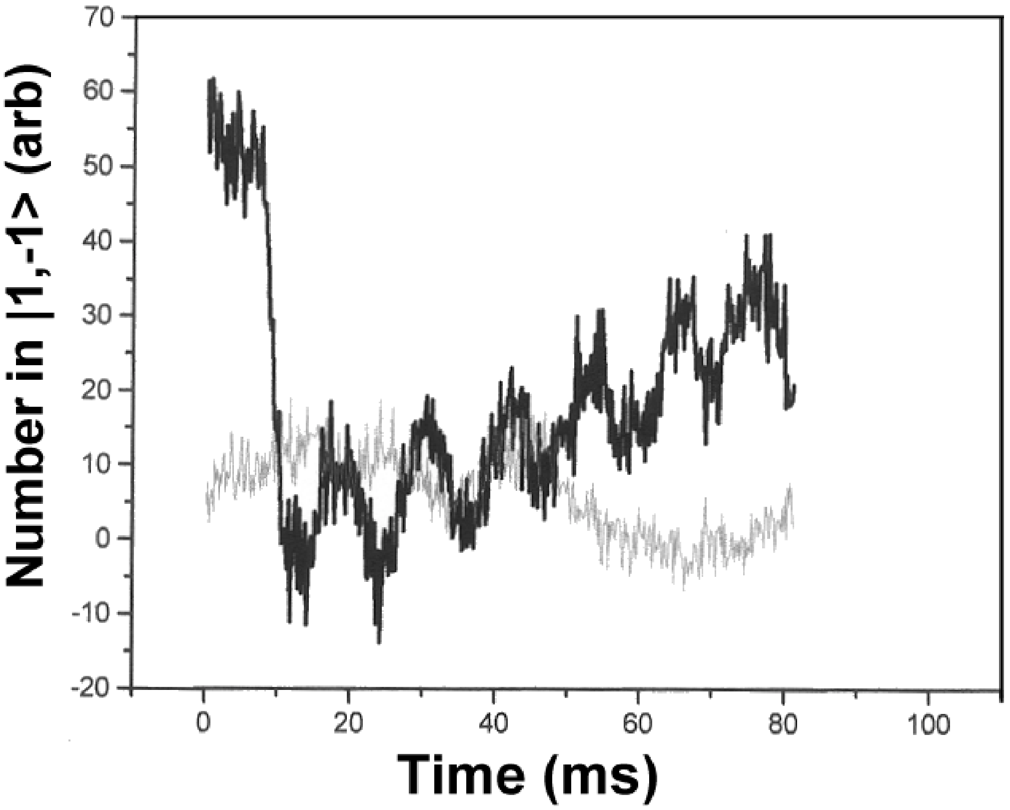

Figure 8.2: Atoms transferred into the $|1,-1\rangle$ state due to the vortex drive. This is slightly different than described in the text. We start with a $|1,-1\rangle$ condensate. Just before $t = 10$ ms we apply a π-pulse to convert the condensate into $|2,1\rangle$. Then at 10 ms the vortex drive is turned on to create a vortex in the $|1,-1\rangle$ state. The gradual increase in $|1,-1\rangle$ population (dark line) is a signature of successful coupling to this unique resonance. The grey line is the background.

and continuity of the phase around the ring (Fig. 8.3e) that are required by the quantization of angular momentum. As a check, we have taken the same type of phase pictures for our "ball and shell" density arrangement which occurs for a simple mixture of the two states. This is shown in Fig. 8.4. The density pictures (top and bottom) show similar structures to our vortex pictures. However the interference picture shows only symmetric structure, indicated there is no relative phase accumulation around the condensate.

In Fig. 8.5 are pictures of the time evolution of vortices to show their dynamics and stability. As expected, the dynamics of the $|1\rangle$ state vortices (Fig. 8.5a and Fig. 8.5b) are different from the $|2\rangle$ state vortices (Fig. 8.5c) due to the different scattering lengths. The $|2\rangle$ vortex ring sinks in toward the trap center (Fig. 8.5c), and then rebounds and apparently breaks up. This pattern is repeatedly observed in measurements of the $|2\rangle$ vortices. Conversely, the equilibrium position of a $|1\rangle$ state fluid is obtained by "floating" outside the $|2\rangle$ state fluid. The inner radius of the $|1\rangle$ state ring shrinks slowly as the interior $|2\rangle$ fluid decays away with a ~ 1 s lifetime. A variety of additional behaviors has been seen for $|1\rangle$ vortices. Initial asymmetry is very sensitive to beam position and condensate slosh. For small differences in the initial vortex state density distribution, asymmetric density distributions sometimes develop and/or "heal" between 0.5 and 1 s.

The nonrotating $|2\rangle$ fluid within a $|1\rangle$ vortex is analogous to the defects that pin vortices in superconductors. This $|2\rangle$ "defect" can be removed quickly, by a properly tuned laser pulse, or allowed to decay slowly (as in Figs. 8.5a and 8.5b). Thus this system can be varied between two relevant physical limits. In the limit of a large repulsive central potential (produced by a large amount of $|2\rangle$ fluid) the system most closely resembles quantized flow in a fixed, 3-D toroidal potential. The vortex core is pinned and its size is determined by the central

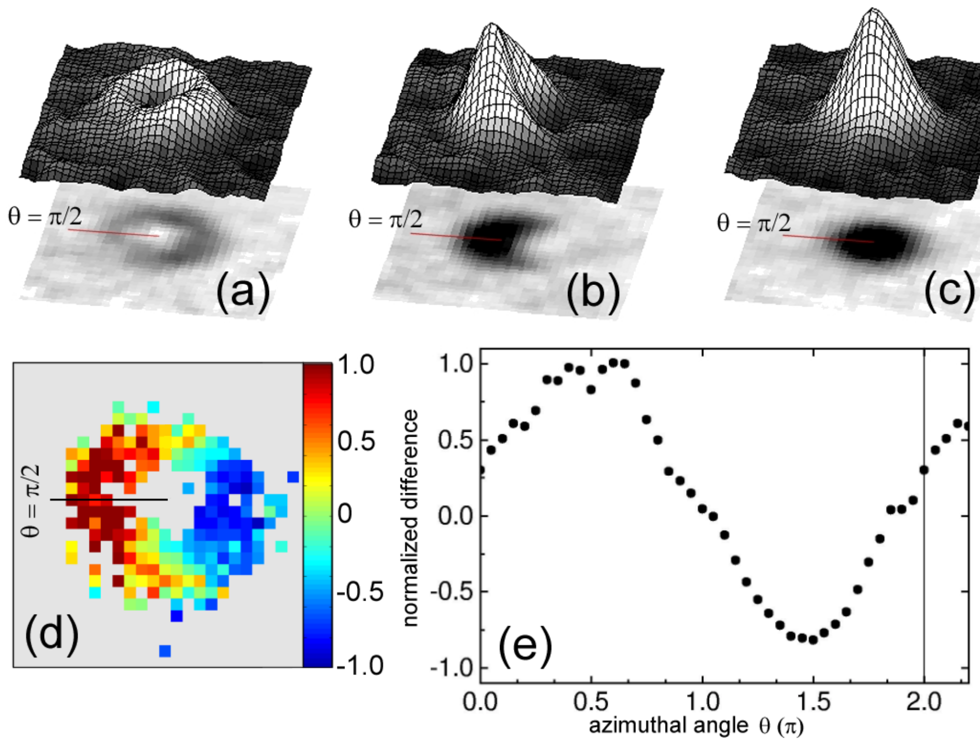

Figure 8.3: Condensate images (100 μm on a side) in which the imaging laser is tuned such that only $|2\rangle$ is visible. (a) The intial image of the vortex, (b) after $\pi/2$ of the interconversion pulse, and (c) after completion of the π-pulse. The vortex is now invisible (in $|1\rangle$) and the interior fluid is imaged (in $|2\rangle$). (d) The normalized difference in densities between the local average ring and interior densities ((a) and (c) respectively) and the phase interferogram density (b) for each corresponding point in the images. This is approximately the cosine of the local phase difference ϕ between the vortex state and the interior state [34]. The values are shown only for those regions where the densities of each state were high enough to give adequate signal to noise for the phase reconstruction. (e) The radial average at each angle θ around the ring is shown in (d). (The data is repeated after the azimuthal angle 2π to better show the continuity around the ring.)

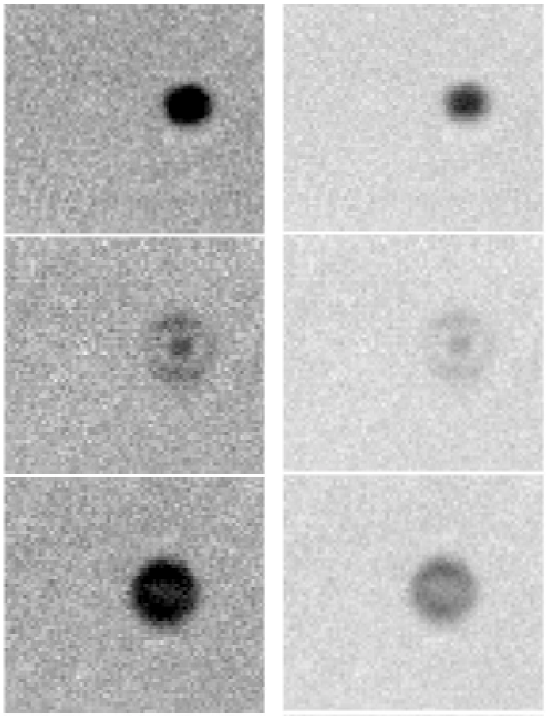

Figure 8.4: Condensate images for a 50-50 mixture of the $|1,-1\rangle$ and $|2,1\rangle$ states, produced by a simple $\pi/2$ pulse. Each vertical strip is the same data, but scaled differently to show specific features. Time is in the vertical direction. The first image is that of the $|2,1\rangle$ "ball", just before a π-pulse is applied. The second image is after $\pi/2$ of the π-pulse, which shows the interference between the two states. The third image is after the π-pulse is complete and shows the $|1,-1\rangle$ "shell".

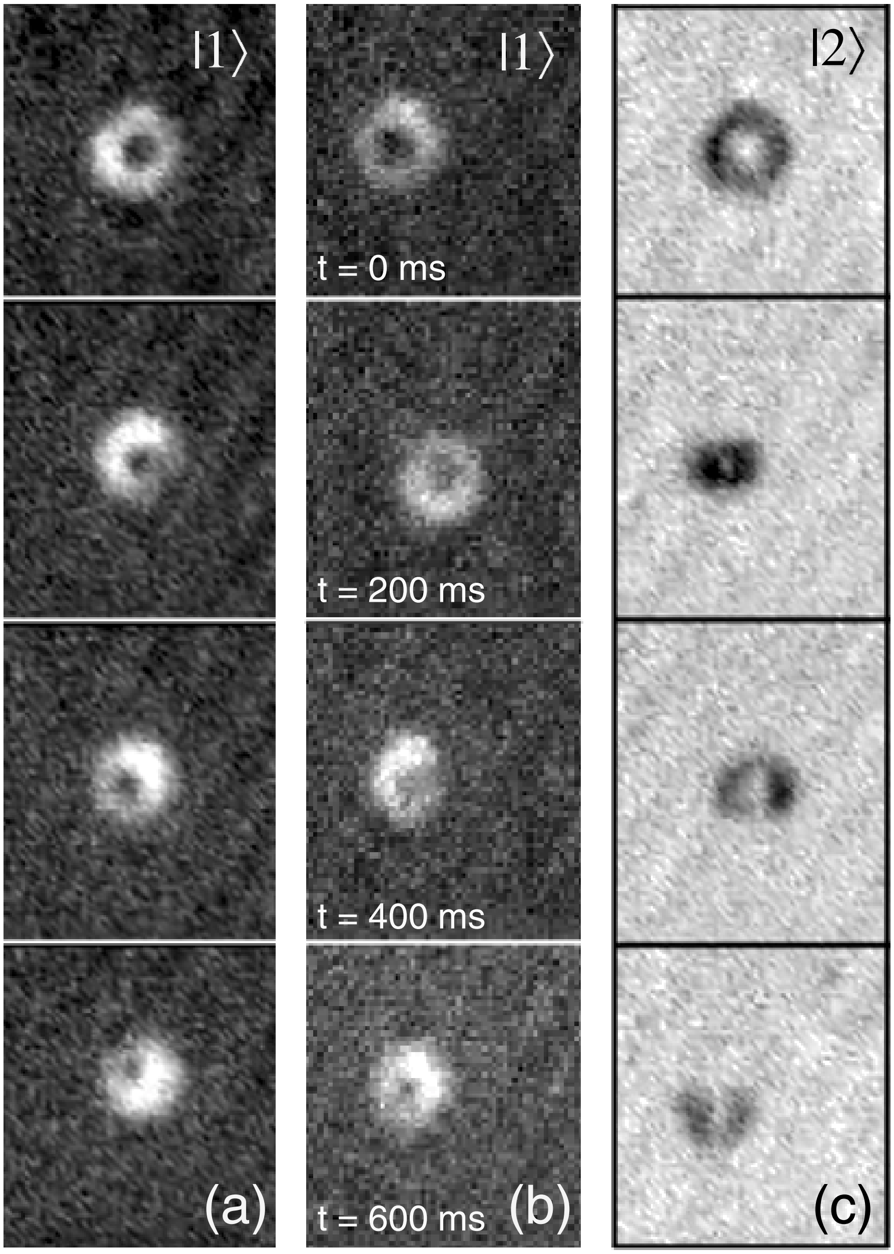

Figure 8.5: (a,b) Two separate instances of the free evolution of a $|1\rangle$ state vortex in the magnetic trap. It is stable over a time long compared to the trap oscillation period (128 ms). (c) The free evolution of a $|2\rangle$ vortex is much more dynamic. It is seen shrinking quickly into the invisible $|1\rangle$ fluid and rebounding into fragments. Each column is from a single run, where time t is referenced to the end of vortex creation (t is the same for each row). The $|1\rangle$ and $|2\rangle$ state images appear different due to different signs of the probe detuning.

potential. Figs. 8.5a and 8.5b are near this limit for t= 0 and 200 ms. In this case the density distribution of the vortex state is vulnerable to instabilities due to the fact that the relative densities of $|1\rangle$ and $|2\rangle$ may evolve with relatively little energy cost so long as the total density remains constant [75]. In the opposite limit (a small amount of $|2\rangle$ fluid), the central potential is negligible and the size of the vortex core (in equilibrium) is determined entirely by its own centrifugal barrier. Figs. 8.5a and 8.5b at $t = 600$ ms are evolving towards this limit. In Fig. 8.5a, we see that the interior $|2\rangle$ fluid is no longer pinning the vortex at 600 ms, but rather is being dragged around by the precessing vortex. The $|2\rangle$ vortex provides an interesting mixture of the above limits. The $|1\rangle$ fluid "floats" to the outside so there is no pinning of the vortex core, but the tendency towards density instabilities remains.

Expanded studies of stability issues are underway. We also expect to be able to observe interesting transitional behavior between these limiting cases. For example, it is a straightforward extension of our method to create an $l = 2$ vortex. In the presence of a strong pinning potential, $l = 2$ vortices should be stable, but in the weak potential limit, $l = 2$ vortices are predicted to spontaneously bifurcate [120].

Bibliography

[1] This is a revised version of [93], with the addition of a comparison to the exicitation spectrum when only the changing number in the condensate is taken into account.

[2] This chapter is a revised version of [105] and [75], with the addition of an introduction and data showing radial separation of condensates in real time.

[3] This is a revised version of [76], including an analysis of the randomization of the relative phase due to experimental noise.

[4] This is a revised version of Matthews(/cond-mat/9906288). Additions include two plots further describing our "phase-twisting" model, and another plot comparing theory to experiment in another regime.

[5] This chapter is a revised version of Matthews(/cond-mat/9908209), with the addition of data showing an interferogram of our "ball and shell", non-vortex mixture of condensates.

[6] J. Williams and M. Holland, cond-mat/9909163.

[7] The observed transition temperature is $T' = 0.94(5)$ [60].

[8] In our previous study of condensate excitations at $T' \approx 0.48$, we used the $m = 0$ non-condensate mode for $T' \approx 1.3$ to calibrate the trap frequency. The present work indicates that this caused the values of ν/ν_r given in Ref. 4 to be too low by 1%. We thank W. Ketterle for pointing out this possible source of systematic error.

[9] To check that any systematic error due to frequency noise is small we have also determined the standard deviation of the measured cloud widths for time intervals corresponding to a couple oscillation periods. Obtaining γ from the exponential decay of these standard deviations is consistent with the damped sine wave fits.

[10] This is based on the approximation that $n^2 - 1 \simeq 2(n-1)$. This is only true when $\Delta \gg \gamma$. For condensates of $\sim 10^{15}$ cm^{-3}, this correction is 1% in real part of n at $\Delta = 100$ MHz.

[11] A. Toepler, 1864.

[12] F. Zernike, in Nobel Lectures, Physics (Elsevier, Amsterdam, 1964), p.239, text of 1953 Nobel Prize lecture.

[13] Equations 5.3 can be indeed generalized to include effects beyond TF approximation. This has been done, for instance, by Pérez-García, Phys. Rev. Lett. **77**, 5320 (1996). For the condensate used in the present work we have numerically checked that the corresponding changes in the final value of a_1/a_2 are much smaller than the experimental uncertainty.

[14] M. R. Andrews *et al.*, Science **275**, 637 (1997). Due to technical noise, the intrinsically random nature of the relative phase was not conclusively established.

[15] One can equally well describe our experimental system as a single condensate in a coherent superposition of internal states, *or* as two separate condensates with a particular relative phase. It would be customary in condensed-matter physics, with a typical coherent sample size of $\sim 10^{20}$ particles, to use the latter description. On the other hand, an expert in atom interferometry, with a typical coherent sample size of 1 particle, would be more likely to use the former.

[16] We define "coherence" as the predictability of the relative quantum phase. For interesting discussions of quantum coherence, see Refs. [100] and [137].

[17] The microwave and rf frequencies are produced by synthesizers locked to global-positioning system (GPS) signals. The manufacturer of the receiver claims a root Allan variance better than 10^{-10}.

[18] C. H. Greene, (private communication).

[19] Atom interferometry between *thermal* beams is a well-established technique. See, for example, D. W. Keith, C. R. Ekstrom, Q. A. Turchette, and D. E. Pritchard, Phys. Rev. Lett. **66**, 2693 (1991). An early condensate interferometer is described in H.-J. Miesner and W. Ketterle, Solid State Commun.

[20] We separate the "environment" into two categories: an "intimate" environment, which includes interactions with thermal atoms as well as with internal modes within the condensate itself; and an "external" environment which includes such experimental factors as uncontrolled fluctuations in the magnetic fields. The former are intrinsic to the physics of the problem, whereas the latter can (in principle) be suppressed. In practice, we experience difficulty in keeping the external environment from intruding on our measurements; only in the modes of quietest operation are the oscillations of Fig. 6.3 observable. When coherence is observed, perturbations due to *both* the intimate and the external environments must be small; when coherence

is washed out, *either* may be responsible. For these reasons, we have not attempted in this paper to quantify the loss of coherence at longer times.

[21] Quantum fluctuations introduce an additional uncertainty that grows linearly in time in a process akin to the spreading of a Gaussian wavepacket in space; see Refs. [49, 134, 89, 102, 84]. We estimate the time scale for this process to be much longer than the duration of an individual measurement.

[22] We take the average of a $\sim 14\ \mu$m wide (post-expansion) vertical swath down the middle of the condensate density profile and extract the amplitude of the pixel at the center of the condensate image (*i.e.*, at the center of the overlap region).

[23] P. Bhattacharyya, T. Ho, and N. Mermin, Phys. Rev. Lett. **39**, 1290 (1977);T.-L. Ho, Phys. Rev. Lett. **48**, 1837 (1982).

[24] For other recent experimental work on multi-component BEC, see [129], and H.-J. Miesner *et al.*, Phys. Rev. Lett. **82**, 2228 (1999).

[25] The probe beam does impose a small, reproducible shift on the energy difference between the $|1\rangle$ and $|2\rangle$ states, a measurable shift for which we correct.

[26] The simulation is a numerical integration of the coupled Gross-Pitaevski equations in. See [133] for more detail.

[27] K. Schwab, N. Bruckner, and R. Packard, **386**, 585 (1997); O. Avenel, P. Hakonen, and E. Varoqaux, Phys. Rev. Lett. **78**, 3602 (1997).

[28] P. O. Fedichev, G. V. Shlyapnikov, and J. T. M. Walraven, Phys. Rev. Lett. **80**, 2269 (1998); L. P. Pitaevskii and S. Stringari, Phys. Lett. A **235**, 398 (1997); W. V. Liu, Phys. Rev. Lett. **79**, 4056 (1997).

[29] P. B. Blakie, R. J. Ballagh and C. W. Gardiner, cond-mat/9902110.

[30] M. H. Anderson *et al.*, Science **269**, 198 (1995); W. Ketterle *et al.,* cond-mat/9904034; E. Cornell *et al.*, cond-mat/9903109.

[31] K.-P. Marzlin, W. Zhang, and E. M. Wright, Phys. Rev. Lett. **79**, 4728 (1997); R. Dum, J. I. Cirac, M. Lewenstein, and P. Zoller, Phys. Rev. Lett. **80**, 2972 (1998); E. L. Bolda and D. F. Walls, Phys. Lett. A **246**, 32 (1998). These vortex generation methods involve transitions between different internal states, as in reference [6].

[32] F. Dalfovo and S. Stringari, Phys. Rev. A **53**, 2477 (1996); T.-L. Ho and V. B. Shenoy, Phys. Rev. Lett. **77**, 2595 (1996); D. S. Rokhsar, Phys. Rev. Lett. **79**, 2164 (1997); R. Dodd, K. Burnett, M. Edwards, and C. Clark, Phys. Rev. A **56**, 587 (1997); B. Jackson, J. F. McCann, and C. S. Adams, Phys. Rev. Lett. **80**, 3903 (1998); A. Fetter, Journal Low. Temp. Phys. **113**,

189 (1998); S. Stringari, Phys. Rev. Lett. **82**, 4371 (1999); T. Isoshima and K. Machida, Phys. Rev. A **59**, 2203 (1999); B. Caradoc-Davies, R. Ballagh, and K. Burnett, Phys. Rev. Lett. **83**, 895 (1999); D. Feder, C. Clark, and B. Schneider, Phys. Rev. Lett. **82**, 4956 (1999).

[33] In the limit of large detuning, δ is equal to the effective Rabi frequency. In our implementation, ω and the effective Rabi frequency are 100 Hz and δ is 94 Hz.

[34] The normalized difference is defined as $(2d_{|1\rangle|2\rangle} - d_{|2\rangle} - d_{|1\rangle})/(2\sqrt{d_{|1\rangle}d_{|2\rangle}})$ where $d_{|i\rangle}$ is the local density for the ith state and $d_{|1\rangle|2\rangle}$ for the interferogram (Fig. 8.3b). This is not exactly the cosine of the phase difference ϕ between the vortex and interior state due to small effects, such as incomplete overlap between the states along the line of sight and uncertainties in the zero levels.

[35] Fundamental physical constants. Phys. Today, 50(8):BG8, May 1997.

[36] M. H. Anderson, J. R. Ensher, M. R. Matthews, C. E. Wieman, and E. A. Cornell. Observation of Bose-Einstein condensation in a dilute atomic vapor. Science, 269(0):198, July 1995.

[37] M. R. Andrews, D. M. Kurn, H.-J. Miesner, D. S. Durfee, C. G. Townsend, S. Inouye, and W. Ketterle. Propagation of sound in a Bose-Einstein condensate. Phys. Rev. Lett., 79(4):553, July 1997. *ibid.* **80**, 2967 (1998).

[38] M. R. Andrews, M.-O. Mewes, N. J. van Druten, D. S. Durfee, D. M. Kurn, and W. Ketterle. Direct, nondestructive observation of a Bose condensate. Science, 273(0):84, July 1996.

[39] E. Arimondo, M. Inguscio, and P. Violino. Experimental determinations of the hyperfine structure in the alkali atoms. Rev. Mod. Phys., 49:31, May 1977.

[40] S. Backhaus, S. V. Pereverzev, A. Loshak, J. C. Davis, and R. E. Packard. Direct measurement of the current-phase relation of a superfluid ^{3}He-B weak link. Science, 278(0):1435, November 1997.

[41] S. M. Barnett, K. Burnett, and J. A. Vaccaro. Why a condensate can be thought of as having a definite phase. J. Res. Natl. Inst. Stand. Tech., 101(4):593, July 1996.

[42] C. C. Bradley, C. A. Sackett, and R. G. Hulet. Bose-Einstein condensation of lithium: Observation of limited condensate number. Phys. Rev. Lett., 78(6):985, February 1997.

[43] C. C. Bradley, C. A. Sackett, J. J. Tollett, and R. G. Hulet. Evidence of Bose-Einstein condensation in an atomic gas with attractive interactions. Phys. Rev. Lett., 75(9):1687, August 1995. *ibid.* **79**, 1170 (1997).

[44] M. Brune, E. Hagley, J. Dreyer, X. Maître, A. Maali, C. Wunderlich, J. M. Raimond, and S. Haroche. Observing the progressive decoherence of the "meter" in a quantum measurement. Phys. Rev. Lett., 77(24):4887, December 1996.

[45] James P. Burke, Jr., John L. Bohn, B. D. Esry, and Chris H. Greene. Impact of the ^{87}Rb singlet scattering length on suppressing inelastic collisions. Phys. Rev. A, 55(4):R2511, April 1997.

[46] James P. Burke, Jr., John L. Bohn, B. D. Esry, and Chris H. Greene. Prospects for mixed-isotope Bose-Einstein condensates in rubidium. Phys. Rev. Lett., 80(10):2097, March 1998.

[47] Th. Busch, J. I. Cirac, V. M. Pérez-García, and P. Zoller. Stability and collective excitations of a two-component Bose-Einstein condensed gas: A moment approach. Phys. Rev. A, 56(4):2978, October 1997.

[48] A. O. Caldeira and A. J. Leggett. Influence of damping on quantum interference: An exactly soluble model. Phys. Rev. A, 31(2):1059, February 1985.

[49] Yvan Castin and Jean Dalibard. Relative phase of two Bose-Einstein condensates. Phys. Rev. A, 55(6):4330, June 1997.

[50] E. A. Cornell, D. S. Hall, M. R. Matthews, and C. E. Wieman. Having it both ways: Distinguishable yet phase-coherent mixtures of Bose-Einstein condensates. J. Low Temp. Phys., 113(3/4):151, 1998.

[51] F. Dalfovo, S. Giorgini, M. Guilleumas, L. Pitaevskii, and S. Stringari. Collective and single-particle excitations of a trapped Bose gas. Phys. Rev. A, 56(5):3840, November 1997.

[52] F. Dalfovo, C. Minniti, S. Stringari, and L. Pitaevskii. Nonlinear dynamics of a Bose condensed gas. Phys. Lett. A, 227(0):259, March 1997.

[53] F. Dalfovo and S. Stringari. Bosons in anisotropic traps: Ground state and vortices. Phys. Rev. A, 53(4):2477, April 1996.

[54] K. B. Davis, M.-O. Mewes, M. R. Andrews, N. J. van Druten, D. S. Durfee, D. M. Kurn, and W. Ketterle. Bose-Einstein condensation in a gas of sodium atoms. Phys. Rev. Lett., 75(22):3969, November 1995.

[55] Wolfgang Demtröder. Laser Spectroscopy. Springer, 1981.

[56] R. J. Dodd, Mark Edwards, C. W. Clark, and K. Burnett. Collective excitations of bose-einstein condensed gases at finite temperatures. Phys. Rev. A, 57:R32, November 1998.

[57] R. Dum, J. I. Cirac, M. Lewenstein, and P. Zoller. Creation of dark solitons and vortices in Bose-Einstein condensates. Phys. Rev. Lett., 80(14):2972, April 1998.

[58] J. A. Dunningham and K. Burnett. Phase standard for Bose-Einstein condensates. Phys. Rev. Lett., 82(19):3729, May 1999.

[59] Mark Edwards, P. A. Ruprecht, K. Burnett, R. J. Dodd, and Charles W. Clark. Collective excitations of atomic Bose-Einstein condensates. Phys. Rev. Lett., 77(9):1671, August 1996.

[60] J. R. Ensher, D. S. Jin, M. R. Matthews, C. E. Wieman, and E. A. Cornell. Bose-Einstein condensation in a dilute gas: Measurement of energy and ground-state occupation. Phys. Rev. Lett., 77(25):4984, December 1996.

[61] J.R. Ensher. The First Experiments with Bose-Einstein Condensation of ^{87}Rb. PhD thesis, University of Colorado, 1998.

[62] B. D. Esry and Chris H. Greene. Low-lying excitations of double Bose-Einstein condensates. Phys. Rev. A, 57(2):1265, February 1998.

[63] B. D. Esry and Chris H. Greene. Spontaneous spatial symmetry breaking in two-component Bose-Einstein condensates. Phys. Rev. A, 59(2):1457, February 1999.

[64] B. D. Esry, Chris H. Greene, James P. Burke, Jr., and John L. Bohn. Hartree-Fock theory for double condensates. Phys. Rev. Lett., 78(19):3594, May 1997.

[65] P. O. Fedichev, G. V. Shlyapnikov, and J. T. M. Walraven. Damping of low-energy excitations of a trapped Bose-Einstein condensate at finite temperatures. Phys. Rev. Lett., 80(11):2269, March 1998.

[66] Alexander L. Fetter. Excited states of a static dilute spherical Bose condensate in a trap. Czech. J. Phys., 46(0):547, 1996. Supplement S1.

[67] Martin Fliesser, András Csordás, Péter Szépfalusy, and Robert Graham. Hydrodynamic excitations of Bose condensates in anisotropic traps. Phys. Rev. A, 56(4):R2533, October 1997.

[68] T.R. Gentile, B.J. Hughey, D. Kleppner, and T.W. Ducas. Experimental study of one- and two-photon rabi oscillations. Phys. Rev. A, 40(9):5103, November 1989.

[69] S. Giorgini, L. P. Pitaevskii, and S. Stringari. Scaling and thermodynamics of a trapped Bose-Condensed gas. Phys. Rev. Lett., 78(21):3987, May 1997.

[70] Elena V. Goldstein and Pierre Meystre. Quasiparticle instabilities in multicomponent atomic condensates. Phys. Rev. A, 55(4):2935, April 1997.

[71] Robert Graham. Decoherence of Bose-Einstein condensates in traps at finite temperatures. Phys. Rev. Lett., 81(24):5262, December 1998.

[72] Robert Graham and Dan Walls. Collective excitations of trapped binary mixtures of Bose-Einstein condensed gases. Phys. Rev. A, 57(1):484, January 1998.

[73] Griffin. cond-mat/9901172.

[74] E.L. Hahn. Phys. Rev. Lett., 80(1):580, February 1950.

[75] D. S. Hall, M. R. Matthews, J. R. Ensher, C. E. Wieman, and E. A. Cornell. Dynamics of component separation in a binary mixture of Bose-Einstein condensates. Phys. Rev. Lett., 81(8):1539, August 1998.

[76] D. S. Hall, M. R. Matthews, C. E. Wieman, and E. A. Cornell. Measurements of relative phase in two-component Bose-Einstein condensates. Phys. Rev. Lett., 81(8):1543, August 1998.

[77] Harald F. Hess. Evaporative cooling of magnetically trapped and compressed spin-polarized hydrogen. Phys. Rev. B, 34(5):3476, September 1986.

[78] Tin-Lun Ho and V. B. Shenoy. Binary mixtures of Bose condensates of alkali atoms. Phys. Rev. Lett., 77(16):3276, October 1996.

[79] M. Holland and J. Cooper. Expansion of a Bose-Einstein condensate in a harmonic potential. Phys. Rev. A, 53(4):R1954, April 1996.

[80] M. J. Holland, D. S. Jin, M. L. Chiofalo, and J. Cooper. Emergence of interaction effects in Bose-Einstein condensation. Phys. Rev. Lett., 78(20):3801, May 1997.

[81] N. M. Hugenholtz and D. Pines. Ground-state energy and excitation spectrum of a system of interacting bosons. Phys. Rev., 116(3):489, November 1959.

[82] D.A. W. Hutchinson, E. Zaremba, and A. Griffin. Finite temperature excitations of a trapped Bose gas. Phys. Rev. Lett., 78(10):1842, March 1997.

[83] A. Imamoḡlu and T. A. B. Kennedy. Optical measurements of the condensate phase. Phys. Rev. A, 55(2):R849, February 1997.

[84] A. Imamoḡlu, M. Lewenstein, and L. You. Inhibition of coherence in trapped Bose-Einstein condensates. Phys. Rev. Lett., 78(13):2511, March 1997.

[85] Tomoya Isoshima and Kazushige Machida. Excitation spectrum in a cylindrical Bose-Einstein condensate. J. Phys. Soc. Jpn., 67(6):1840, June 1998.

[86] J.D. Jackson. Classical Electrodynamics. Wiley and Sons, 1975.

[87] Juha Javanainen. Noncondensate atoms in a trapped Bose gas. Phys. Rev. A, 54(5):R3722, November 1996.

[88] Juha Javanainen. Optical detection of the relative phase between two Bose-Einstein condensates. Phys. Rev. A, 54(6):R4629, December 1996.

[89] Juha Javanainen and Martin Wilkens. Phase and phase diffusion of a split Bose-Einstein condensate. Phys. Rev. Lett., 78(25):4675, June 1997.

[90] Juha Javanainen and Sung Mi Yoo. Quantum phase of a Bose-Einstein condensate with an arbitrary number of atoms. Phys. Rev. Lett., 76(2):161, January 1996.

[91] D. S. Jin, J. R. Ensher, M. R. Matthews, C. E. Wieman, and E. A. Cornell. Collective excitations of a Bose-Einstein condensate in a dilute gas. Phys. Rev. Lett., 77(3):420, July 1996.

[92] D. S. Jin, J. R. Ensher, M. R. Matthews, C. E. Wieman, and E. A. Cornell. Quantitative studies of Bose-Einstein condensation in a dilute atomic vapor. Czech. J. Phys., 46(S6):3070, 1996. Supplement S6.

[93] D. S. Jin, M. R. Matthews, J. R. Ensher, C. E. Wieman, and E. A. Cornell. Temperature-dependent damping and frequency shifts in collective excitations of a dilute Bose-Einstein condensate. Phys. Rev. Lett., 78(5):764, February 1997.

[94] P. S. Julienne, F. H. Mies, E. Tiesinga, and C. J. Williams. Collisional stability of double Bose condensates. Phys. Rev. Lett., 78(10):1880, March 1997.

[95] Yu. Kagan, E. L. Surkov, and G. V. Shlyapnikov. Evolution of a Bose-condensed gas under variations of the confining potential. Phys. Rev. A, 54(3):R1753, September 1996.

[96] Yu. Kagan, E. L. Surkov, and G. V. Shlyapnikov. Evolution and global collapse of trapped Bose condensates under variations of the scattering length. Phys. Rev. Lett., 79(14):2604, October 1997.

[97] Wolfgang Ketterle and Hans-Joachim Miesner. Coherence properties of Bose-Einstein condensates and atom lasers. Phys. Rev. A, 56(4):3291, October 1997.

[98] S.J.J.M.F. Kokkelmans, B.J. Verhaar, K. Gibble, and D.J. Heinzen. Predictions for laser-cooled rb clocks. Phys. Rev. A, 56(6):R4389, December 1997.

[99] C. K. Law, H. Pu, N. P. Bigelow, and J. H. Eberly. Quantum phase diffusion of a two-component dilute Bose-Einstein condensate. Phys. Rev. A, 58(1):531, July 1998.

[100] A. J. Leggett. Broken gauge symmetry in a Bose condensate. In A. Griffin, D. W. Snoke, and S. Stringari, editors, Bose-Einstein Condensation, page 452. Cambridge University Press, 1995.

[101] Anthony J. Leggett and Fernando Sols. On the concept of spontaneously broken gauge symmetry in condensed matter physics. Found. Phys., 21(3):353, 1991.

[102] M. Lewenstein and L. You. Quantum phase diffusion of a Bose-Einstein condensate. Phys. Rev. Lett., 77(17):3489, October 1996.

[103] W. Vincent Liu. Theoretical study of the damping of collective excitations in a Bose-Einstein condensate. Phys. Rev. Lett., 79(21):4056, November 1997.

[104] Mircea Marinescu and Anthony F. Starace. Elementary excitation spectrum of a trapped weakly interacting Bose-Einstein condensate. Phys. Rev. A, 56(1):570, July 1997.

[105] M. R. Matthews, D. S. Hall, D. S. Jin, J. R. Ensher, C. E. Wieman, E. A. Cornell, F. Dalfovo, C. Minniti, and S. Stringari. Dynamical response of a Bose-Einstein condensate to a discontinuous change in internal state. Phys. Rev. Lett., 81(2):243, July 1998.

[106] M.-O. Mewes, M. R. Andrews, N. J. van Druten, D. M. Kurn, D. S. Durfee, and W. Ketterle. Bose-Einstein condensation in a tightly confining dc magnetic trap. Phys. Rev. Lett., 77(3):416, July 1996.

[107] M.-O. Mewes, M. R. Andrews, N. J. van Druten, D. M. Kurn, D. S. Durfee, C. G. Townsend, and W. Ketterle. Collective excitations of a Bose-Einstein condensate in a magnetic trap. Phys. Rev. Lett., 77(6):988, August 1996.

[108] C. J. Myatt, E. A. Burt, R. W. Ghrist, E. A. Cornell, and C. E. Wieman. Production of two overlapping Bose-Einstein condensates by sympathetic cooling. Phys. Rev. Lett., 78(4):586, January 1997.

[109] P. Öhberg, E. L. Surkov, I. Tittonen, S. Stenholm, M. Wilkens, and G. V. Shlyapnikov. Low-energy elementary excitations of a trapped Bose-condensed gas. Phys. Rev. A, 56(5):R3346, November 1997.

[110] Olshanii. Finite-Temperature Collective Excitation of a Bose-Einstein Condensate, cond-mat/9807412.

[111] D. N. Paulson, M. Krusius, and J. C. Wheatley. Long-lived and persistent orbital motions in superfluid ^{3}He-A. Phys. Rev. Lett., 37(10):599, September 1976.

[112] Víctor M. Pérez-García, H. Michinel, J. I. Cirac, M. Lewenstein, and P. Zoller. Low energy excitations of a Bose-Einstein condensate:A time-dependent variational analysis. Phys. Rev. Lett., 77(27):5320, December 1996.

[113] Wolfgang Petrich, Michael H. Anderson, Jason R. Ensher, and Eric A. Cornell. Behavior of atoms in a compressed magneto-optical trap. J. Opt. Soc. Am. B, 11(8):1332, August 1994.

[114] Wolfgang Petrich, Michael H. Anderson, Jason R. Ensher, and Eric A. Cornell. Stable, tightly confining magnetic trap for evaporative cooling of neutral atoms. Phys. Rev. Lett., 74(17):3352, April 1995.

[115] L. Pitaevskii and S. Stringari. Elementary excitations in trapped Bose-Einstein condensed gases beyond the mean-field approximation. Phys. Rev. Lett., 81(21):4541, November 1998.

[116] L. P. Pitaevskii. Phenomenological theory of mode collapse-revival in a confined Bose gas. Phys. Lett. A, 229(0):406, June 1997.

[117] L. P. Pitaevskii and S. Stringari. Landau damping in dilute Bose gases. Phys. Lett. A, 235(0):398, November 1997.

[118] H. Pu and N. P. Bigelow. Collective excitations, metastability, and nonlinear response of a trapped two-species Bose-Einstein condensate. Phys. Rev. Lett., 80(6):1134, February 1998.

[119] H. Pu and N. P. Bigelow. Properties of two-species Bose condensates. Phys. Rev. Lett., 80(6):1130, February 1998.

[120] H. Pu, C. Law, J. Everly, and N. P. Bigelow. Phys. Rev. A, 59:1533, February 1999.

[121] Norman Ramsey. Molecular Beams. Oxford, 1956.

[122] Jürgen Reidl, András Csordás, Robert Graham, and Péter Szépfalusy. Finite-temperature excitations of Bose gases in anisotropic traps. Phys. Rev. A, 59(5):3816, May 1999.

[123] Janne Ruostekoski and Dan F. Walls. Phase-dependent spectrum of scattered light from two Bose condensates. Phys. Rev. A, 55(5):3625, May 1997.

[124] P. A. Ruprecht, M. J. Holland, K. Burnett, and Mark Edwards. Time-dependent solution of the nonlinear Schrödinger equation for Bose-condensed trapped neutral atoms. Phys. Rev. A, 51(6):4704, June 1995.

[125] M. Rusch and K. Burnett. Mean-field theory for excitations of trapped Bose condensates at finite temperatures. Phys. Rev. A, 59(5):3851, May 1999.

[126] Hua Shi and Allan Griffin. Finite-temperature excitations in a dilute Bose-condensed gas. Phys. Rep., 304(1-2):1, October 1998.

[127] K. G. Singh and D. S. Rokhsar. Collective excitations of a confined Bose condensate. Phys. Rev. Lett., 77(9):1667, August 1996.

[128] Kanwal G. Singh and Daniel S. Rokhsar. Disordered bosons: Condensate and excitations. Phys. Rev. B, 49(13):9013, April 1994.

[129] J. Stenger, S. Inouye, D. M. Stamper-Kurn, H.-J. Miesner, A. P. Chikkatur, and W. Ketterle. Spin domains in ground-state Bose-Einstein condensates. Nature, 396:345, November 1999.

[130] S. Stringari. Collective excitations of a trapped Bose-condensed gas. Phys. Rev. Lett., 77(12):2360, September 1996.

[131] J. M. Vogels, C. C. Tsai, R. S. Freeland, S. J. J. M. F. Kokkelmans, B. J. Verhaar, and D. J. Heinzen. Prediction of Feshbach resonances in collisions of ultracold rubidium atoms. Phys. Rev. A, 56(2):R1067, August 1997.

[132] D. F. Walls and G. J. Milburn. Effect of dissipation on quantum coherence. Phys. Rev. A, 31(4):2403, April 1985.

[133] J. Williams, R. Walser, J. Cooper, E. Cornell, and M. Holland. Nonlinear Josephson-type oscillations of a driven, two-component Bose-Einstein condensate. Phys. Rev. A, 59(1):R31, January 1999.

[134] E. M. Wright, D. F. Walls, and J. C. Garrison. Collapses and revivals of Bose-Einstein condensates formed in small atomic samples. Phys. Rev. Lett., 77(11):2158, September 1996.

[135] L. You, W. Hoston, and M. Lewenstein. Low-energy excitations of trapped Bose condensates. Phys. Rev. A, 55(3):R1581, March 1997.

[136] E. Zaremba, A. Griffin, and T. Nikuni. Two-fluid hydrodynamics for a trapped weakly-interacting Bose gas. Phys. Rev. A, 57(6):4695, June 1998.

[137] Wojciech H. Zurek. Decoherence and the transition from quantum to classical. Phys. Today, 44(10):36, October 1991.

Appendix A

Phase-contrast imaging

Following is a more detailed derivation of phase contrast imaging, specializing to our specific case. The only assumptions made previously are qualified here; that the phase shift from a condensate is small, and that the probe beam size is much larger than the condensate. Due to the cylindrical symmetry along the probing direction (aside from a constant scaling factor) the analysis can be done in only one dimension, perpendicular to the direction of beam propagation.

I begin by writing down the electric field for a gaussian beam (of size $\sigma = 1/\sqrt{2a}$) propagating along the $\hat{z}$ direction with angular frequency ω and spatial phase profile $\phi(x) = \phi_0 \exp(-bx^2)$;

$$\begin{aligned} E(\vec{x}, \vec{z}) &= E_0 e^{-ax^2} e^{i\omega t + i\phi(x)} e^{-i\vec{k}\cdot\vec{z}} \\ &\simeq E_0 e^{-ax^2} (1 + i\phi(x) - \phi^2(x)/2) \end{aligned} \tag{A.1}$$

where the approximation is valid for small ϕ_0, and the time and $\vec{z}$ terms can be dropped. This is the field just after the atom cloud. The field at the focal point (P1) of the first imaging lens (Fig. 4.10) is the Fourier transform of the field at the condensate, evaluated at $k = x/\lambda f_1$;

$$\begin{aligned} E(x, P1) &= \int_{-\infty}^{\infty} E_0 e^{-ax^2} \left(1 + i\phi(x) - \phi^2(x)/2\right) e^{-2\pi ikx} dx \\ &= e^{-\frac{\pi^2}{a\lambda^2 f_1^2}x^2} \left(\frac{1}{\sqrt{a}} + \frac{i\phi_0}{\sqrt{a+b}} e^{-\frac{\pi^2}{b\lambda^2 f_1^2}x^2} - \frac{\phi_0^2}{2\sqrt{a+2b}} e^{-\frac{\pi^2}{2b\lambda^2 f_1^2}x^2} \right) \end{aligned} \tag{A.2}$$

In this equation the coefficient to x^2 in the exponent is the size of the beam/phase profile in the focal plane of the first lens. The factors in front are also dropped for convenience, but can be easily replaced at the end by requiring the intensity to be normalized.

This is the point where the phase mask is inserted. The phase mask applies a spatially dependent shift of the following form

$$\theta(x) \begin{cases} \theta & \text{if } -c < x < c \\ 0 & \text{otherwise} \end{cases} \tag{A.3}$$

where $2c$ is the diameter of the magnesium fluoride dot responsible for the phase shift.

Again the Fourier transform is taken and evaluated at $k = x/\lambda f_2$ for the second imaging lens which focuses onto the CCD array. The transform is broken up into two parts due to the discontinuity in the phase dot;

$$\begin{aligned} E(x, P2) &= 2\int_0^c e^{i\theta} E(x, P1) + 2\int_c^\infty E(x, P1) \\ &= e^{-\frac{f_1^2}{f_2^2}ax^2}\Big((e^{i\theta}-1)A+1\Big) + i\phi_0 e^{-\frac{f_1^2}{f_2^2}(a+b)x^2}\Big((e^{i\theta}-1)B+1\Big) \\ &- \frac{\phi_0^2}{2} e^{-\frac{f_1^2}{f_2^2}(a+2b)x^2}\Big((e^{i\theta}-1)C+1\Big). \end{aligned} \tag{A.4}$$

The coefficients in the exponents are now the size of the beam/phase profile in the image plane, properly scaled by the magnification. A, B and C are error functions from the integrals in Eq. A.4;

$$\begin{aligned} A &\equiv \operatorname{erf}\left(\frac{\pi c}{\lambda f_1 \sqrt{a}}\right) \\ B &\equiv \operatorname{erf}\left(\frac{\pi c}{\lambda f_1 \sqrt{a+b}}\right) \\ C &\equiv \operatorname{erf}\left(\frac{\pi c}{\lambda f_1 \sqrt{a+2b}}\right) \end{aligned} \tag{A.5}$$

where the argument of the error functions is the ratio of the size of the phase dot to the beam (in A) or phase profile (in B) in the plane P1.

To find the intensity at the CCD array, the field from Eq. A.4 is squared and time-averaged to give

$$\begin{aligned} I(x) &= 2I_0 e^{-\frac{f_1^2}{f_2^2}ax^2}\Big((1-\cos\theta)A^2+(\cos\theta-1)A+1/2\Big) \\ &+ 2I_0\phi_0 e^{-\frac{f_1^2}{f_2^2}bx^2}(A-B)\sin\theta. \end{aligned} \tag{A.6}$$

This shows that the signal is proportional to the phase shift, and that the spatial distribution is recreated on the CCD. The best signal is obtained when $\theta = \pi/2$ and $A = 1$, $B = 0$. The first condition, $A = 1$, requires that the probe beam waist at the plane P1 is much smaller than the phase dot, and $B = 0$ requires that the diffracted wave from the condensate be much larger than the phase dot at P1. With these conditions the signal is

$$I(x) = I_0(1+2\phi(x)). \tag{A.7}$$